Single-turn Sensitive Stator Inter-turn Fault Detection of Induction Machines

by

Qing Wu
B. Eng.. Tianjin University, China 1997

A Thesis Submitted in Partial Fulfilment of the Requirements for the Degree of

MASTER OF APPLIED SCIENCE

in the Department of Electrical and Computer Engineering

Single-turn Sensitive Stator Inter-turn Fault Detection of Induction Machines

by

Qing Wu
B. Eng., Tianjin University, China 1997

Supervisory Committee

Dr. Subhasis Nandi

Supervisor (Department of Electrical and Computer Engineering)

Dr. A.K.S. Bhat

Department Member (Department of Electrical and Computer Engineering)

Dr. Zuomin Dong

Outside Member (Department of Mechanical Engineering)

Dr. Sudhakar Ganti

External Examiner (Department of Computer Science)

Supervisory Committee

Dr. Subhasis Nandi

Supervisor (Department of Electrical and Computer Engineering)

Dr. A.K.S. Bhat

Department Member (Department of Electrical and Computer Engineering)

Dr. Zuomin Dong

Outside Member (Department of Mechanical Engineering)

Dr. Sudhakar Ganti

External Examiner (Department of Computer Science)

ABSTRACT

Catastrophic failure of the electric machines can result from stator inter-turn faults even at their very incipient stage, i.e., single-turn fault. Consequently, fire and explosion, loss of human life and property, extended downtime of the equipment, increased cost of repair and heavy financial losses in the industries may take place. As a recent trend, online fault diagnosis of the electric machines that are employed in critical applications has been considered of paramount importance since frequent outage of the machines for the purpose of testing cannot be recommended. In this thesis, a very accurate diagnostic scheme has been developed to unambiguously detect single-turn faults on line in squirrel cage induction machines by detecting positive and negative sequence line current third harmonic components.

Initially, inadequacy has been identified in a diagnostic scheme based on negative sequence quantities of the machine and critical improvements have been realized to

suppress the effects of changing supply unbalance. However, the modified method fails to detect faults involving one turn short. The feasibility of computing positive and negative sequence line current third harmonic components have been proved by conducting space vector analysis. Subsequently, a detailed description upon the introduction of these line current third harmonic components is given that accounts for the effects of air gap permeance harmonics, MMF harmonics under supply unbalance, internal asymmetries as well as fault conditions. Least-square method is employed to discriminate fault signatures from those arise from other abnormal operating conditions.

The implementation of the scheme is carried out on both simulated and experimental machines. Mathematical models of the induction machines have been developed which took different induction machine operating conditions into consideration. The machine has been simulated to verify the differences among different complex coefficients by computing complex line current spectra fault signatures with ideal (harmonics-free) three phase voltages input as well as experimentally collected voltages input. Further in an attempt to test the effectiveness of the diagnostic scheme under practical conditions, stator inter-turn faults associated with varying fault severities have been introduced to the line and inverter fed machines under different stator configuration. It has been demonstrated from experimental results that proposed fault signatures can achieve unambiguous single-turn fault detection. In addition, the need of different coefficients for computing the positive and the negative third harmonic related fault signatures have also been demonstrated.

Table of Contents

List of Tables

List of Figures

List of Abbreviations

+3f	Positive third harmonic frequency
-3f	Negative third harmonic frequency
AC	Alternating current
AI	Artificial intelligence
CSI	Current source inverter
DAQ	Data-acquisition system
DC	Direct current
DFT	Discrete Fourier transform
DSP	Digital Signal Processor
DTC	Direct torque control
EPVA	Extended Park's vector approach
FFT	Fast Fourier transform
FL	Fuzzy-logic
FSI_{I-}	Computed positive sequence fault signatures
$FSI_{I3\pm}$	Computed ±3f fault signatures with residues estimated from measured current harmonic components
$FSI_{U3\pm}$	Computed ±3f fault signatures with residues estimated from measured voltage harmonic components
LIM	Linear induction machine
MCSA	Motor current signature analysis
MMF	Magnetomotive-force
MUSIC	Multiple signal classification estimator
MWFA	Modified Winding Function Approach
ODE	Ordinary differential equation
PD	Partial-discharge
PDT	Power decomposition technique

RSM	Reluctance synchronous machine
SM	Synchronous machine
SOFM	Self-organizing feature map
T1	Machine with 1-turn fault under balanced supply
T2	Machine with 2-turn fault under balanced supply
T3	Machine with 3-turn fault under balanced supply
T4	Machine with 4-turn fault under balanced supply
T5	Machine with 5-turn fault under balanced supply
VSI	Voltage source inverter

List of Symbols

$\bar{k}_{I0\pm} - \bar{k}_{I5\pm}$	Complex coefficients
$\bar{k}_{I'0\pm} - \bar{k}_{I'5\pm}$	Complex coefficients
B	Air gap flux density harmonics
f	Fundamental frequency
F	Specific air gap MMF harmonics
f_s	Frequency components to detect in the axial flux component
$g`$	Modified average air-gap length
g_s	Air-gap function
g_s^{-1}	Inverse air-gap function
h	Order of time harmonics
$\bar{I}_{1\text{-}(e)}$	Estimated line current negative sequence component
$\bar{I}_{1\pm(m)}$	Measured line current ±f component
$\bar{I}_{5\pm(m)}$	Measured line current ±5f component
I_a	Stator phase A current
$\bar{I}_{AB}$, $\bar{I}_{BC}$, $\bar{I}_{CA}$	Three phase currents of delta-connected induction machine
I_b	Stator phase B current
I_c	Stator phase C current
I_f	Fault current
$\bar{I}_{I3\pm(e)}$	Current ±3f component estimated from current harmonic components
$\bar{I}_{L1}$, $\bar{I}_{L2}$, $\bar{I}_{L3}$	Three line currents of delta-connected induction machine
I_r	Rotor bar and end ring current vector
I_s	Stator current vector
$\bar{I}_s(j\omega)$	Complex frequency-domain current signature
$\bar{I}_{U3\pm(e)}$	Current ±3f component estimated from voltage harmonic components
j	$\sqrt{-1}$

J	Inertia
k	Any integer
k_{gsat}	Saturation factor
l	Stack length
L_{11}	Magnetizing inductance of winding '1'
L_{12}	Mutual inductance between winding '1' and '2'
L_b	Bar leakage inductance
L_e	Rotor end ring leakage inductance
L_{ls}	Stator phase leakage inductance
L_{rirj}	Mutual inductance between rotor loop 'i' and loop 'j'
L_{rr}	n+1 by n+1 rotor loop and end ring inductance matrix
L_{sr}	3 by n+1 stator phase and rotor bar mutual inductance matrix
L_{srij}	Mutual inductance between stator phase 'i' and rotor bar loop 'j'
L_{ss}	3 by 3 stator phase winding inductance matrix
L_{ssij}	Mutual inductance between phase 'i' and 'j'
m	Order of permeance harmonics
n	Order of space harmonics
N	The number of turns in series in stator per phase
$N_1(\phi)$, $N_2(\phi)$	Winding Functions
$n_a(\phi)$	Turns functions of phase 'a'
$n_{rj}(\phi,\theta)$	Turns functions of rotor loop 'j'
p	Number of fundamental pole-pairs
P	Specific air gap permeance harmonics
p_n	$n \times p$, n is the order of space harmonics
R	Number of rotor bars
r	Radius of the rotor
R_r	n+1 by n+1 rotor bar and end ring resistance matrix
R_s	Stator resistance matrix

T_e	Electromagnetic torque
T_L	Load torque
$U_1(j\omega)$	A random frequency domain impulse at $\omega = \omega_1$
$\bar{U}_{1\pm(m)}$	Measured line voltage ±f component
$\bar{U}_{3\pm(m)}$	Measured line voltage ±3f component
$\bar{U}_{5\pm(m)}$	Measured line voltage ±5f component
$\bar{U}_s(j\omega)$	Complex frequency-domain voltage signature
$\bar{u}_s(t)$	Complex voltage vector of the three-phase system of sinusoidal voltages
$u_{s1}(t)$ - $u_{s3}(t)$	Three phase system of sinusoidal voltages
U_{s1}, U_{s2}, U_{s3}	Amplitudes of three phase system of sinusoidal voltages
$\bar{U}_{s1}$, $\bar{U}_{s2}$, $\bar{U}_{s3}$	Three phase voltage constant vectors
$\bar{U}_{s1}^*$, $\bar{U}_{s2}^*$, $\bar{U}_{s3}^*$	Conjugates of $\bar{U}_{s1}$, $\bar{U}_{s2}$, $\bar{U}_{s3}$
$\bar{U}_{s+}$, $\bar{U}_{s-}$, $\bar{U}_0$	Positive, negative and zero sequence components of three phase system of sinusoidal voltages
V_r	Voltage vector which includes all rotor bars voltages plus one end ring voltage
V_s	Stator voltage vector
W_{co}	Stored magnetic energy
θ_r	Rotor position with respect to the peripheral of stator structure
μ_o	Permeability of the free space
Λ_r	Rotor flux linkage
Λ_s	Stator flux linkage
α	$2\pi/R$
β	Rotor bar skewing angle
γ	$2\pi/3$
θ	Air gap flux position with respect to stator reference frame
ϕ	Stator position measured from stator phase 'a' axis

τ_1, τ_2, τ_3	Arbitrary initial phase angles
ω	Fundamental air gap MMF field rotating angular speed
ω_r	Mechanical speed of rotor

Acknowledgments

I would like to acknowledge and extend my heartfelt gratitude to my supervisor Dr. Subhasis Nandi for his valuable time and constant guidance during the period of this thesis work.

I would like to thank all the members of my supervisory committee for their very beneficial comments and suggestions.

I would like to thank all my fellow graduate students and friends for their constant encouragements.

I would like to thank my parents, my dear wife Guang Shi who have devoted all they can do to support me in finishing this work. I also want to thank my lovely daughters Danlin Wu and Vicky Wu who always help me out of the heavy work load with their adorableness.

Dedication

Dedicated to my beloved my family, my parents, and my sister

Chapter 1

Review of Fault Diagnosis in Induction Machines

1.1 General Description of Induction Machine

Electrical machines have been predominant electro-mechanical power converting devices over a long period of time. Various types of electrical machines, such as DC machine, induction machine, and synchronous machine, have been developed depending on various purposes and requirements [1]. Electrical machines like Linear Induction Machine (LIM), Reluctance Synchronous Machine (RSM), Hysteresis Machine, Stepping Motor intended for specific applications, have also served in both industry and academia over a considerable time [2]. Nowadays, scientists and engineers are still developing new types of electrical machines for custom applications. Essentially all electrical machines are used to translate electrical input to mechanical output or visa versa. There are always two systems involved in them: electrical and mechanical, the coupling medium between these two systems is the magnetic field [3]. In this thesis, stator fault detection in one type of representative electrical machine, i.e. induction machine will be discussed.

An induction machine could be deemed as a rotating electric transformer whose magnetic circuit is separated by air gap into two relatively movable portions. One of them is usually static and is called stator. The rotating part is called the rotor. They are analogous to primary and secondary windings of a transformer [4]. The essential feature which distinguishes the induction machines from other types of electric machines is that their secondary currents are created solely induction, as in a transformer. Hence, induction machines are able to eliminate all sliding electrical contact, resulting in an exceedingly simple and rugged construction [5]. Therefore, induction machines are the most commonly used electrical machines in the industrial scenario. Their applications

could be found from our household appliances such as blenders, mixers, to modern and traditional industries as pumps, compressors, paper mills etc [3, 4].

Induction machines are widely used as critical components in modern industrial processes. Therefore, in spite of their comparative robustness and reliability, their unexpected failure during normal course of operation will result in a significant plant downtime, unavoidable revenue losses or even damage to other equipments [6]. Hence, it is of paramount importance to monitor the conditions of the machines on-line or off-line. If the abnormal state can be successfully recognized at the incipient state, the unscheduled downtime of the machine can be limited and the consequent revenue losses could be prevented.

1.2 Introduction of Induction Machine Fault Diagnosis

The research of fault diagnosis and protection of induction machine is as archaic as the machines themselves. During the early days of induction machines, overvoltage, overcurrent, or ground fault used to be the prevalent fault diagnosis schemes. However, these methods have their inherent limitations: earlier sensing devices did not have sufficient sensitivity to capture the fault signature while the fault is in its incipient stage [6, 7]. Further, along with the fast progress of electrical technology, the machine-load systems are becoming more and more complicated. Some of traditional fault detection methods are in lack of reliable discrimination of the faults from other abnormalities. Hence, recently research towards developing more decisive and reliable fault detection schemes has picked up a fervent pace. A variety of new fault diagnosis techniques have been reported and validated both theoretically and experimentally. Compared with their former counterparts, these new techniques have many advantages. They can be summarized in the following criteria [6, 8]:

- Response time to fault is as short as possible.
- Discriminating fault signature from normal signatures unambiguously.
- Performing fault detection without interrupting the operation of induction machine, i.e. on line non-invasive fault diagnosis.

Basically all those schemes are established based on the fact that each fault will subsequently result in a variation of electrical or mechanical signals. For instance, signatures such as thermal measurements, chemical analysis, etc. have been employed to find out the nature and the degree of the fault. Speed, torque, acoustic noise, vibration etc., have also been attempted to effectively address induction machine faults [8-12]. However, due to lack of fault discrimination procedure or the inconvenience of onsite installation, many of them cannot meet the demand of online condition monitoring [8].

A prevalent fault diagnosis methodology which has been reported by many researchers is based on the estimation of line current harmonic components (commonly known as motor current signature analysis) [8, 13-15]. On-line condition monitoring could easily be realized by fast-speed data acquisition and process devices. Software such as MATLAB is capable of providing sufficiently accurate solution of fault signature estimation with even a normal PC.

Accompanying with the fast upgrading of computer hardware and software, more and more artificial intelligence (AI) based condition monitoring and fault diagnosis strategies have been introduced [16-19]. Fuzzy-logic (FL), for example, is a problem-solving methodology that provides a simple way to arrive at a definite conclusion based upon vague, ambiguous, imprecise, noisy, or missing input information [18, 20]. Gradually, human involvement in the actual fault detection decision making will be totally replaced by automated systems.

1.3 Stator Inter-Turn Fault in Three Phase Induction Machine

Induction machine abnormalities could be classified as bearing faults, stator inter-turn faults, broken rotor bar or cracked end ring, rotor static or dynamic eccentricity or gearbox failures, etc [6, 8]. Amongst all the types of induction machine faults, stator inter-turn fault is next to bearing faults in number of occurrences. Investigation shows 30% ~ 40% of all induction motor failures fall into this category [21]. Hence, exclusive attentions have been paid by various researchers to find out the cause of inter-turn fault

and pursue decisively its predication. It has been reported that inter-turn fault can seriously threaten the safety of operation of the machine by causing excessive heat to the shorted windings and stator core [7, 21 and 22]. Further, if the fault is not detected immediately, it ultimately leads to commonly known line-to-ground or line-to-line faults [8, 22]. Often stator faults lead to fire, explosion in a very short period of time [22, 23]. Thus with stator faults, the machine need to be stopped very quickly in a matter of one third of a second or even lesser time, if possible, in order to prevent any damage to other equipments or even personnel [7, 21-23].

Basically the development of inter-turn fault within a stator winding is due to the insulation failure. A variety of factors have been found to contribute to the failure of insulation. Some of them are listed below [6, 8, and 22]:

- High temperatures of stator core or winding;
- Slack core lamination, slot wedges, and joints;
- Loose bracing for end winding;
- Contamination due to oil, moisture;
- Electrical discharges;
- Leakage in cooling systems.

An explicit description upon how inter-turn short circuit developed within stator winding of an induction machine will be given next. First as background information, some fundamental definitions are reviewed [24].

- A turn consists of two conductors connected to one end by an end connector.
- A coil is formed by connecting several turns in series.
- A winding is fabricated by connecting several coils in series.

The configuration of turn, coil and winding are shown as Fig 1.1 [3].

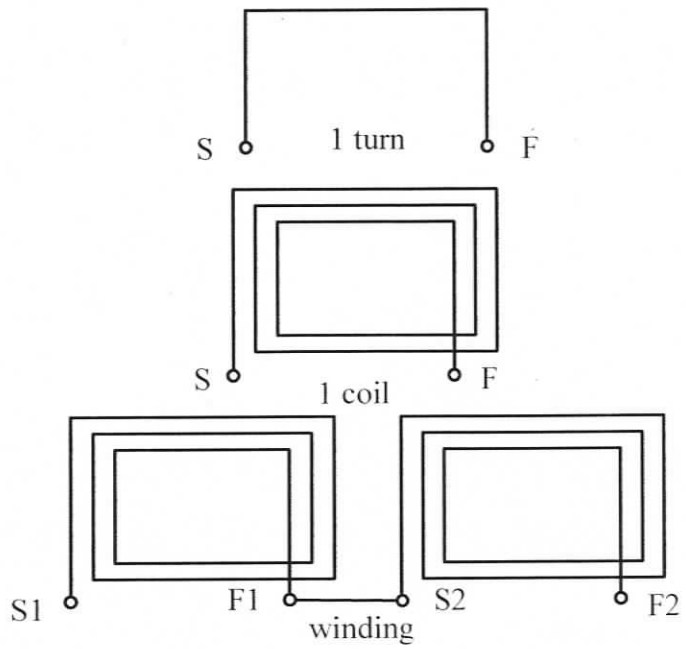

Fig. 1.1 Configurations of turn, coil and winding structure.

In a practical machine, a phase winding is formed by packing multiple numbers of conductors in stator slots and connected via end winding in a systematic manner. These conductors are covered with a thin layer of insulation to provide isolation between conductors as well end windings. Internal short circuit of different turns can thus be prevented by the insulation layer on these conductors. The cross section of one stator slot as well all conductors included is shown in Fig. 1.2 [25].

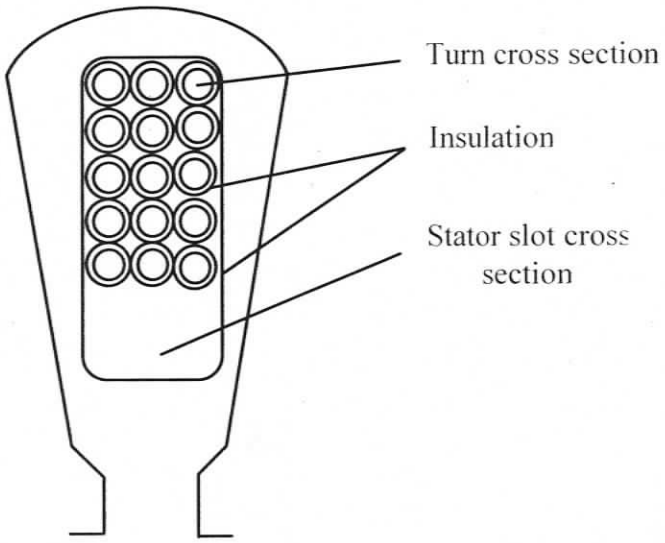

Fig. 1.2 Stator slot cross section with a particular number of conductors included.

A picture of actual stator winding together with end winding is shown in Fig. 1.3,

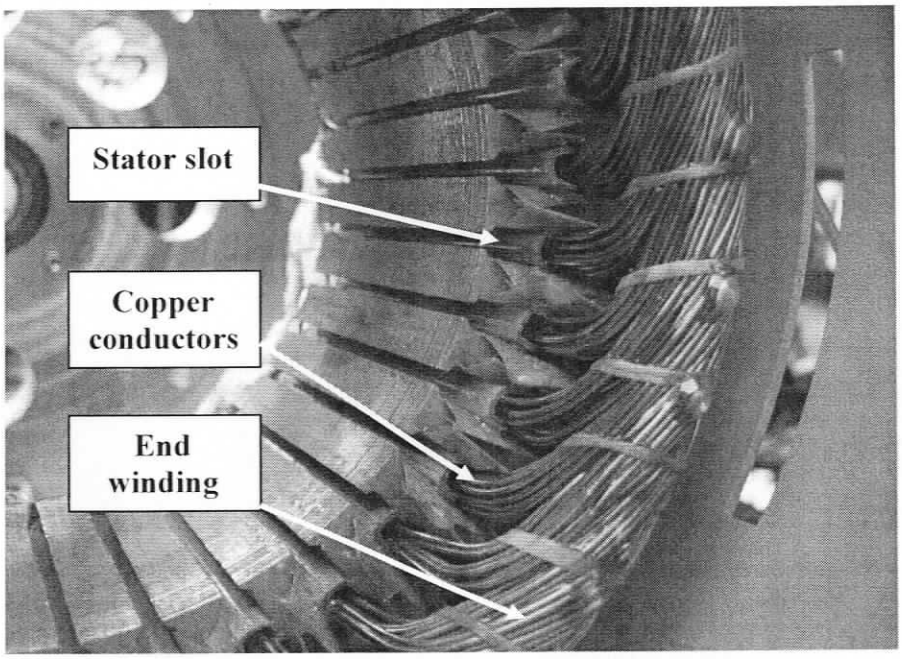

Fig. 1.3 Stator winding of an induction machine.

From Fig. 1.2 and 1.3 one can see that all the conductors in one stator slot are put together intimately. Suppose due to some reasons mentioned earlier, the insulation between two turns fail. This will result in the direct electric contact between these two turns. Fig. 1.3 also shows that it is possible for inter-turn short circuit to develop in end winding portion [7]. In either case, a shorted turn loop which includes one or several turns will be generated in the stator winding [7, 26]. In order to visualize the shorted turn loop created in the stator winding, a faulty loop including several number of turns developed within a three phase system is shown in Fig. 1.4.

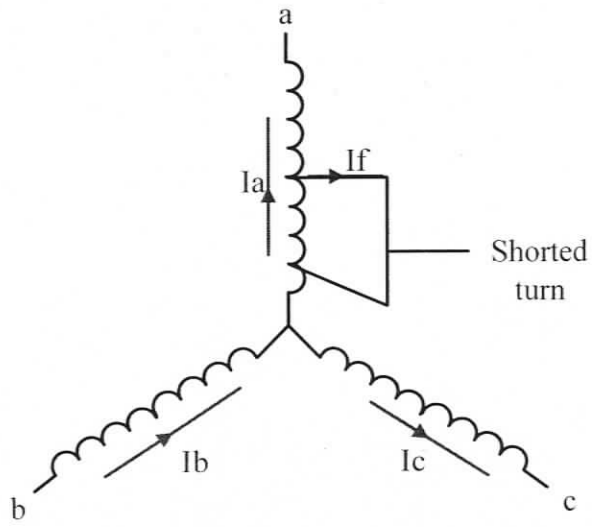

Fig. 1.4 Inter turn short circuit on star connected induction machine phase A.

In Fig. 1.4, 'I_a', 'I_b' and 'I_c' are three phase currents, 'I_f' is the faulty current which is circulating within the faulty loop. Due to the short circuit, the magnitude of this current is going to reach a very high level (almost in the order of twice the short circuit current of the motor [21]) and a large amount of heat will thus be generated [7, 21]. Also from Fig. 1.4 one can see that due to existence of faulty loop, the balance of the 3-phase system has been broken. As the results, 3-phase unbalanced currents will be established accordingly [23, 27 and 28]. More symptoms along with the inter-turn fault will be illustrated in the next section.

1.4 Literature Survey of Stator Inter-turn Fault Detection in Induction Machines

The search of new methodologies and techniques to unambiguously and promptly detect inter-turn fault have been conducted over decades. A variety of novel on-line or off-line fault detecting schemes have been developed which can be attributed to the availability of faster and more sensitive devices. These schemes are taking diverse approaches to achieve inter-turn fault detection, and the validations of them have been proved by various authors. Literature survey show that it is a comparably less challenging task to perform condition monitoring on a high voltage large-dimension or large-volume motor

[8, 22]. For example, online partial-discharge (PD) test can very reliably detect the deterioration of winding insulation on large generator and motor windings rated 4 kV and above. Even a portable test instrument called TGA-B is able to perform this task very well [24]. However, in the case of low voltage motors, the diagnosis methods are yet to be standardized. Therefore, more research interest has been put on the small-size motor fault diagnosis. In the following discussion, some representative fault detecting techniques will be listed.

Toliyat and Lipo [28] have shown that since stator inter-turn fault results in asymmetry in the machine impedance, unbalanced phase currents will be present. This is the result of negative-sequence currents flowing in the three phase windings. However, negative-sequence currents can also arise from inherent machine structural asymmetry, voltage unbalance, machine saturation, etc. In [21, 29], supply unbalance and machine imperfection are modeled to minimize their effect on negative sequence current. It is reported that with these modifications, it is capable of detecting a one turn fault out of a total of 648 turns. However, the methods did not take into account the changing supply unbalance conditions. The method was later modified in [7, 30] to compensate the effect of changing supply unbalances. It was claimed that the resulting negative sequence current signature successfully eliminated the effect of changing supply unbalance. However, the proposed fault signature does not have sufficient sensitivity to unambiguously indicate single turn fault.

In [31], a similar method which is called power decomposition technique (PDT) has been proposed to compensate negative sequence current due to supply unbalance and machine structure imperfection. Temperature effects and slip dependent variations of negative sequence resistance have also been minimized by this scheme. However, it is stated by the authors that this method causes ambiguity in detecting faults involving few turns with supply unbalance in other phases.

Effective negative sequence impedance has been proved to be a valid stator fault indicator for AC machines [32, 33]. The scheme is able to give a clear fault signature under most stator inter-turn fault conditions but may fail in detecting extremely low-level

of faults, especially under supply unbalance. Voltage mismatch detectors were then developed in [34] to overcome this drawback. Compared with negative sequence impedance, voltage mismatch detectors have better performance in detecting extremely small stator winding deterioration. However, as has been pointed out by the authors, voltage mismatch detectors are more difficult to apply as a training period is needed in order to develop the impedance parameters.

In [35], another technique to perform stator inter-turn faults detection of induction motors has been proposed which uses the off-diagonal terms of the impedance matrix. It has been reported that the scheme has better immunity to the varying supply unbalance, measurement errors and the slip-dependent variations of machine's internal asymmetry. Besides, the method is relatively simple and robust. However, the test results under changing supply unbalance have not been reported. Further, the changes in the off-diagonal terms are load-dependent.

Joksimovic and Penman in [26] show that a large increase of line current third harmonic can be used as an indicator of a stator inter-turn fault in induction motors. Conclusions were validated using both simulation and experimental results. However, because the line current third harmonic component is also sensitive to saturation, supply unbalance and internal asymmetries of the machine, ambiguity might arise due to signature corruption from abnormal conditions.

Line current third harmonic component detection technique also have been proposed by Cruz and Cardoso [36], to detect stator inter-turn faults in a Direct Torque Control (DTC) induction motor drive. The action of the torque and flux controllers introduces a strong third harmonic in the motor supply currents, which can be used to detect this type of fault. Unfortunately, once again the inherent asymmetry of the motor would lead to the appearance of third harmonic components in the supply current. Hence the uncertainty is still unavoidable.

Monitoring the change in positive-sequence current using the multiple reference frame theory was additionally suggested in [36] and [37] for detection of stator inter-turn fault. Each fault causes a different disturbance or introduces different components in the

motor supply current. By choosing a proper reference frame, it is possible to transform each one of these current components to a d-q frame. It has been reported that this scheme can successfully eliminate the disturbance of supply unbalance. However, the effectiveness of this method has not been tested under incipient stator fault (like single turn short circuit fault).

Nandi and Toliyat [22] reported that the shorted stator turns act as a search coil to pick up rotor magnetomotive-force (MMF) harmonics in a squirrel cage machine given by

$$k(R/p)\pm 1, \quad k = 1, 2, 3... \tag{1.1}$$

R is number of rotor bars; p is the number of pole pairs. By analyzing the terminal voltages after the motor disconnected from the power supply, one can discriminate the inter-turn fault down to very small number of turns. However, according to (1.1), motor parameters such as rotor slot number are required by this method. Subsequently, a similar terminal voltage analysis technique was proposed in [23]. Based on the interaction between reverse rotating fields and saturation related permeance harmonics, odd multiples of terminal voltage third harmonics have been found to be effective fault indicators. Motor parameter such as rotor bar number is not required by this method hence more applications of it can be found. Both above mentioned two techniques are immune from supply unbalance and time harmonics due to the fact that the fault signatures are attained without power supply. Moreover, these schemes are also capable of detecting the faulty phase of the stator winding. The disadvantage of the above method is that it can only be suitable to the machines which are frequently operated in the transient conditions since they have to be disconnected from the power supply for the fault detection purpose. Thus, this scheme is mainly considered as an effective method to validate the on-line schemes used for the continuous duty motors.

In the fault diagnosis of induction motors, advanced signal processing techniques have been used to reduce the influence of noise and extract useful information [38]. These techniques make use of computationally intense algorithms called MUSIC (multiple signal classification estimators) and ROOT-MUSIC. Experimental results have demonstrated that the proposed scheme has definite advantages over the traditionally

used FFT spectral analysis. However, this method sacrificed from increased computational complexity.

The detection of stator inter-turn faults in both synchronous and asynchronous machines has been carried out by using extended Park's vector approach (EPVA) [39]. Experimental results were obtained in an industrial environment. In EPVA spectrum, the component at twice the supply frequency has been demonstrated to be highly sensitive to such faults. However, test results under supply unbalance were not provided.

A scheme, based on neural networks, has been developed for detecting the stator inter-turn faults in induction machines [40]. A feed-forward neural network combined with the self-organizing feature map (SOFM) learns the model of a healthy machine and visually displays the operating condition of the machine. The drift of operating point of the machine to a specific region on this map is capable of indicating initiation of a fault. Experimental results show that this method is immune to supply unbalance or internal asymmetries in the machine. But, this method needs additional feed-forward neural network. Hence the complexity of detection has been increased.

Penman et al [41] detected turn-to-turn faults by analyzing the axial flux component of the machine using a large coil wound concentrically around the shaft of the machine. The frequency components to detect in the axial flux component are given as

$$f_s = (k \pm \frac{n(1-s)}{p}) f \tag{1.2}$$

Where f is the fundamental frequency, k = 1, 3, s is the slip, n = 1, 2, 3... (2p-1), p is the number of pole pairs. An algorithm has been developed to locate the position of the fault in the stator winding. The theoretical predictions have been validated using experimental results. Similarly, fault analysis of induction machines fed by both sinusoidal supply and voltage source inverter has been carried out using the stray flux [42]. The method has been proven to be a valid fault indictor. However, the test results under changing supply unbalance have not been reported.

An attempt has been made to detect the stator inter-turn faults in induction motor using wavelet packet analysis [43]. The electromagnetic torque is dependent on both

stator and rotor current and very sensitive to asymmetry due to fault. Inter-turn short circuit fault will change the energy distribution in the frequency bands obtained by the wavelet packet analysis of electromagnetic torque signal. Based on each frequency bands' energy eigenvalue, and eigenvector is set up to diagnose the stator inter-turn short circuit fault in induction motors. Experimental results show that the method is able to effectively diagnose the inter-turn short circuit fault independent of the load variations and supply unbalance. However, stator inter-turn fault detection under incipient conditions have not been reported.

Another technique to detect the stator insulation failure of a star-connected induction motor has been proposed whose neutral point is accessible [44]. Faults are detected from the algebraic sum of the three, instantaneous, line-neutral voltages. Band-pass filter is used to remove the harmonics that arise from factors like core saturation, slot harmonics, etc. This scheme is immunes to changes in the operating points of the machine, temperature, and supply voltage. Validation of the scheme through experimental results has also been claimed by the authors. The only known notable limitation is an accessibility requirement to the machine electrical neutral in its wye configuration.

Some other fault detection techniques based on MCSA have been reported for inter-turn stator fault detection [26, 45]. Both low- and high-frequency components are shown to be present under fault. However, the physics behind the existence of such components are not clearly explained yet. Also, voltage unbalance, constructional imperfections that produce similar effects are still disturbing issues.

Stator fault detection using external signal injection is discussed in [46]. A low-magnitude high frequency voltage is superimposed on the fundamental excitation of an inverter fed induction machine, and the measurement of the dc component of the resulting negative-sequence carrier-signal current has been shown to effectively detect turn-to-turn faults at their incipient stage. Besides, this method has a reduced sensitivity to the working conditions of the machine. One drawback of it is that the requirement of continuous injection of small value of the carrier voltage may be undesirable in some applications.

Angular fluctuation of the stator current space vector [47] has also been monitored in detecting stator inter-turn faults. The phase-angle variations are analyzed in frequency domain. The Goertzel algorithm is used for real-time implementation. Experiment results show that this method can give very decisive fault signatures under the condition of stator inter-turn fault. However, in order to eliminate the influence of supply unbalance, the analysis of voltage space vector has to be combined with the analysis of current space vector hence increase the complexity.

1.5 Thesis Outline

The thesis has been written in the following manner. First, a brief introduction of fault detection on electrical machine is included in Chapter 1. Generalized discussion of different types of electrical machine faults is presented followed by the review of some traditional and new fault detection schemes. The causes of stator inter-turn faults have been explored and the importance of decisively detecting inter-turn fault have been explained. Finally, a literature survey of some prevalent inter-turn faults diagnosing methodologies has been listed.

Chapter 2 conducts feasibility analysis of detecting stator inter-turn fault by using negative sequence current signature. Least-square method was applied in order to eliminate the effect of inherent machine structural asymmetry and supply unbalance. The method was further modified to take changing supply unbalance into account. Testing results imply that the effect of supply unbalance can be successfully eliminated by the proposed technique. However, the resulting fault signature is not able to decisively indicate single turn fault, which suggests that it is not a reliable fault indictor.

Feasibility analysis of detecting stator inter-turn faults by the computation of line current positive and negative third harmonics (±3f) is conducted in Chapter 3. Derivation of positive and negative frequency components based on three phase voltages as well as currents space vectors is first furnished. Under the presence of saturation related permeance harmonics, air gap MMF space and time harmonics under practical operating conditions are discussed in an attempt to analyze their effects on ±3f components.

Subsequently, the assumption that ±3f components can also be introduced by fault current is mathematically proved. Since the +3f and -3f components are seen to be caused by the interaction of different MMF and permeance harmonics, the need for residue computation using different sets of coefficients for +3f and -3f components under inherent machine imperfection and supply unbalance conditions have been demonstrated.

Dynamic simulation of induction machine has been conducted in Chapter 4. Winding Functions of stator windings and rotor loops are derived and used in computing inductances that are then used in the coupled inductive circuit model of induction machine. Core saturation and stator inter-turn fault have also been included into the simulation. Initially the induction motor was simulated under ideal balanced and unbalanced voltage condition (harmonics-free). A substantial increase of +3f can be seen when balanced power supply is replaced by unbalanced power supply. It is then demonstrated that turn fault affects both +3f and -3f components. Later in an attempt to obtain simulated fault signatures under more realistic scenario, this model was simulated by feeding three phase experimentally collected voltage data. Considerable differences between +3f and -3f signatures under fault condition can be seen from either line current spectra or computed fault signatures which validate the theoretical analysis in Chapter 3 that essentially pointed towards the need for the use of different coefficients.

Experimental results of inter-turn fault detection based on a line-fed star-connected induction machine are presented in Chapter 5. Line current as well voltage data sets are collected with respect to different conditions of the machine and in accordance with various load levels. Structural imperfection and supply unbalances are compensated by subtracting estimated residual ±3f signatures from measured quantities following the analysis results of Chapter 3. Experimental results show that after residues are subtracted, both voltage and current based -3f and +3f signatures are able to unambiguously indicate even single turn fault.

To test the reliability of the developed ±3f signatures in detecting inter-turn fault, an inverter-fed star-connected induction machine is studied in Chapter 6. Experimental results show that ±3f frequency component can decisively detect even single-turn fault

for solid state motor drives without adding extra computational complexity; provided residues are estimated by line current harmonic components. The machine was tested under 60, 30 and 10 Hz line frequency conditions.

In Chapter 7, the robustness of proposed fault detection scheme is proved by an experiment conducted on a delta connected induction machine. Despite the fact that three phase currents of a delta connected machine are not accessible externally, very effective ±3f fault signatures are obtained for all the four types of fault signatures. Therefore, the proposed fault signatures are valid for delta-connected machines also.

Conclusions and future scope of this thesis are followed in Chapter 8. The contributions that arise out of this work are listed following by the discussion of the constraints of proposed fault detection scheme.

Chapter 2
Investigation of Stator Inter-turn Fault Detection by Using Negative Sequence Current

Literature survey of preceding chapter suggests that many researchers have focused on the stator inter-turn fault detection by using negative sequence current signature [21, 28 and 29]. By removing the signature induced by inherent machine structural asymmetry and supply unbalance from measured negative sequence current signature, one can unambiguously achieve inter-turn fault detection. However, the method is based on the assumption that complex coefficients subject to supply unbalance is not varying under different unbalanced supply voltages. The fault signature was further evaluated on synchronous machine (SM) and RSM by introducing a series of changing supply unbalances [7, 30]. The authors claimed that the fault signature can be seriously influenced by the variation of supply unbalance. The fault signature was then tuned in order to take changing unbalanced supply into account. The resulting fault signature got rid of the effect of supply unbalance to a great extent. Unfortunately, still the sensitivity of the fault signature is not sufficient enough to detect incipient stator inter-turn faults. In the following work, proposed fault signature is investigated on an induction machine under both with and without the changing supply unbalance conditions.

2.1 Concept of Residual Negative Sequence Current (-f) In Three-phase Induction Machine

According to [29], under healthy condition, negative sequence current of induction machine due to inherent structural asymmetry and supply unbalance can be expressed as the following:

$$\bar{I}_{1-(e)} = \bar{k}_0 \overline{U}_{1+(m)} + \bar{k}_1 \overline{U}_{1-(m)} \tag{2.1}$$

Here,

- $\bar{I}_{1-(e)}$ = estimated line current negative sequence component due to inherent structural asymmetry and supply unbalance.
- $\overline{U}_{1+(m)}$ = measured line voltage positive sequence component.
- $\overline{U}_{1-(m)}$ = measured line voltage negative sequence component.

The derivation of $\bar{I}_{1-(e)}$, $\overline{U}_{1+(m)}$ and $\overline{U}_{1-(m)}$ mathematically will be given later in Chapter 3. In this method, negative sequence current determined by (2.1) are deemed as the residual components because it comes from inherent structural asymmetry and supply unbalance. $\bar{k}_0$ and $\bar{k}_1$ are complex coefficients which only vary in accordance with different load conditions. Their values can be estimated by using least-square method. Detailed discussion of this method is given in Appendix A. Under faulty condition, residual negative sequence current signatures are estimated and subtracted from measured quantities to obtain final fault signatures. The mathematical calculation of fault signature residues (or loosely called fault signatures) (FSI_{1-}) is given as below,

$$\mathrm{FSI}_{1-} = \left| I_{1-(m)} - I_{1-(e)} \right| \tag{2.2}$$

where $\bar{I}_{1-(m)}$ is the measured line current negative sequence component. As has been mentioned earlier, a changing supply unbalance might bring ambiguity in detecting incipient stator fault. Therefore, under healthy condition, $\bar{k}_0$ and $\bar{k}_1$ are estimated under two different cases.

- $\bar{k}_0$ and $\bar{k}_1$ are obtained under balanced conditions only.
- $\bar{k}_0$ and $\bar{k}_1$ are obtained under balance and a series of changing supply unbalance conditions.

The resulting faults signatures are listed below followed by the result assessments, respectively.

2.2 Estimation of Complex Coefficients under Balanced Supply

In order to clearly display the trend of fault signatures under different fault severities, seven abbreviations are employed to represent seven conditions of the machine:

- 'HB' = healthy machine fed by balanced voltage supply,
- 'HU' = represents healthy machine fed by unbalanced voltage supply (three line voltages are 448 V, 460 V and 472 V, respectively).
- 'T1' to 'T5' = inter-turn fault conditions involving 1 to 5 turns in the stator winding.

Six 'HB' related data sets are used in the computation of $\bar{k}_0$ and $\bar{k}_1$. Each fault signature is obtained by averaging of six resulting fault signatures computed on 1 second of collected data in an attempt to reduce noise and uncertainty. The detailed test setup has been described in Chapter 5. As mentioned earlier, $\bar{k}_0$ and $\bar{k}_1$ are changing under different load conditions, hence a variety of residual $\bar{I}_{SI-(e)}$ are obtained by repeating the same least-square estimation procedure under different load conditions. The resulting fault signatures with respect to different fault severities are plotted in Fig. 2.1 for three selected load conditions. The same testing results are also summarized into Table 2.1 for all five load conditions (denoted by speed of 1799 rpm, 1790 rpm, 1780 rpm, 1770 rpm and 1760 rpm, respectively). Both Fig. 2.1 and Table 2.1 display upward trend fault signatures when the stator fault goes from 'T1' to 'T5'. However, it can also be seen that under all load levels, the fault signature of 'HU' are higher than that of single-turn fault cases. Hence proposed negative sequence current fault signatures are not able to discriminate a single turn fault from a healthy machine supplied by unbalanced voltage condition. The ambiguity in detecting faults by this scheme under supply unbalances is thus implied.

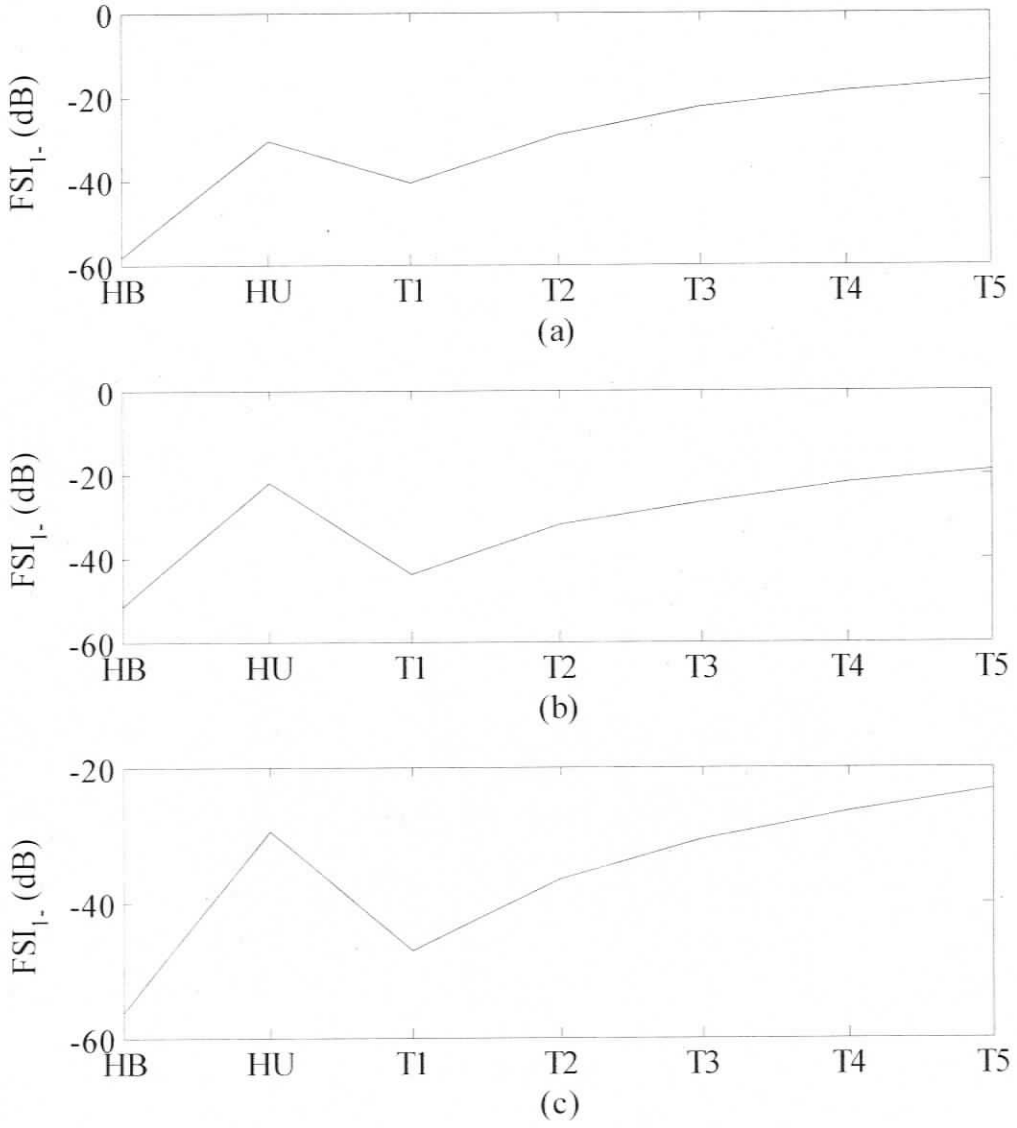

Fig. 2.1 Normalized FSI_{1-} under different load conditions: (a) 1799 rpm (no load); (b) 1780 rpm (half load); (c) 1760 rpm (full load). $\bar{k}_0$ and $\bar{k}_1$ are trained by balanced data only.

Table 2.1 Normalized FSI_{1-} under different load conditions, $\bar{k}_0$ and $\bar{k}_1$ are trained by balanced-data only.

Rotating speed (rpm)	Normalized FSI_{1-} (dB) with respect to fault severities						
	HB	HU	T1	T2	T3	T4	T5
1799	-58.51	-30.77	-40.60	-29.49	-22.81	-18.86	-16.32
1790	-54.44	-37.94	-42.08	-29.74	-21.12	-17.30	-15.12
1780	-51.82	-22.30	-43.88	-32.17	-26.67	-22.16	-19.22
1770	-53.28	-26.27	-46.47	-34.92	-28.91	-24.57	-21.30
1760	-56.41	-29.64	-47.12	-36.57	-30.68	-26.58	-23.44

From Fig. 2.1 and Table 2.1 one can clearly see that under all load conditions, FSI_{1-} at 'HU' are higher than that of 'T1'. The similar fault signature profiles have been shown in [7, 30] with the tests conducted on a reluctance synchronous machine (RSM) and a synchronous machine (SM). Hence, $\bar{k}_0$ and $\bar{k}_1$ obtained are not able to accommodate the variation of unbalanced supply. In order to minimize the effect of changing unbalanced supply, $\bar{k}_0$ and $\bar{k}_1$ are determined by using both balanced supply and unbalanced supply data. Details are given in the following section.

2.3 Estimation of Complex Coefficients under Changing Supply Unbalance

In practice, supply unbalance may happen in infinite many ways. It is impossible to include all unbalanced supply conditions into complex coefficients estimation. In this test, data are collected under one balanced supply condition and six different unbalanced supply conditions. One balanced-data combined with five unbalanced-data and are utilized to estimate complex coefficients. The sixth unbalanced data are utilized to obtain 'HU' signatures. The resulting fault signatures are plotted in Fig. 2.2 under no load, half load and full load conditions respectively. Also fault signatures under all five load conditions are summarized into Table 2.2.

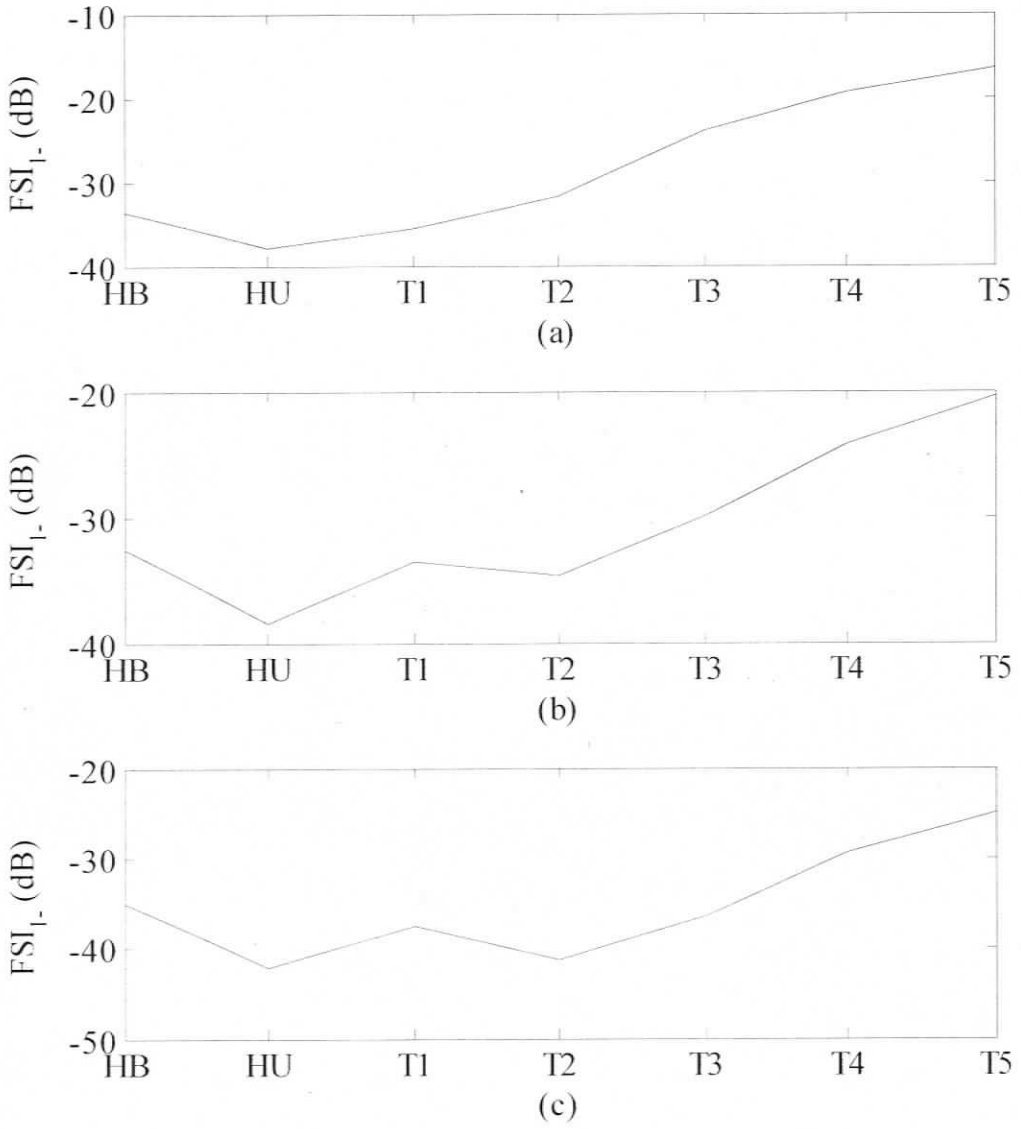

Fig. 2.2 Normalized FSI_{1-} under different load conditions: (a) 1799 rpm (no load); (b) 1780 rpm (half load); (c) 1760 rpm (full load), $\bar{k}_0$ and $\bar{k}_1$ are trained by balanced- and unbalanced-data.

Table 2.2 Normalized FSI_{1-} under different load conditions, $\bar{k}_0$ and $\bar{k}_1$ are trained by balanced- and unbalanced-data.

Rotating speed (rpm)	Normalized FSI_{1-} (dB) with respect to fault severities						
	HB	HU	T1	T2	T3	T4	T5
1799	-33.79	-38.01	-35.65	-31.72	-23.88	-19.36	-16.56
1790	-30.66	-44.13	-31.34	-41.62	-23.55	-19.04	-16.18
1780	-32.62	-38.52	-33.65	-34.61	-29.93	-24.24	-20.32
1770	-34.39	-46.17	-35.66	-37.95	-32.02	-26.59	-22.32
1760	-35.20	-42.10	-37.62	-41.35	-36.50	-29.43	-25.07

It is clear from comparing Fig. 2.1 with Fig. 2.2 and Table 2.1 with Table 2.2, the effects of supply unbalance upon FSI_{1-} has been eliminated to a great extent. However, despite the great improvement that has been achieved, the detectability of the fault signatures is still poor for turn faults up to 3 turns (compare 'HB' with 'T3' at 1760 rpm in Table 2.2). Therefore, they cannot be deemed as a reliable fault indicator.

2.4 Extension of Residue Computation Technique

Since the fault signatures obtained above are not able to effectively indicate a single turn fault, the computation of the residues was further modified such that other factors which are also believed to be affecting sensitivity can be included. According to the line current harmonics analysis given later in Chapter 3, any practical machine will involve stator core iron saturation. Specific air gap permeance harmonics are given accordingly from [27] and [48]:

$$P = P_m \cos(mp\theta - m\omega t) \quad m = 0, 2, 4... \tag{2.3}$$

where, p is fundamental pole pair number; ω is fundamental air gap MMF field rotating angular speed; θ is position with respect to stator reference frame. Due to the presence of third harmonic in line current under practical scenario [23], third time harmonics in MMF will be induced in the air gap. Two relevant harmonics components are expressed as,

$$F_1 = F_{1m}\cos(p\theta - 3\omega t) \text{ and } F_5 = F_{5m}\cos(5p\theta + 3\omega t) \tag{2.4}$$

As air gap flux density harmonics B are obtained as the product of related MMF F and specific permeance harmonics P with expressions given as $B = F \times P$, substituting F and P given in (2.3, 2.4) will result in the following two flux density harmonics for $m = 2$,

$$B = B_{m1}\cos(p\theta + \omega t) \text{ and } B = B_{m2}\cos(7p\theta + \omega t) \tag{2.5}$$

Flux density harmonic components given in (2.5) will introduce negative sequence current in line due to the matching pole pair numbers [49]. Other possible MMF components can be neglected as the coefficients associated with higher order MMF and permeance harmonics decrease very rapidly. The theory of time harmonics, space harmonics, permeance and flux density of a three phase induction machine will be explained explicitly in Chapter 3.

Therefore, based on above analysis, in addition to fundamental positive and negative sequence line voltage components, MMF harmonics given in (2.4) are considered also the cause of residual negative sequence current. As the amplitude of MMF harmonics can be quantified by measuring related voltage harmonics in line, hence, the residue-estimation formula given in (2.1) can now be re-written as,

$$\bar{I}_{S1-(e)} = \bar{k}_0\overline{U}_{S1+(m)} + \bar{k}_1\overline{U}_{S1-(m)} + \bar{k}_2\overline{U}_{S3+(m)} + \bar{k}_3\overline{U}_{S3-(m)} \tag{2.6}$$

Similar steps are taken as has been done in the previous section to obtain fault signatures under different load levels. $\bar{k}_0$ - $\bar{k}_3$ are determined under both with and without including the variation of supply unbalance conditions. The resulting fault signatures under different load levels are shown in the Figs. 2.3, 2.4 and Tables 2.3, 2.4, respectively.

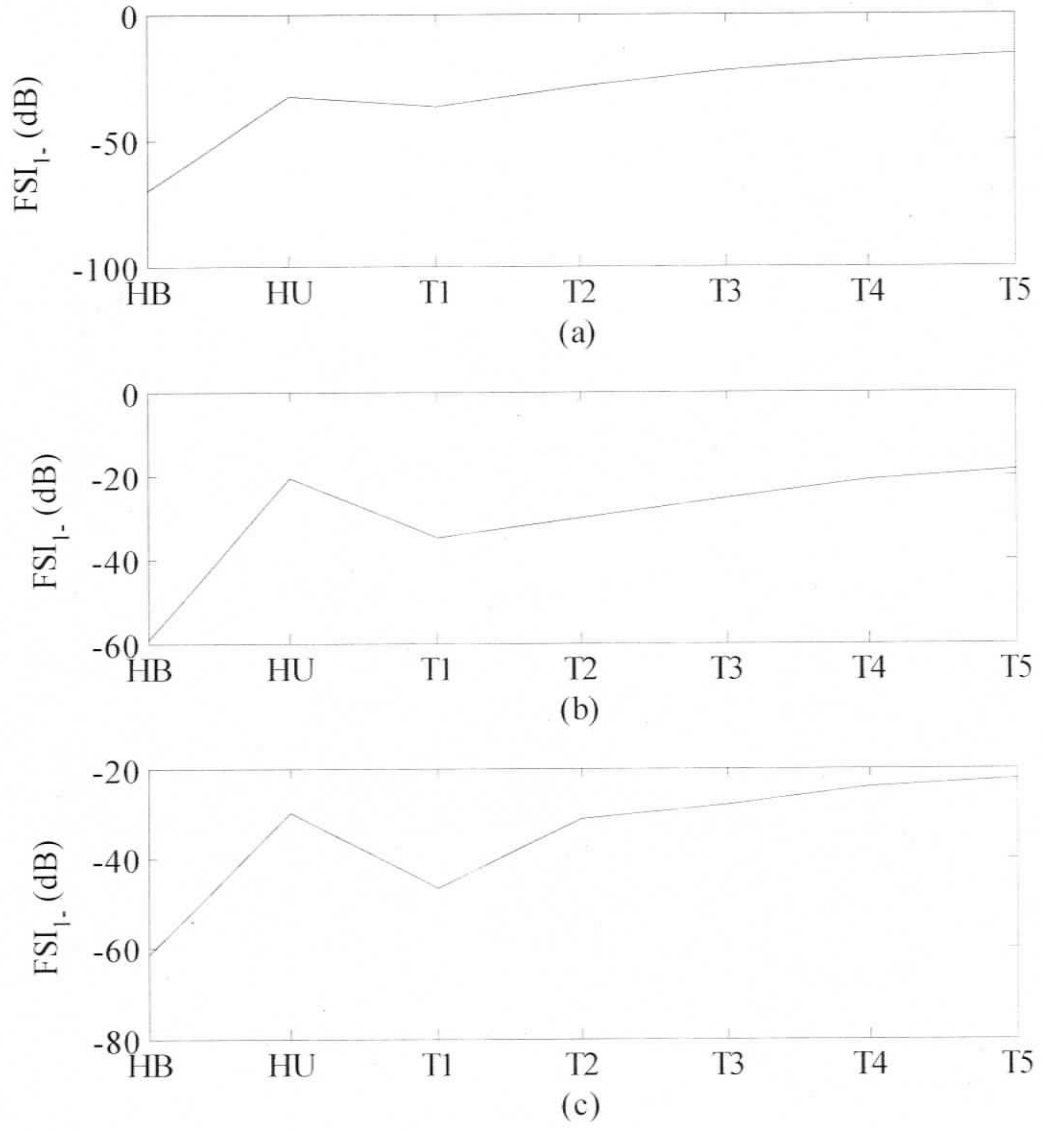

Fig. 2.3 Normalized FSI_{1-} under different load conditions: (a) 1799 rpm (no load); (b) 1780 rpm (half load); (c) 1760 rpm (full load). $\bar{k}_0$ - $\bar{k}_3$ are trained by balanced-data only.

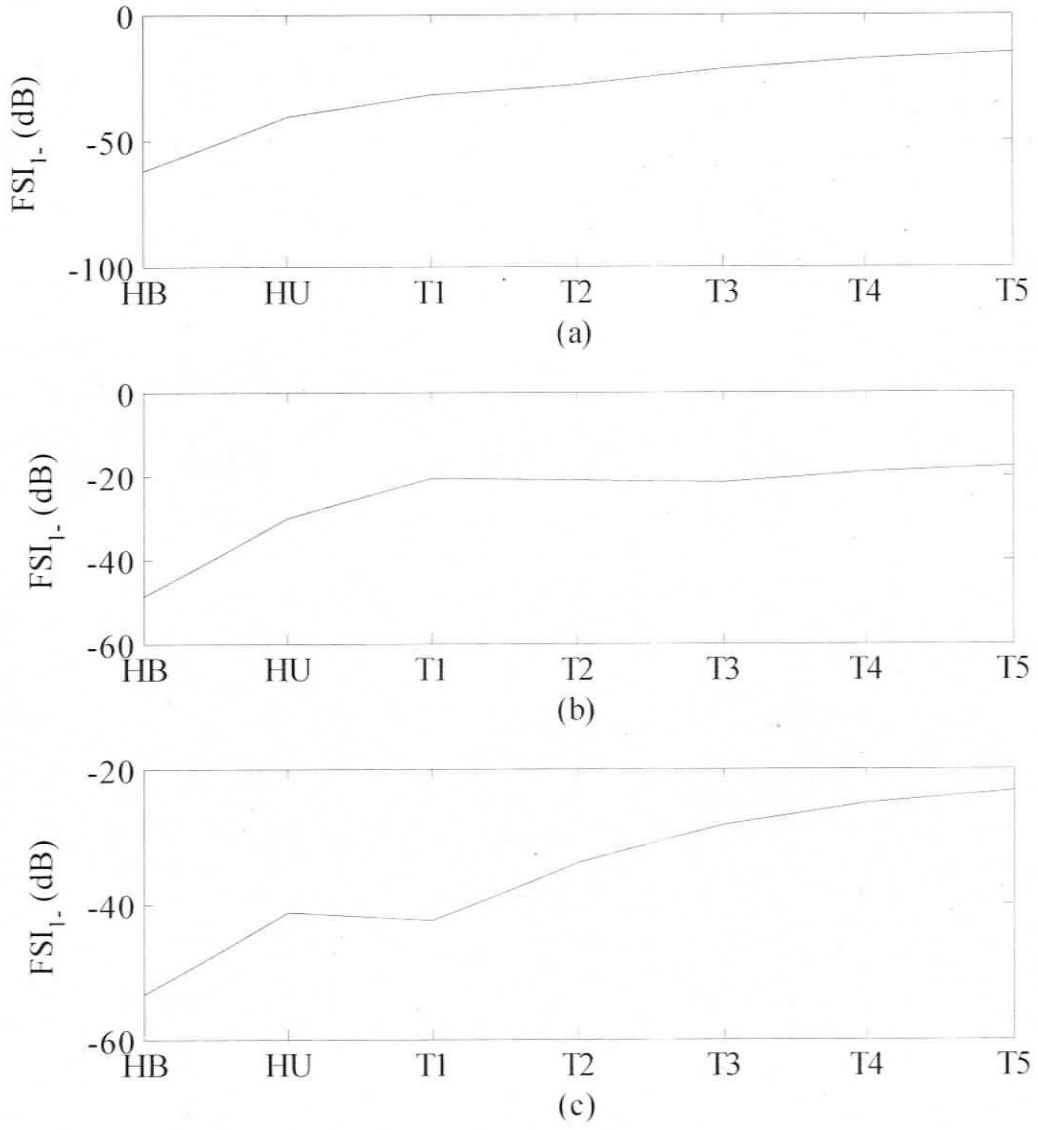

Fig. 2.4 Normalized FSI_{1-} under different load conditions: (a) 1799 rpm (no load); (b) 1780 rpm (half load); (c) 1760 rpm (full load), $\bar{k}_0$ - $\bar{k}_3$ are trained by balanced- and unbalanced-data.

Table 2.3 Normalized FSI_{1-} under different load conditions, $\bar{k}_0$-$\bar{k}_3$ are trained by balanced-data only.

Rotating speed (rpm)	Normalized FSI_{1-} (dB) with respect to fault severities						
	HB	HU	T1	T2	T3	T4	T5
1799	-70.46	-33.06	-37.04	-28.99	-22.34	-18.72	-16.03
1790	-68.49	-38.65	-34.35	-27.12	-20.49	-16.88	-14.85
1780	-59.41	-20.83	-34.89	-30.28	-25.60	-21.22	-18.60
1770	-58.18	-27.03	-31.34	-31.25	-26.83	-23.89	-20.81
1760	-61.43	-29.95	-46.91	-31.25	-27.99	-24.40	-22.34

Table 2.4 Normalized FSI_{1-} under different load conditions, $\bar{k}_0$-$\bar{k}_3$ are trained by balanced- and unbalanced-data.

Rotating speed (rpm)	Normalized FSI_{1-} (dB) with respect to fault severities						
	HB	HU	T1	T2	T3	T4	T5
1799	-34.45	-41.42	-33.30	-30.48	-25.59	-19.98	-16.80
1790	-39.69	-41.14	-31.76	-28.06	-22.22	-18.36	-15.77
1780	-33.85	-31.59	-31.18	-29.33	-21.74	-18.20	-15.68
1770	-36.44	-39.32	-34.53	-31.30	-25.16	-21.89	-19.44
1760	-34.71	-39.36	-37.57	-31.09	-28.26	-26.22	-23.21

Fault signatures given in Figs 2.3-2.4 and Tables 2.3-2.4 are similar as that obtained in the previous section. Clearly, effective single-turn fault detection is still not achievable due to the unclear discrimination between 'T1' and 'HU' and 'HB' (compare 'HB', 'T1' at 1760 rpm in table 2.4).

2.5 Discussions on Testing Results and Contributions

Testing results displayed in Figs. 2.1-2.4 and Tables 2.1-2.4 imply that proposed negative sequence current signatures are not able to decisively separate an incipient turn

fault from health with balanced supply (HB) or health with supply unbalance (HU) conditions. However, as can be see in Figs. 2.2, 2,4 and tables 2.2, 2.4, the supply unbalance- eliminating technique proposed in [7, 30] are still validated on an induction motor. That is, by estimating complex coefficients with both balanced and unbalanced data, disturbances of fault signatures due to changing supply unbalance have been eliminated to a great extent. This conclusion will be used in the subsequent stator fault study as long as changing supply unbalances are concerned.

Another contribution of above study came from the results obtained in section 2.4. The residual negative sequence currents are determined by using (2.6) instead of (2.1). Adding $\overline{U}_{S3+(m)}$ and $\overline{U}_{S3-(m)}$ into the process of residue estimation indeed brings improvements in sensitivities of the proposed negative sequence current signatures to a certain extent. For instance, when four coefficients ($\bar{k}_0$-$\bar{k}_3$) are included in residue estimation, FSI_1- under certain fault level, such as two-turn short (T2) can be unambiguously detected (Table 2.4). However, T2 is not effectively detectable when residues are trained with only two complex coefficients (results shown in Table 2.2). Therefore, although the modified fault signatures are still not able to decisively indicate single turn fault, further improvements may be achieved at the cost of more measurement and complexity.

To sum up, in this chapter, negative sequence current is tested as a fault detector under the presence of changing supply unbalance. The testing results indicate that although the proposed residue minimization technique can help in improving the accuracy of fault signature, unambiguous single turn fault detection is still not possible. In the following chapter, third harmonic components will be further explored for possible unambiguous single turn fault detection.

Chapter 3

Feasibility Analysis of Stator Inter-turn Fault Detection by Using ±3f Line Current Harmonic Components

One important fault detection technique, i.e. negative sequence current detection technique has been tested in the previous chapter. The testing result obtained indicates that proposed fault signature is not an effective fault detector for faults down to single turn faults. It is clear that the proposed residue estimation technique described in chapter 2 cannot thoroughly compensate the inherent structural asymmetry and supply unbalance. Hence, in this chapter, efforts are made to establish an effective fault diagnostic scheme based on other frequency components. Literature survey conducted in chapter 1 reveals that line current third harmonics also play a vital role in detecting stator inter-turn fault [26], [27] and [36]. Hence in the following analysis, fault detection by using line current third harmonic components is attempted. Furthermore, other than computing only positive line current third harmonic (+3f) fault signatures, negative line current third harmonic (-3f) fault signatures are also computed and their sensitivities in detecting stator inter-turn fault are evaluated. As will be shown later in Section 3.3, even under same operating points, the MMF and permeance harmonics producing -3f components are different from those producing +3f components. Hence they need different coefficients for residue computation.

Based on the demand of frequency domain fault analysis, theory of negative frequency is first discussed. A very common method to achieve time to frequency domain conversion is through Fourier Transform. However, Fourier Transform of real line current can only result in positive frequency domain signature like +3f component. It is therefore not suitable for negative frequency computation. Fourier Transform based on a set of complex data, as will show later, will result in both effective positive and negative frequency components. Therefore, complex Fourier Transform is employed in the

following frequency domain signature computation. The construction of time-domain complex voltage and current vectors as well the derivations of complex positive and negative frequency-domain signatures are discussed in the following two sections.

3.1 Introduction of Complex Three-phase Voltage Vector

According to [5], three phase balanced or unbalanced system of sinusoidal voltages having the angular frequency ω_1 can be defined as the following,

$$u_{s1}(t) = \sqrt{2}U_{s1}\cos(\omega_1 t + \tau_1) \tag{3.1}$$

$$u_{s2}(t) = \sqrt{2}U_{s2}\cos(\omega_1 t + \tau_2 - \gamma) \tag{3.2}$$

$$u_{s3}(t) = \sqrt{2}U_{s3}\cos(\omega_1 t + \tau_3 + \gamma) \tag{3.3}$$

Here

$$\gamma = \frac{2\pi}{3}$$

τ_1, τ_2 and τ_3 are arbitrary initial phase angles of $u_{s1}(t)$, $u_{s2}(t)$ and $u_{s3}(t)$

Euler formula $\cos(\omega t) = \frac{e^{j\omega t} + e^{-j\omega t}}{2}$, $j = \sqrt{-1}$ is utilized to convert equations (3.1-3.3) into complex formats and the following equation set is obtained after converting,

$$u_{s1}(t) = \frac{1}{\sqrt{2}}U_{s1}\left(e^{j(\omega_1 t+\tau_1)} + e^{-j(\omega_1 t+\tau_1)}\right) \tag{3.4}$$

$$u_{s2}(t) = \frac{1}{\sqrt{2}}U_{s2}\left(e^{j(\omega_1 t+\tau_2-\gamma)} + e^{-j(\omega_1 t+\tau_2-\gamma)}\right) \tag{3.5}$$

$$u_{s3}(t) = \frac{1}{\sqrt{2}}U_{s3}\left(e^{j(\omega_1 t+\tau_3+\gamma)} + e^{-j(\omega_1 t+\tau_3+\gamma)}\right) \tag{3.6}$$

In [5], complex voltage vector of the three-phase system of sinusoidal voltages are defined as,

$$\overline{u}_s(t) = u_{s1}(t) + u_{s2}(t)e^{j\gamma} + u_{s3}(t)e^{j2\gamma} \tag{3.7}$$

Substituting (3.4 – 3.6) into (3.7) will results in the following expression:

$$\overline{u}_s(t) = \frac{1}{\sqrt{2}}\left[\left(U_{s1}e^{j\tau_1} + U_{s2}e^{j\tau_2} + U_{s3}e^{j\tau_3}\right)e^{j\omega_1 t}\right. \\ \left. + \left(U_{s1}e^{-j\tau_1} + U_{s2}e^{-j(\tau_2-2\gamma)} + U_{s3}e^{-j(\tau_3+2\gamma)}\right)e^{-j\omega_1 t}\right] \tag{3.8}$$

Or

$$\overline{u}_s(t) = \frac{1}{\sqrt{2}}\left[\left(U_{s1}e^{j\tau_1} + U_{s2}e^{j(\tau_2-\gamma)}e^{j\gamma} + U_{s3}e^{j(\tau_3+\gamma)}e^{-j\gamma}\right)e^{j\omega_1 t}\right. \\ \left. + \left(U_{s1}e^{-j\tau_1} + U_{s2}e^{-j(\tau_2-\gamma)}e^{j\gamma} + U_{s3}e^{-j(\tau_3+\gamma)}e^{-j\gamma}\right)e^{-j\omega_1 t}\right] \tag{3.9}$$

According to symmetrical components theory [5], three phase voltages given in (3.1 – 3.3) can be decomposed into positive, negative and zero sequence components given as follow,

$$\overline{U}_{s+} = \frac{1}{3}\left(\overline{U}_{s1} + \overline{U}_{s2}e^{j\gamma} + \overline{U}_{s3}e^{-j\gamma}\right) \tag{3.10}$$

$$\overline{U}_{s-} = \frac{1}{3}\left(\overline{U}_{s1} + \overline{U}_{s2}e^{-j\gamma} + \overline{U}_{s3}e^{j\gamma}\right) \tag{3.11}$$

$$\overline{U}_0 = \frac{1}{3}\left(\overline{U}_{s1} + \overline{U}_{s2} + \overline{U}_{s3}\right) \tag{3.12}$$

where $\overline{U}_{s1}$, $\overline{U}_{s2}$, $\overline{U}_{s3}$ are three phase voltage constant vectors. Their values are defined as

$$\overline{U}_{s1} = U_{s1}e^{j\tau_1},\ \overline{U}_{s2} = U_{s2}e^{j(\tau_2-\gamma)},\ \overline{U}_{s3} = U_{s3}e^{j(\tau_3+\gamma)} \tag{3.13}$$

The complex conjugates of terms in (3.13) are given respectively as,

$$\overline{U}_{s1}^{\ *} = U_{s1}e^{-j\tau_1},\ \overline{U}_{s2}^{\ *} = U_{s2}e^{-j(\tau_2-\gamma)},\ \overline{U}_{s3}^{\ *} = U_{s3}e^{-j(\tau_3+\gamma)} \tag{3.14}$$

Substitute (3.13, 3.14) into (3.9), the following expression will be obtained,

$$\overline{u}_s(t) = \frac{3}{\sqrt{2}}\left[\left(\overline{U}_{s1} + \overline{U}_{s2}e^{j\gamma} + \overline{U}_{s3}e^{-j\gamma}\right)e^{j\omega_1 t} + \left(\overline{U}_{s1}^{\ *} + \overline{U}_{s2}^{\ *}e^{j\gamma} + \overline{U}_{s3}^{\ *}e^{-j\gamma}\right)e^{-j\omega_1 t}\right] \tag{3.15}$$

(3.15) can be further simplified as the following if (3.10, 3.11) are substituted,

$$\overline{u}_s(t) = \frac{3}{\sqrt{2}}\left(\overline{U}_{s+}e^{j\omega_1 t} + \overline{U}_{s-}^{\ *}e^{-j\omega_1 t}\right) \tag{3.16}$$

From the above derivation one can see that a three-phase voltage complex vector can be considered as the superposition of two constant vectors rotating with equal angular velocity in opposite direction. The magnitudes of these two constant vectors are proportional to the positive sequence component $\overline{U}_{s+}$ and conjugate of negative sequence component $\overline{U}_{s-}^{*}$ respectively.

3.2 Converting Time Domain Complex Voltage Vectors into Frequency-domain by Using Fourier Transform

Previous analysis establishes a group of time domain complex voltage vectors. In this section, it will be demonstrated that they can be converted into corresponding positive and negative frequency components by applying Fourier Transform. The detail of deriving complex frequency domain signals from the time domain signals obtained in (3.16) is explained as below.

For the purpose of simplifying the derivation, the inverse Fourier Transform of a frequency domain impulse at $\omega = \omega_1$ is first computed [50]. Suppose a frequency domain signature is given as,

$$U_1(j\omega) = 2\pi[\delta(\omega - \omega_1)] \tag{3.17}$$

The inverse Fourier Transform of this signal is given as:

$$\begin{aligned} u_1(t) &= \frac{1}{2\pi}\int_{-\infty}^{+\infty} 2\pi[\delta(\omega-\omega_1)]e^{j\omega t}\,d\omega \\ &= e^{j\omega_1 t}\int_{-\infty}^{+\infty}\delta(\omega-\omega_1)\,d\omega \\ &= e^{j\omega_1 t} \end{aligned} \tag{3.18}$$

(3.18) can be explained in the following way: A complex exponential signal of frequency ω_1 has a Fourier Transform that is nonzero only at the frequency ω_1. If ω_1 is replaced by $-\omega_1$, (3.17) can be rewritten as:

$$U_2(j\omega) = 2\pi[\delta(\omega + \omega_1)] \tag{3.19}$$

(3.19) indicates now $U_2(j\omega)$ is nonzero only at frequency $-\omega_1$. The inverse Fourier Transform of $U_2(j\omega)$ is,

$$\begin{aligned} u_2(t) &= \frac{1}{2\pi}\int_{-\infty}^{+\infty} 2\pi[\delta(\omega+\omega_1)]e^{j\omega t}\,d\omega \\ &= e^{-j\omega_1 t}\int_{-\infty}^{+\infty}\delta(\omega+\omega_1)d\omega \\ &= e^{-j\omega_1 t} \end{aligned} \tag{3.20}$$

The combination of (3.17-3.20) will result in the following time-frequency domain signal pair:

$$\begin{array}{ccc} Time-domain & & Frequency-domain \\ e^{\pm j\omega_1 t} & \leftrightarrow & 2\pi[\delta(\omega\pm\omega_1)] \end{array} \tag{3.21}$$

(3.21) can be utilized to realize the time-frequency domain conversion. Substituting (3.21) into (3.16), the following complex frequency-domain signatures can be obtained,

$$\overline{U}_s(j\omega) = 3\sqrt{2}\pi\left(\overline{U}_{s+}[\delta(\omega-\omega_1)] + \overline{U}_{s-}^{*}[\delta(\omega+\omega_1)]\right) \tag{3.22}$$

Above derivation demonstrates that complex voltage vector $\overline{u}_s(t)$ can be decomposed into complex positive and negative frequency domain signatures through Fourier Transform. The resulting frequency-domain signature $\overline{U}_s(j\omega)$ is nonzero only at frequency $+\omega_1$ and $-\omega_1$. Thus the spectral lines at $+\omega_1$ and $-\omega_1$ are measures of positive and negative sequence voltage components respectively.

The analysis shown above is based on three phase voltages $u_{s1}(t)$, $u_{s2}(t)$ and $u_{s3}(t)$. The same conclusion can also be applied to three phase currents $i_{s1}(t)$, $i_{s2}(t)$ and $i_{s3}(t)$, i.e., the following expression is also valid,

$$\bar{I}_s(j\omega) = 3\sqrt{2}\pi\left(\bar{I}_{s+}[\delta(\omega-\omega_1)] + \bar{I}_{s-}^{*}[\delta(\omega+\omega_1)]\right) \tag{3.23}$$

The frequency components obtained from (3.22, 3.23) is true for any angular frequency ω_1. Thus the line current $\pm 3\omega_1$ components can also be obtained from the same formulae by simply replacing $\pm\omega_1$ with $\pm 3\omega_1$ in (3.23, 3.24). Also since $\omega_1 = 2\pi f_1$, one can rewrite:

$$\bar{I}_{3s}(j3f) = 3\sqrt{2}\pi\left(\bar{I}_{3s+}\delta(f-3f_1) + \bar{I}_{3s-}^{*}\delta(f+3f_1)\right) \tag{3.24}$$

Therefore, from above complex Fourier Transform, both positive and negative sequence line current frequency components $\bar{I}_{3+}$ and $\bar{I}_{3-}$ can be attained. Positive frequency components correspond to positive angular frequency, whereas negative frequency components correspond to negative angular frequency.

The analysis of above two sections shows that it is feasible to conduct both positive and negative frequency signature analysis based on complex voltage and current vectors. The following analysis emphasizes on finding the cause of line current ±3f harmonic components due to various influencing factors such as space harmonics, time harmonics, and establishing mathematical relationships among them.

3.3 Derivation of ±3f Components in the Induction Machine under Inherent Unbalanced Power Supply and Imperfect Stator Structure Condition

The search for improvements of the ±3f current harmonics based detection scheme under fault condition forms the basis of this thesis. Therefore, in order to obtain effective ±3f fault signatures which can show clear variations under incipient stage of a fault but show minimal changes under unbalanced but not faulty operating conditions, the origin of line current ±3f frequency components under different operating conditions are explored.

According to the basic electromagnetic theory [1], current components induced in the stator windings are proportional to the air gap flux densities. In other words, stator line current harmonics are 'scaled' air gap flux density harmonics. On the other hand, flux densities can be expressed as the product of specific permeance (unit Wb/At m^2) and MMF (unit At) given as

$$B = P \times F \tag{3. 25}$$

where B is air gap flux density, P is specific air gap permeance and F is MMF. Expression (3.25) will be employed later to derive line current ±3f components under different machine operating conditions.

[27], [30] and [51] reported that a significant fundamental reverse rotating magnetic field will be induced due to unbalanced power supply. The interaction between this reverse rotating field and saturation related permeance harmonics will give rise to a strong line current third harmonic (+3f) component. The derivation can be described mathematically as:

$$\begin{aligned} B &= P_m \cos(2p\theta - 2\omega t + \theta_p) \times F_m \cos(p\theta + \omega t + \theta_f) \\ &= B_m \left(\cos(3p\theta - \omega t + \theta_p + \theta_f) + \cos(p\theta - 3\omega t + \theta_p - \theta_f)\right) \end{aligned} \tag{3.26}$$

Based on the theory that only those components in rotating flux density whose pole pair numbers match those of the distribution of stator windings can induce voltage, the second term of (3.26) will introduce +3f components due to a matching flux density pole pair number of p. Therefore, when supplied by ideal three phase voltages (harmonics free); supply unbalance related reverse rotating fields will give rise to +3f signatures only. -3f, however, seems to be less influenced by supply unbalance under harmonics-free input voltages. When supplied by practical three phase voltages, the magnitude of +3f signatures will also differ from that of -3f signatures as they are formed by the interaction of different harmonic components. This assumption is proved later by simulation and experimental results. Therefore as stated earlier, individual computations of +3f and -3f signatures have to be conducted.

Two types of harmonics, hereby space harmonics and time harmonics will be introduced and their contribution to the third current harmonic will be analyzed individually in the following sections.

3.3.1 Space Harmonics under Inherent Structural Imperfection and Unbalanced Supply Condition

An ideal sinusoidal distribution of MMF is possible only if the machine winding is sinusoidally distributed. This is not practically possible to attain. In a real induction machine the stator windings are put in a finite number of slots. As a result, if current flows in these windings, they will induce staircase like MMF waveforms. This waveform can be decomposed into a family of sinusoidal waveforms by using Fourier Series analysis. Those harmonics are known as space harmonics. MMF produced by the n^{th} space harmonic travels at $\frac{1}{n}$ of the speed of the MMF produced by the fundamental space harmonic [3].

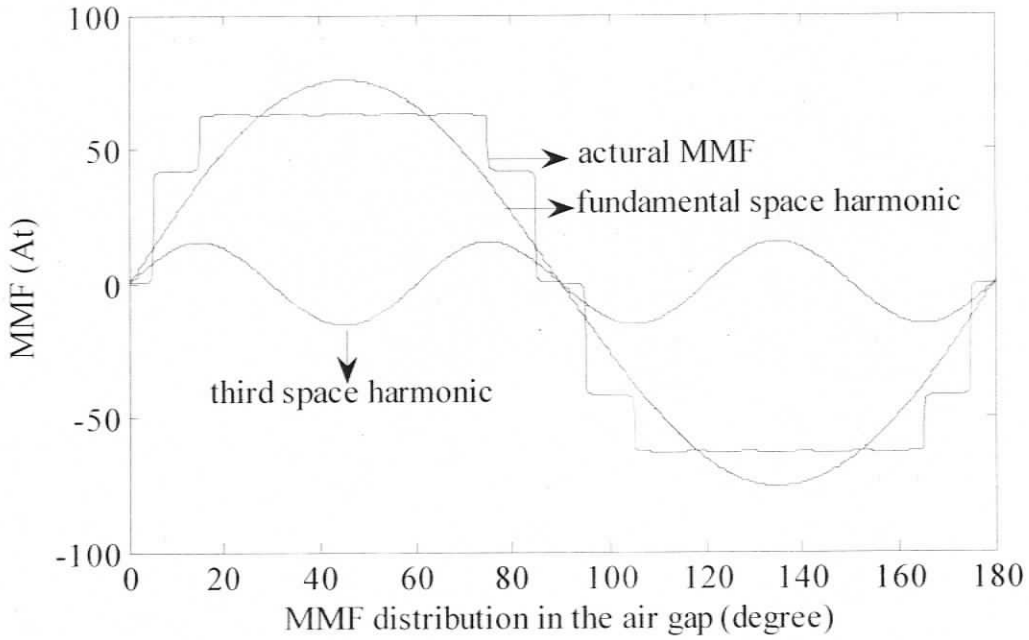

Fig. 3.1 Air gap MMF distribution and its 1st and 3rd harmonics.

The MMF distribution of a distributed winding along with its 1st and 3rd harmonic components is shown in Fig 3.1. MMF space harmonics of an ideally balanced three phase system have been derived in [3]. The components of the rotating MMF waves can be expressed by the following equation,

$$F = F_m \cos(p_n \theta \pm \omega t + \theta_f) \tag{3.27}$$

Here $p_n = n \times p$, n is the order of space harmonics, p is fundamental pole pair number. The sign in front of 'ωt' is '-' as $n = 6k + 1$ and '+' while $n = 6k - 1$, $k = 0, 1, 2, 3\ldots$ [3]. This balance of the three phase system will be disturbed, however, if the machine has structural imperfection or is connected to an unbalanced voltage supply. Accordingly, a set of reverse rotating MMF space harmonics will be created which can be expressed as,

$$F = F_m \cos(np\theta - \omega t),\ n = 5, 11, 17\ldots \tag{3.28}$$

$$F = F_m \cos(np\theta + \omega t),\ n = 1, 7, 13\ldots \tag{3.29}$$

Substituting permeance harmonic equation (2.3) and the MMF space harmonic equations (3.28, 3.29) into (3.25), infinite numbers of flux density harmonics associated with different pole pair numbers and rotating speeds will be obtained. Due to the reason that line current ±3f components can only be introduced by those flux density harmonics whose rotating speed are three times of that of fundamental, analysis followed are conducted only on those flux density harmonics components. According to the analysis of proceeding sections, '+3f' and '-3f' line current harmonic components are determined by forward rotating ($+3\omega$) and reverse rotating (-3ω) flux density harmonic components respectively. A few low order MMF and permeance harmonics were included into the estimation of ±3f line current components. This reduces the complexity of analysis. The results are summarized in Table 3.1.

Table 3.1 Specific harmonic components of air gap permeance P, air gap MMF F (space harmonics), flux density B, and line current I_L, under supply unbalance and structural asymmetry.

P	F	B ($3\omega t$ related)	I_L (3f related)
$P_2 \cos(2p\theta - 2\omega t)$	$F_{s1+}\cos(p\theta + \omega t)$	$B_{s1+}\cos(p\theta - 3\omega t)$	+3f
	$F_{s5-}\cos(5p\theta - \omega t)$	$B_{s7+}\cos(7p\theta - 3\omega t)$	+3f
	$F_{s7+}\cos(7p\theta + \omega t)$	$B_{s5-}\cos(5p\theta + 3\omega t)$	-3f
$P_2 \cos(4p\theta - 4\omega t)$	$F_{s1+}\cos(p\theta + \omega t)$	$B_{s5+}\cos(5p\theta - 3\omega t)$	+3f
	$F_{s5-}\cos(5p\theta - \omega t)$	$B_{s1-}\cos(p\theta + 3\omega t)$	-3f
	$F_{s7+}\cos(7p\theta + \omega t)$	$B_{s11+}\cos(11p\theta - 3\omega t)$	+3f

Table 3.1 clearly demonstrates that due to structural imperfection and unbalanced supply, both +3f and -3f components are introduced in stator line currents because of the interaction between space harmonics and saturation related air gap permeance harmonics. However, different MMF and permeance harmonics are involved in producing them.

3.3.2 Time Harmonics under Inherent Unbalanced Supply and Structural Imperfection Condition

Apart from utility supplies, induction machines powered by voltage source inverter (VSI) or current source inverter (CSI) will include fundamental as well as high order harmonics. These harmonics are known as time harmonics [3]. Higher order time harmonics will produce rotating magnetic fields in the air gap that rotate at higher speed than fundamental MMF. Time harmonics are usually not desired since they will produce parasitic torques in the machine and reduce efficiency due to extra losses. In the following analysis, however, the supply unbalance and structural imperfection related time harmonics have been shown to contribute to the detection of stator inter-turn fault.

Following same procedure of deriving MMF space harmonics shown in the previous section, time harmonics under unbalanced supply voltage and imperfect structure can be given as [3]:

$$F = F_m \cos(p\theta \pm h\omega t) \tag{3.30}$$

h is the order of time harmonics, p is fundamental pole pair number.
(3.30) can be considered the sum of two equations given as:

$$F = F_m \cos(p\theta - h\omega t),\ h = 5, 11, 17 \ldots. \tag{3.31}$$

$$F = F_m \cos(p\theta + h\omega t),\ h = 1, 7, 13 \ldots. \tag{3.32}$$

Combining (3.31) and (3.32) with air gap permeance harmonics (2.3) and taking only a few lower order of them, Table 3.2 can be obtained. Again, only flux densities associating with $\pm 3\omega$ are included in the table because only they are of interest.

Table 3.2 Specific harmonic components of permeance P, air gap MMF F (time harmonics), air gap flux density B, and line current I_L under supply unbalance and structural asymmetry.

P	F	B ($3\omega t$ related)	I_L (3f related)
$P_2\cos(2p\theta - 2\omega t)$	$F_{t1+}\cos(p\theta + \omega t)$	$B_{t1+}\cos(p\theta - 3\omega t)$	+3f
	$F_{t5-}\cos(p\theta - 5\omega t)$	$B_{t1-}\cos(p\theta + 3\omega t)$	-3f
$P_4\cos(4p\theta - 4\omega t)$	$F_{t1+}\cos(p\theta + \omega t)$	$B_{t5+}\cos(5p\theta - 3\omega t)$	+3f
	$F_{t7+}\cos(p\theta + 7\omega t)$	$B_{t5-}\cos(5p\theta + 3\omega t)$	-3f
$P_4\cos(8p\theta - 8\omega t)$	$F_{t5-}\cos(p\theta - 5\omega t)$	$B_{t7+}\cos(7p\theta - 3\omega t)$	+3f
	$F_{t11-}\cos(p\theta - 11\omega t)$	$B_{t7-}\cos(7p\theta + 3\omega t)$	-3f

Similar conclusion can be drawn according to Table 3.2 that due to supply unbalance and structural imperfection, MMF time harmonics are also capable of introducing ±3f line current components.

3.4 Derivation of ±3f Components under Fault Condition

Under stator inter-turn short circuit condition, both +3f and -3f line current components can be introduced due to the presence of fault current. Explanations are given in the following analysis.

A faulty loop can be visualized as a single phase winding. Hence a current through it results in double revolving fields [3]. According to [21], [23], and [51], this fault current will give rise to a new series of MMFs which include all the orders of space harmonics. The interaction between fault current related MMF and saturation related permeance waves will result in a new group of flux density components. These $\pm 3\omega$ related flux density harmonic components will induce ±3f components in line current provided their associated pole pair numbers are matching. Subsequent analysis will be focus on the evaluation of $\pm 3\omega$ related flux density pole pair numbers due to fault current related MMFs.

According to above description, mathematical description of MMF introduced by fault is given as [36],

$$F = F_m \cos(np\theta \pm h\omega t) \tag{3.33}$$

Here,

$$n = 1, 2, 3 \ldots; h = 1, 5, 7, 11\ldots \tag{3.34}$$

The interaction of (3.33) with saturation related permeance equation (2.3) will result in a series of new flux density harmonics given as,

$$B = B_m \cos[(n \pm m)p\theta \pm (h \pm m)\omega t] \tag{3.35}$$

In order for (3.35) to give rise to line current ±3f components, two conditions that are listed below should be satisfied.

- Flux density pole pair numbers are matching pole pair numbers, i.e. $n \pm m = 1, 5, 7, 11\ldots$
- Flux density rotating speed is three times of that of fundamental, i.e. $h \pm m = \pm 3$

The values of n and h are defined by (3.34). Some principle flux density pole pair numbers (given as $n \pm m$) as well rotating speeds (given as $h \pm m$) determined by (3.35) are shown in Tables 3.3 and 3.4.

Table 3.3 Specific orders of space harmonics n, permeance harmonics m and inducing pole pair numbers of flux density harmonics $(n + m)/(n - m)$ given in (3.35).

n \ m	0	2	4	6	8
1	1/1	3/**-1**	**5**/-3	7/-5	9/**-7**
2	2/2	4/0	6/-2	8/-4	10/-6
3	3/3	**5/1**	**7/-1**	9/-3	**11/-5**
4	4/4	6/2	8/0	10/-2	12/-4
5	5/5	**7**/3	9/**1**	11/-1	**13**/-3

Table 3.4 specific orders of time harmonics h, permeance harmonics m and inducing rotating speeds of flux density harmonics $(h + m)/(h - m)$ given in (3.35).

h \ m	0	2	4	6	8
1	1/1	**3**/-1	5/**-3**	7/-5	9/-7
5	5/5	7/**3**	9/1	11/-1	13/**-3**
7	7/7	9/5	11/**3**	13/1	15/-1
11	11/11	13/9	15/7	17/5	19/**3**
13	13/13	15/11	17/19	19/7	21/5

In Table 3.3, cells with numbers in boldface are corresponding to matching flux density pole pair numbers. Cells with numbers in boldface in Table 3.4 are corresponding to $\pm 3\omega$ rotating speed flux density waves. Conclusion can hereby be made that those boldfaced pole pair numbers in Table 3.3 associated with ±3f flux density components only will contribute to ±3f harmonics in line current due to matching pole pair numbers.

To sum up, above analysis show that line current ±3f components can be introduced by factors as unbalanced supply, structural imperfection or stator inter-turn faults. Hence, ±3f signatures obtained in Section 3.2 may not be able to decisively indicate a turn fault due to the influence of unbalanced supply and inherent structural imperfection. Therefore, following residue-elimination technique conducted in the previous chapter, residual ±3f signature-estimation methodology is discussed in the following analysis to minimize their influence in stator fault detection.

3.5 Estimation of Residual ±3f Components

As has been mentioned above, if residual ±3f signature can be effectively isolated from those arising from faulty condition, unambiguous fault detection down to single turn fault can possibly be realized. Therefore, in the following discussions, method of estimating the residual ±3f signatures will be presented.

In Section 3.3 and 3.4, space and time harmonics are discussed separately upon their effects on ±3f line current signatures. Under supply unbalance and machine structural imperfect conditions, both of them are capable of introducing ±3f line current signatures. In Appendix B, a generalized expression of MMF harmonics which combines both time and space harmonics is derived [52]. The equation has the same form as the one given in (3.33), i.e. $F = F_m \cos(np\theta \pm h\omega t)$. However, the orders of space harmonics n as well the rotating directions (the sign in front of h) have been changed. The values of n, h, and associated signs can be summarized by the following two tables:

Table 3.5 n^{th} MMF space harmonic produced by h^{th} current time harmonic under condition of structural imperfection and supply unbalance, '+' implies forward, '-' implies reverse rotation, $k = 1, 2, 3\ldots$, $q = 1, 2, 3\ldots$

Order of space Harmonic n	Order of time harmonic h		
	1	$6q$ - 1	$6q$ + 1
1	-	+	-
$6k$ - 1	+	-	+
$6k$ + 1	-	+	-

Signs associating with the time harmonics shown in Table 3.5 are obtained under conditions of inherent structural imperfection and supply unbalance. Hence they can contribute to the estimation of residual ±3f signatures which when subtracted from measured quantities under fault will lead to effective fault detection. A similar Table 3.6 shows components obtained under perfectly balanced condition for the purpose of comparison. All the signs are changed for balanced supply and a symmetric machine. In practice, MMF waves with both signs will be present with those in Table 3.5 in small quantities even under healthy condition.

Table 3.6 n^{th} MMF space harmonic produced by h^{th} current time harmonic under ideal balanced supply and symmetrical structure condition, '+' implies forward, '-' implies reverse rotation, $k = 1, 2, 3\ldots$, $q = 1, 2, 3\ldots$

Order of space Harmonic n	Order of time harmonic h		
	1	$6q$ - 1	$6q$ + 1
1	+	-	+
$6k$ - 1	-	+	-
$6k$ + 1	+	-	+

In order to reduce analytic complexity, only the principle time harmonics are taken into account while estimating residual ±3f signatures. The reason is that based on the basic magnetic circuit theory, time harmonic components are proportional to the current harmonics from which they are induced. Hence time harmonics can be quantified by measuring the line current or voltage harmonic components. For this purpose, initially the fundamental and fifth time harmonics are included into residue estimation since a) they are the most prominent ones; b) The effect of other time harmonics are deemed to be less considerable, as will be shown subsequently and c) The scheme for detection must be a good tradeoff between computational effort and detection sensitivity.

When harmonic components given in Table 3.5 interact with specific permeance harmonics, a set of specific flux density harmonics will be introduced accordingly. Since only $\pm 3\omega$ rotating speed related flux density harmonics are capable of inducing ±3f line current harmonics, pole pair numbers of only those flux density harmonics are evaluated subsequently. Principle MMF and permeance harmonics and the resulting flux density harmonics as well ±3f line current components are listed in the following table.

Table 3.7 MMF harmonics, air gap permeance harmonics, $\pm 3\omega$ related flux densities and ±3f line current induced.

MMF harmonics	permeance harmonics	$\pm 3\omega$ related flux density harmonics	Line current harmonics
$F_{1-}\cos(p\theta+\omega t)$	$P_2(2p\theta-2\omega t)$	$B_{3+}\cos(p\theta-3\omega t)$	+3f
$F_{1+}\cos(5p\theta-\omega t)$	$P_2(2p\theta-2\omega t)$	$B_{3+}\cos(7p\theta-3\omega t)$	+3f
$F_{5-}\cos(5p\theta+5\omega t)$	$P_8(8p\theta-8\omega t)$	$B_{3+}\cos(13p\theta-3\omega t)$	+3f
$F_{5+}\cos(7p\theta-5\omega t)$	$P_2(2p\theta-2\omega t)$	$B_{3+}\cos(5p\theta-3\omega t)$	+3f
$F_{1+}\cos(5p\theta-\omega t)$	$P_4(4p\theta-4\omega t)$	$B_{3-}\cos(p\theta+3\omega t)$	-3f
$F_{1-}\cos(7p\theta+\omega t)$	$P_2(2p\theta-2\omega t)$	$B_{3-}\cos(5p\theta+3\omega t)$	-3f
$F_{5+}\cos(p\theta-5\omega t)$	$P_2(2p\theta-2\omega t)$	$B_{3-}\cos(p\theta+3\omega t)$	-3f
$F_{5-}\cos(5p\theta+5\omega t)$	$P_2(2p\theta-2\omega t)$	$B_{3-}\cos(7p\theta+3\omega t)$	-3f

In Table 3.7, fundamental and fifth time harmonics only are shown to interact with specific permeance harmonics to produce ±3f harmonics. It can be observed that all the $\pm 3\omega$ related flux density harmonics have matching pole pair numbers. This clearly indicate that under machine structural imperfection and supply unbalance, fundamental and fifth time harmonics are able to introduce both +3f and -3f line current harmonics. From the following experimental (no fault applied) line voltage and current spectrums, one can see that fundamental and fifth MMF harmonic components are quite considerable. Significant contributions from fundamental (±f) and fifth (±5f) time harmonics can thus be proved. In Fig.3.2, line voltage ±3f components can also be observed, signifying that line voltage ±3f components is another contribution of line current ±3f components. However, experimental results obtained in chapter 2 and observations made in [27] indicate that line voltage ±3f components did not play critical roles in resulting unambiguous fault signature. Therefore, initially line voltage ±3f components are not included in computing fault signatures.

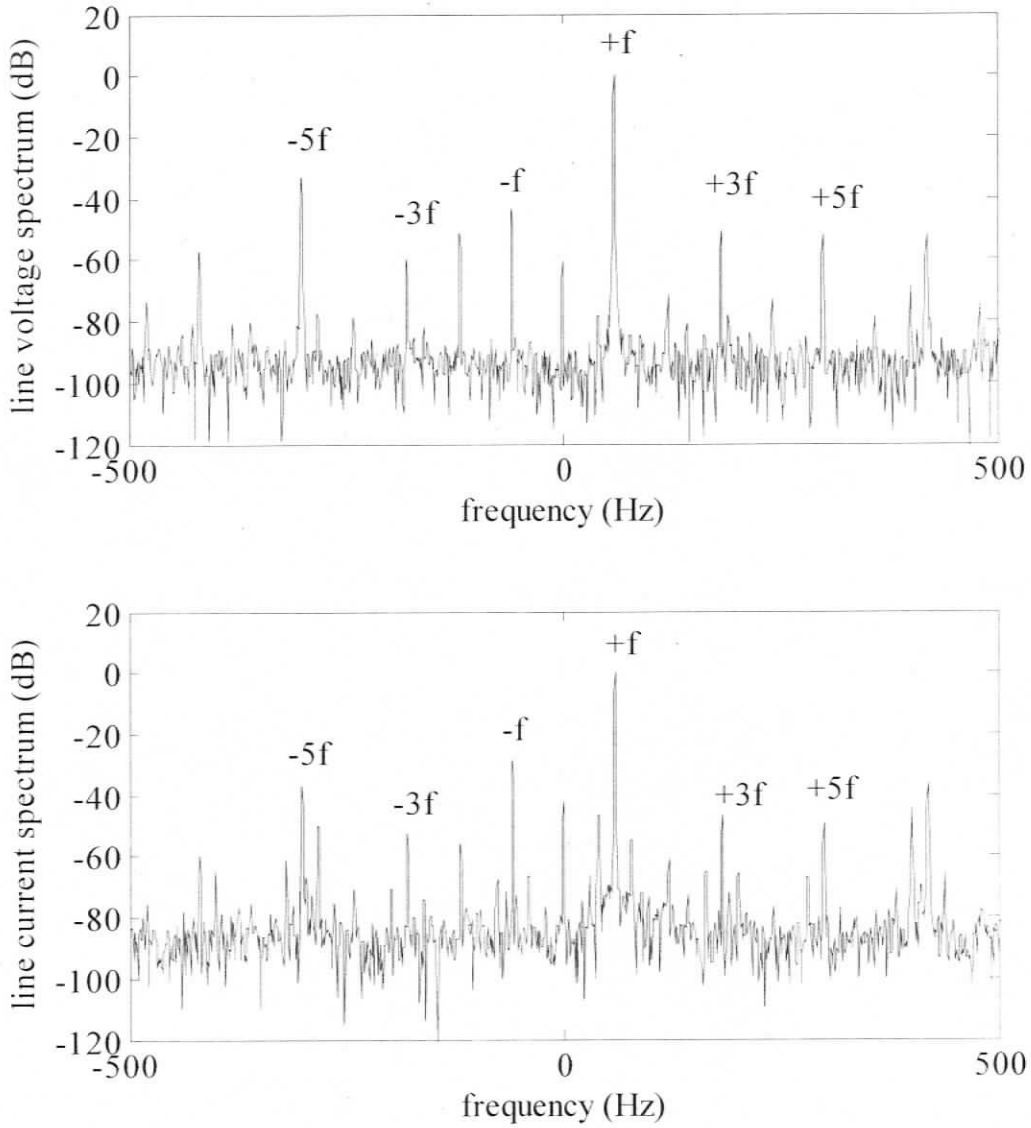

Fig. 3.2 Experimental, normalized line voltage (top) and line current (bottom) spectra with no fault applied, under no load condition.

Based on the conclusion obtained above, either +3f or -3f line current harmonics is mainly affected by fundamental and fifth time harmonics, the following mathematical expression can be used to express this relationship as [7, 30]:

$$\bar{I}_{I3-(e)} = \bar{k}_{I0-}\bar{I}_{1+} + \bar{k}_{I1-}\bar{I}_{1-} + \bar{k}_{I2-}\bar{I}_{5+} + \bar{k}_{I3-}\bar{I}_{5-} \tag{3.36}$$

$$\bar{I}_{I3+(e)} = \bar{k}_{I0+}\bar{I}_{1+} + \bar{k}_{I1+}\bar{I}_{1-} + \bar{k}_{I2+}\bar{I}_{5+} + \bar{k}_{I3+}\bar{I}_{5-} \tag{3.37}$$

where,

$\bar{I}_{I3-(e)}$ = line current -3f component estimated from current harmonics

$\bar{I}_{I3+(e)}$ = line current +3f component estimated from current harmonics

$\bar{I}_{1+}$ = line current +f component

$\bar{I}_{1-}$ = line current -f component

$\bar{I}_{5+}$ = line current +5f component

$\bar{I}_{5-}$ = line current -5f component

Since the current components $\bar{I}_{1+}$, $\bar{I}_{1-}$, $\bar{I}_{5+}$ and $\bar{I}_{5-}$ are deemed to be proportional to the voltage components $\overline{U}_{1+}$, $\overline{U}_{1-}$, $\overline{U}_{5+}$ and $\overline{U}_{5-}$, the following equations can also be expressed,

$$\bar{I}_{U3-(e)} = \bar{k}_{U0-}\overline{U}_{1+} + \bar{k}_{U1-}\overline{U}_{1-} + \bar{k}_{U2-}\overline{U}_{5+} + \bar{k}_{U3-}\overline{U}_{5-} \tag{3.38}$$

$$\bar{I}_{U3+(e)} = \bar{k}_{U0+}\overline{U}_{1+} + \bar{k}_{U1+}\overline{U}_{1-} + \bar{k}_{U2+}\overline{U}_{5+} + \bar{k}_{U3+}\overline{U}_{5-} \tag{3.39}$$

where,

$\bar{I}_{U3-(e)}$ = line current -3f component estimated from voltage harmonics

$\bar{I}_{U3+(e)}$ = line current +3f component estimated from voltage harmonics

$\overline{U}_{1+}$ = line voltage +f component

$\overline{U}_{1-}$ = line voltage -f component

$\overline{U}_{5+}$ = line voltage +5f component

$\overline{U}_{5-}$ = line voltage -5f component

Following Chapter 2, the complex coefficients are estimated by using least-square technique [53]. The residues are then subtracted from measured ±3f signatures from a faulty machine to obtain final fault signatures. The values of complex coefficients are affected by the following factors:

- Load levels of the machine due to the variation of saturation
- Whether +3f or -3f line current components are computed
- Whether voltage or currents signatures are utilized in complex coefficients estimation
- Number of coefficients used
- Number of data sets used to obtained the complex coefficients
- Supply unbalance

The uncertainty of balance in power supply under actual operating environments will increase the ambiguity of this fault detection scheme. Thus, more efforts are taken to eliminate the residues due to unbalanced supply voltages. One set of balanced measurements with five sets of different unbalanced measurements of $\overline{U}_{1\pm}, \overline{U}_{5\pm}$ and $\overline{I}_{l/3\pm}$ are obtained and substituted into (3.38 – 3.39) with $\overline{I}_{l/3+(e)}$ and $\overline{I}_{l/3-(e)}$ replaced with $\overline{I}_{l/3+(m)}$ and $\overline{I}_{l/3-(m)}$. Hereby a set of mathematical equations can be established and grouped into the following complex matrix form.

$$\begin{bmatrix} \overline{I}_{l/3-}(1) \\ \overline{I}_{l/3-}(2) \\ \overline{I}_{l/3-}(3) \\ \overline{I}_{l/3-}(4) \\ \overline{I}_{l/3-}(5) \\ \overline{I}_{l/3-}(6) \end{bmatrix} = \begin{bmatrix} \overline{U}_{1+}(1) & \overline{U}_{1-}(1) & \overline{U}_{5+}(1) & \overline{U}_{5-}(1) \\ \overline{U}_{1+}(2) & \overline{U}_{1-}(2) & \overline{U}_{5+}(2) & \overline{U}_{5-}(2) \\ \overline{U}_{1+}(3) & \overline{U}_{1-}(3) & \overline{U}_{5+}(3) & \overline{U}_{5-}(3) \\ \overline{U}_{1+}(4) & \overline{U}_{1-}(4) & \overline{U}_{5+}(4) & \overline{U}_{5-}(4) \\ \overline{U}_{1+}(5) & \overline{U}_{1-}(5) & \overline{U}_{5+}(5) & \overline{U}_{5-}(5) \\ \overline{U}_{1+}(6) & \overline{U}_{1-}(6) & \overline{U}_{5+}(6) & \overline{U}_{5-}(6) \end{bmatrix} \begin{bmatrix} \overline{k}_{l/0-} \\ \overline{k}_{l/1-} \\ \overline{k}_{l/1-} \\ \overline{k}_{l/3-} \end{bmatrix} \tag{3.40}$$

Equation (3.40) is obtained from (3.38). In (3.40), $\overline{I}_{l/3-}(1)$, $\overline{U}_{1+}(1)$, $\overline{U}_{1-}(1)$, $\overline{U}_{5+}(1)$ and $\overline{U}_{5-}(1)$ are the measured data sets with balanced quantities (first row of current and voltage matrix); the rest are measured data sets associating with unbalanced quantities. The complex coefficients $\overline{k}_{l/0-} - \overline{k}_{l/3-}$ can be solved out by simply perform K = pinv (U) ×I in MATLAB [54]. The same way $\overline{k}_{l/0+} - \overline{k}_{l/3+}$ can be solved using (3.39). After the computation of above mentioned complex coefficients, ±3f residues can be estimated following (2.2)

In order to validate theoretical analysis, a series of simulation and experiments are conducted. They are introduced in the following chapters.

Chapter 4

Modeling of Three Phase Induction Machine with Modified Winding Function Approach (MWFA) and Stator Inter-turn Faults Analysis with Simulated Line Currents

In an attempt to predict the performance of a three phase induction machine under various operating conditions, the operation of the induction machine is simulated using a coupled magnetic circuit model [13], [27]. The model includes a set of differential equations which take stator phase currents, rotor bar currents, rotor speed and peripheral position as state variables. The coupled inductances of stator phase winding and rotor bar are computed using MWFA [55] by taking all the principal stator winding and rotor loop space harmonics into consideration. The model is then solved numerically with the simulation software developed in MATLAB. The model can also include stator iron saturation and inter-turn faults in order to facilitate fault signatures analysis. The simulations are conducted under two types of supply voltages, i.e. harmonics-free voltages and experimentally collected voltages and the fault analysis results are displayed accordingly.

4.1 State Space Model of 3 - ϕ Induction Machine [13], [27]

Stator winding voltage equation is given as:

$$V_s = R_s I_s + \frac{d\Lambda_s}{dt} \tag{4.1}$$

where the stator flux linkage Λ_s are:

$$\Lambda_s = L_{ss} I_s + L_{sr} I_r \tag{4.2}$$

$$V_s = [v_a \;\; v_b \;\; v_c]^t \tag{4.3}$$

$$I_s = [i_a \ i_b \ i_c]^t \tag{4.4}$$

$$I_r = [i_{r1} \ i_{r2} \ \ldots \ i_{rm} \ i_{re}]^t \tag{4.5}$$

V_s is stator voltage vector, I_s is stator current vector, I_r is rotor loop and end ring current vector. R_s is stator resistance matrix, L_{ss} is 3 by 3 stator phase winding inductance matrix, L_{sr} is 3 by n+1 stator phase and rotor bar mutual inductance matrix, whose elements are given below respectively:

$$R_s = \begin{bmatrix} r_s & 0 & 0 \\ 0 & r_s & 0 \\ 0 & 0 & r_s \end{bmatrix} \tag{4.6}$$

$$L_{ss} = \begin{bmatrix} L_{ss11} + L_{ls} & L_{ss12} & L_{ss13} \\ L_{ss21} & L_{ss22} + L_{ls} & L_{ss23} \\ L_{ss31} & L_{ss32} & L_{ss33} + L_{ls} \end{bmatrix} \tag{4.7}$$

$$L_{sr} = \begin{bmatrix} L_{sr11} & L_{sr12} & \ldots & L_{sr1n} & L_{sr1e} \\ L_{sr21} & L_{sr22} & \ldots & L_{sr2n} & L_{sr2e} \\ L_{sr31} & L_{sr32} & \ldots & L_{sr3n} & L_{sr3e} \end{bmatrix} \tag{4.8}$$

L_{ssij} is mutual inductance between phase 'i'and 'j'. L_{ssij} represents magnetizing inductance is case of 'i' is equal to 'j'. L_{ls} is stator phase leakage inductance. L_{srij} is mutual inductance between stator phase 'i' and rotor loop 'j'.

Voltage equations relating to rotor are given as:

$$V_r = R_r I_r + \frac{d\Lambda_r}{dt} \tag{4.9}$$

where V_r is voltage vector which includes all rotor bar voltages plus one end ring voltage. Therefore, in this model, V_r is a null array with n+1elements included; with n loops, each consists of two rotor bars and two end ring segment and one loop consists of one end ring.

Λ_r is rotor flux linkage which can be expressed as:

$$\Lambda_r = L_{rr} I_r + L_{rs} I_s \tag{4.10}$$

R_r is n+1 by n+1 rotor bar and end ring resistance matrix which is given as:

$$R_r = \begin{bmatrix} 2(r_b + r_e) & -r_b & 0 & \dots & 0 & -r_b & -r_e \\ -r_b & 2(r_b + r_e) & -r_b & \dots & 0 & 0 & -r_e \\ \vdots & \vdots & \vdots & \dots & \vdots & \vdots & \vdots \\ \vdots & \vdots & \vdots & \dots & \vdots & \vdots & \vdots \\ 0 & 0 & 0 & \dots & 2(r_b + r_e) & -r_b & -r_e \\ -r_b & 0 & 0 & \dots & -r_b & 2(r_b + r_e) & -r_e \\ -r_e & -r_e & -r_e & \dots & -r_e & -r_e & nr_e \end{bmatrix} \tag{4.11}$$

L_{rr} is n+1 by n+1 rotor loop and end ring inductance matrix, given by:

$L_{rr} =$

$$\begin{bmatrix} L_{r1r1} + 2(L_b + L_e) & L_{r1r2} - L_b & L_{r1r3} & \dots & L_{r1r(n-1)} & L_{r1rn} - L_b & -L_e \\ L_{r2r1} - L_b & L_{r2r2} + 2(L_b + L_e) & L_{r2r3} - L_b & \dots & L_{r2r(n-1)} & L_{r2rn} & -L_e \\ \vdots & \vdots & \vdots & \dots & \vdots & \vdots & \vdots \\ \vdots & \vdots & \vdots & \dots & \vdots & \vdots & \vdots \\ L_{r(n-1)r1} & L_{r(n-1)r2} & L_{r(n-1)r3} & \dots & L_{r(n-1)r(n-1)} + 2(L_b + L_e) & L_{r(n-1)rn} - L_b & -L_e \\ L_{rnr1} - L_b & L_{rnr2} & L_{rnr3} & \dots & L_{rnr(n-1)} - L_b & L_{rnrn} + 2(L_b + L_e) & -L_e \\ -L_e & -L_e & -L_e & \dots & -L_e & -L_e & nL_e \end{bmatrix} \tag{4.12}$$

L_{rirj} is the mutual inductance between rotor loop 'i' and loop 'j'. L_b is bar leakage inductance. L_e is rotor end ring leakage inductance.

Reference [27] suggests when saturation effects included into voltage equations, the L_{ss} terms are function of θ alone while the L_{sr}, L_{rs}, L_{rr} inductances are functions of θ and θ_r. Here, θ is the position of the air gap flux and θ_r is the rotor position. They are both defined with respect to stator reference frame. Thus the derivative of L_{ss} is,

$$\frac{dL_{ss}}{dt} = \frac{dL_{ss}}{d\theta}\frac{d\theta}{dt} \tag{4.13}$$

And the derivatives of the L_{sr}, L_{rs}, L_{rr} are,

$$\frac{dL_{sr}}{dt} = \frac{\partial L_{sr}}{\partial \theta}\frac{d\theta}{dt} + \frac{\partial L_{sr}}{\partial \theta_r}\omega_r \tag{4.14}$$

$$\frac{dL_{rs}}{dt} = \frac{\partial L_{rs}}{\partial \theta}\frac{d\theta}{dt} + \frac{\partial L_{rs}}{\partial \theta_r}\omega_r \tag{4.15}$$

$$\frac{dL_{rr}}{dt} = \frac{\partial L_{rr}}{\partial \theta} \frac{d\theta}{dt} + \frac{\partial L_{rr}}{\partial \theta_r} \omega_r \tag{4.16}$$

ω_r is rotor rotating mechanical speed which is given as:

$$\omega_r = \frac{d\theta_r}{dt} \tag{4.17}$$

If damping is neglected in the model, the following mechanical equation could be established:

$$T_e = J \frac{d\omega_r}{dt} + T_l \tag{4.18}$$

T_e is the electromagnetic torque, T_l is load torque, J is inertia. The following equation could help to compute electrical torque:

$$T_e = \left[\frac{\partial W_{co}}{\partial \theta_r} \right] \tag{4.19}$$

Also, in a linear magnetic system, the co-energy W_{co} is equal to the stored magnetic energy which could be expressed in the following equation:

$$W_{co} = \frac{1}{2} \left[I_s^t \frac{\partial L_{ss}}{\partial \theta_r} I_s + I_s^t \frac{\partial L_{sr}}{\partial \theta_r} I_r + I_r^t \frac{\partial L_{rs}}{\partial \theta_r} I_s + I_r^t \frac{\partial L_{rr}}{\partial \theta_r} I_r \right] \tag{4.20}$$

According to all the equations obtained above, one would be able to write the state space equations in matrix form as follows:

$$\dot{X} = AX + BU \tag{4.21}$$

where

$$X = \begin{bmatrix} i_a \\ i_b \\ i_{r1} \\ i_{r2} \\ \vdots \\ i_{re} \\ \omega_r \\ \theta_r \end{bmatrix}, \text{ and } U = \begin{bmatrix} v_{ab} \\ v_{bc} \\ 0 \\ \vdots \\ \frac{T_e - T_l}{J} \\ 0 \end{bmatrix} \tag{4.22}$$

4.2 Turns Functions and Inductance Profiles of a Healthy Machine

As can been seen from above analysis, state space description of induction machine will require the derivation of various self and mutual inductances. Hence, first efforts were made to obtain turns functions of stator windings and rotor loops which are critical in inductances computation [55]. Space distributions of a phase winding and rotor loop are sketched for the purpose of deriving turns functions. In order to achieve meaningful comparison between simulation and experiments, the induction machine model simulated here has the same parameters as that of experiment. The cross section of stator phase 'a' is shown as Fig. 4.1.

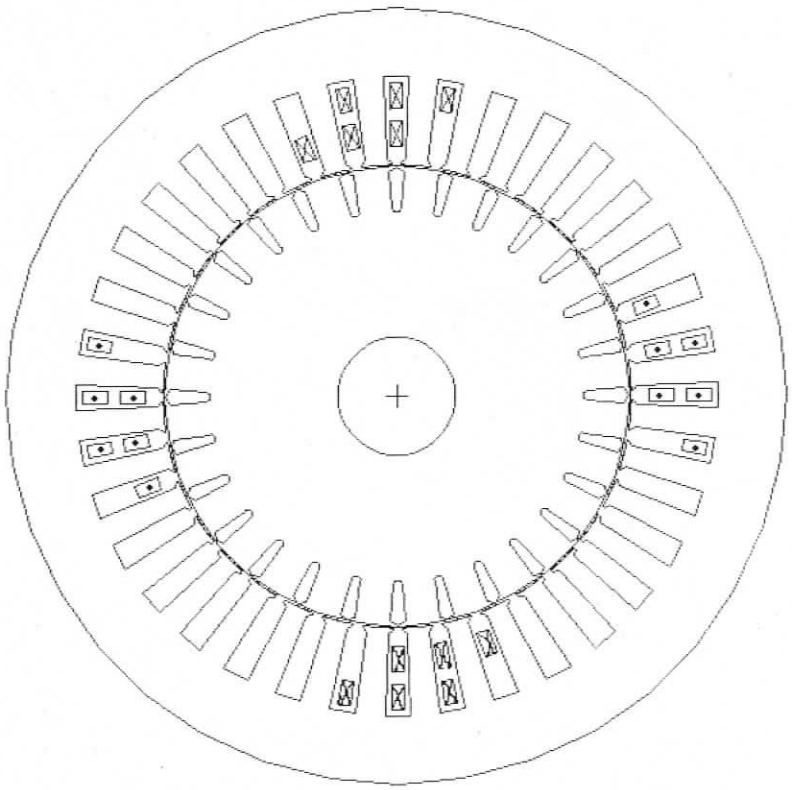

Fig. 4.1 Cross section of stator phase 'a' winding and rotor bar distribution: 'x' indicates current goes into cross section plane, '•' Indicates current comes out of cross section plane.

4.2.1 Turns Functions of Stator Phase 'a'

Based on the winding layout of phase 'a' displayed in Fig 4.1, turns functions of phase 'a' can be expressed as,

$$n_a(\phi) = \sum_{p=1,3,5...}^{\infty} \left(\frac{4N}{3\pi p} \sin\frac{\pi p}{3} + \frac{8N}{3\pi p} \sin\frac{4\pi p}{9} \right) \cos(2p\phi) + \frac{3N}{2}; \quad N = 21 \tag{4.23}$$

N is stator turns in series; ϕ is the stator position measured from phase 'a' axis. Fig. 4.2 shows the turns functions of stator phase 'a'

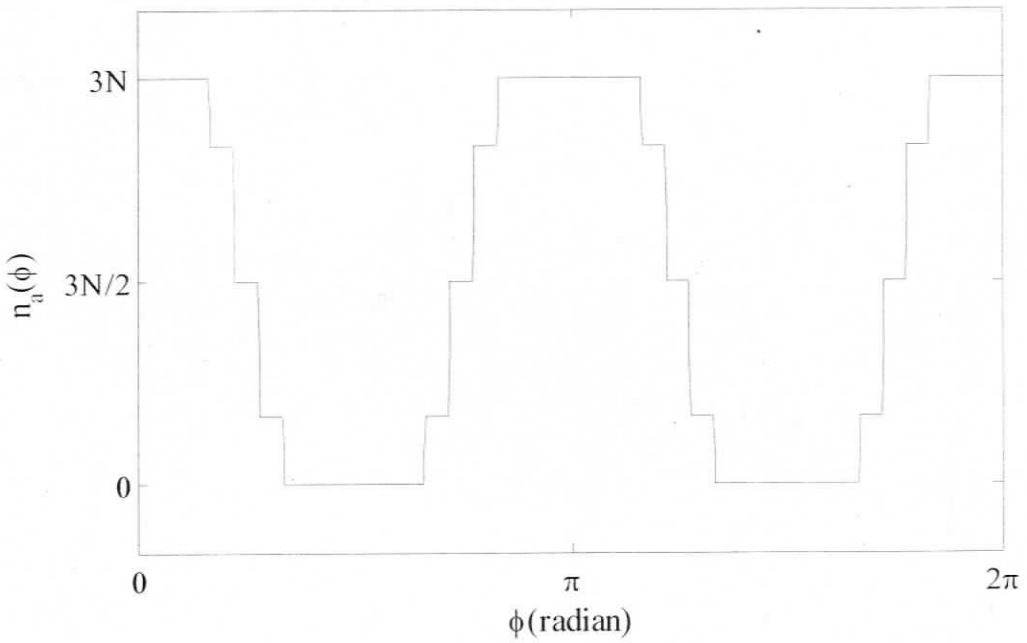

Fig. 4.2 Turns function of phase 'a'.

4.2.2 Turns Functions of Rotor Loop '1'

Turn function of rotor loop 1 can be given as:

$$n_{rj}(\phi, \theta) = \frac{\alpha}{2\pi} + \sum_{h=1,2,3}^{\infty} \frac{4}{\pi h^2 \beta} \sin(\frac{h\alpha}{2}) \sin(\frac{h\beta}{2}) \cos[h(\phi - (j-1)\alpha - \theta)] \tag{4.24}$$

$j = 1, 2, \ldots 28$

where $\alpha = 2\pi/R$, R is the number of rotor bars, β is the skewing angle.

Fig. 4.3 shows the turns functions of rotor loop '1'. The effect of rotor bar skew can be clearly seen from the plot.

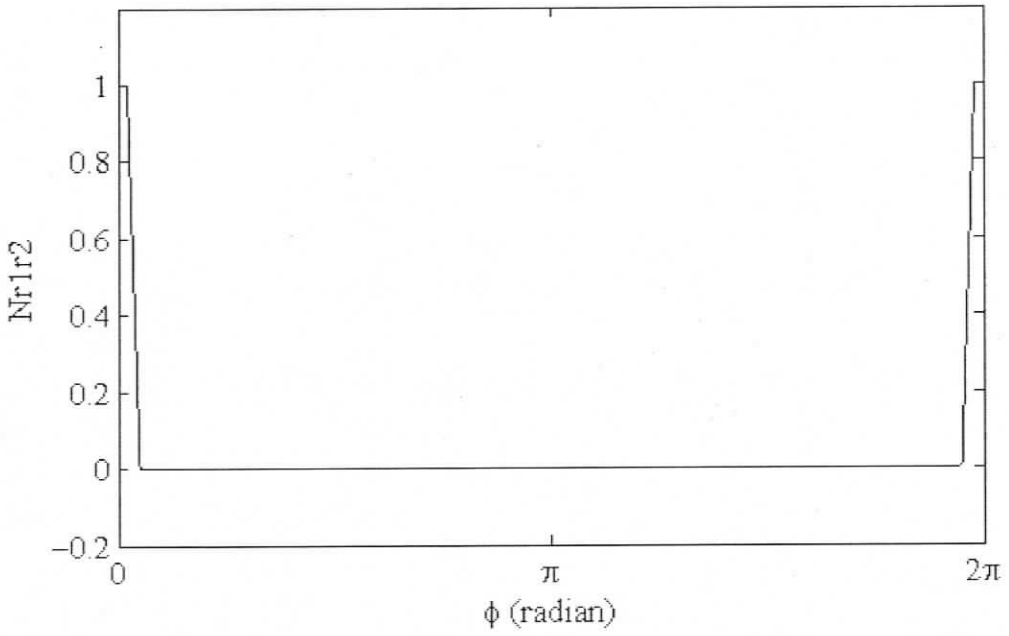

Fig. 4.3 Turns function of rotor loop '1'.

4.2.3 Effective Air-Gap Length with Saturation Effect Incorporated

Due to the effect of saturation, air gap length between stator and rotor need to be modified. The air-gap function g_s and inverse air-gap function g_s^{-1} can be defined following [27], [48].

$$g_s(\phi,\theta) \approx g'\left[1 - k_{gsat} Cos\{2(p\phi - \theta)\}\right] \tag{4.25}$$

$$g_s^{-1}(\phi,\theta) \approx \frac{1}{g'}\left[1 + k_{gsat} Cos\{2(p\phi - \theta)\}\right] \tag{4.26}$$

where g' is modified average air-gap length. k_{gsat} is saturation factor. Equations (4.25) and (4.26) are based on the assumption that saturation will modulate the air-gap permeance at twice the frequency of the air-gap flux density wave. Fig. 4.4 shows the relevant position of normalized fundamental air-gap flux density B, g_s and g_s^{-1} around the air-gap (4 pole

machine). Obviously, the maxima position of g_s^{-1} coincides with the negative and positive going zero crossing of the air-gap flux density.

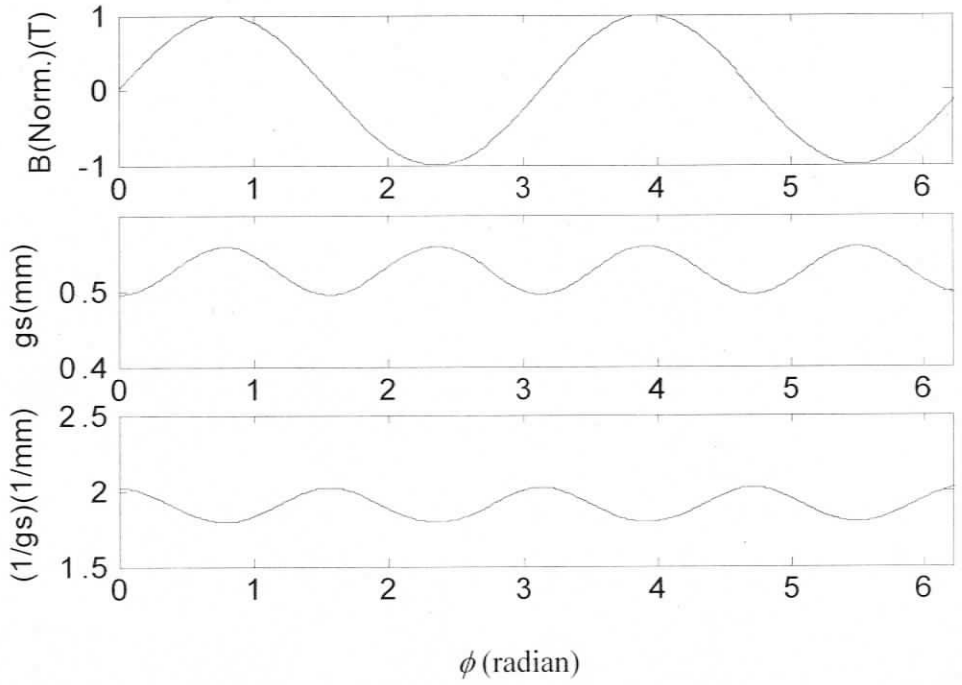

Fig. 4.4 Idealized sketch of normalized air – gap flux density (top), g_s (middle) and g_s^{-1} (bottom). ϕ is in mechanical radians.

Usually k_{gsat} is small enough that (4.26) can be simply derived by inverting (4.25). Its value can be approximately computed via taking the ratio of full load and no load air gap voltage and then using the procedure proposed in [48].

4.2.4 Computation of Stator Inductances of Induction Machine Using MWFA

According to the turns functions and effective air-gap functions obtained above, one can now solve for various inductances of stator phase winding and rotor loops, respectively [55].

$$L_{11} = \mu_0 rl \int_0^{2\pi} \left[(N_1(\phi))^2 g_s^{-1}(\phi, \theta) \right] d\phi \tag{4.27}$$

$$L_{12} = \mu_0 rl \int_0^{2\pi} \left[N_1(\phi) N_2(\phi) g_s^{-1}(\phi, \theta) \right] d\phi \tag{4.28}$$

where,

μ_o is the permeability of the free space; r is the radius of the rotor; l is the stack length; $N_1(\phi)$, $N_2(\phi)$ are the winding functions of windings '1' and '2' respectively; L_{11} is the magnetizing inductance of phase '1' and L_{12} is the mutual inductance between windings '1' and '2'.

When saturation is considered, the magnetizing and mutual inductance of stator phase winding would be functions of air gap flux density position θ, as can be seen from Fig. 4.5 and Fig. 4.6:

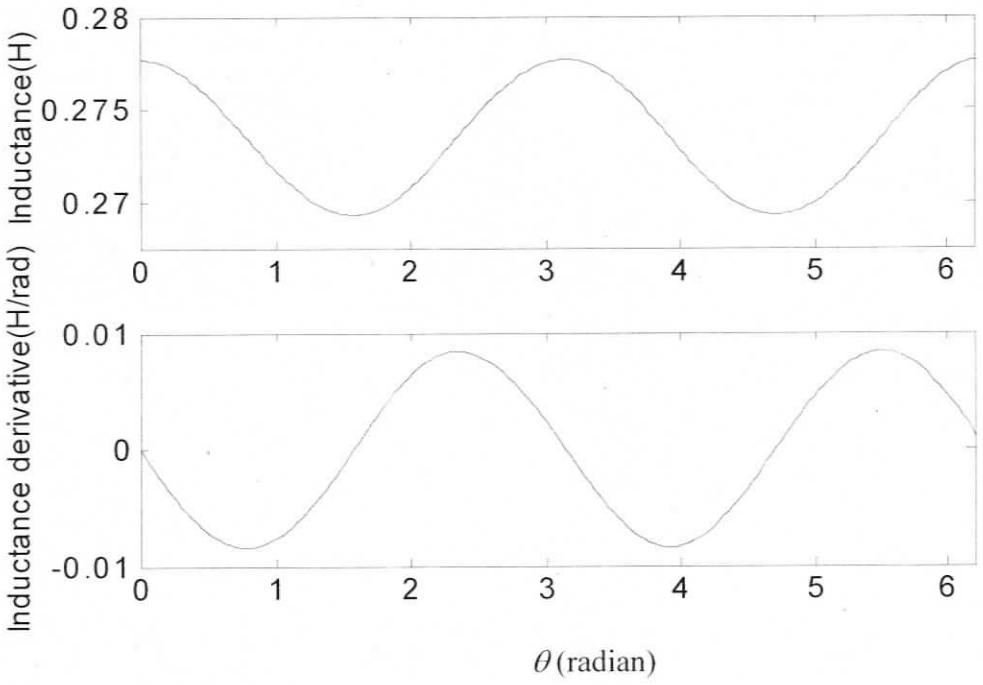

Fig.4.5 Magnetizing inductance of stator phase 'a' and its derivative (bottom) $K_{gsat} \approx 0.06$.

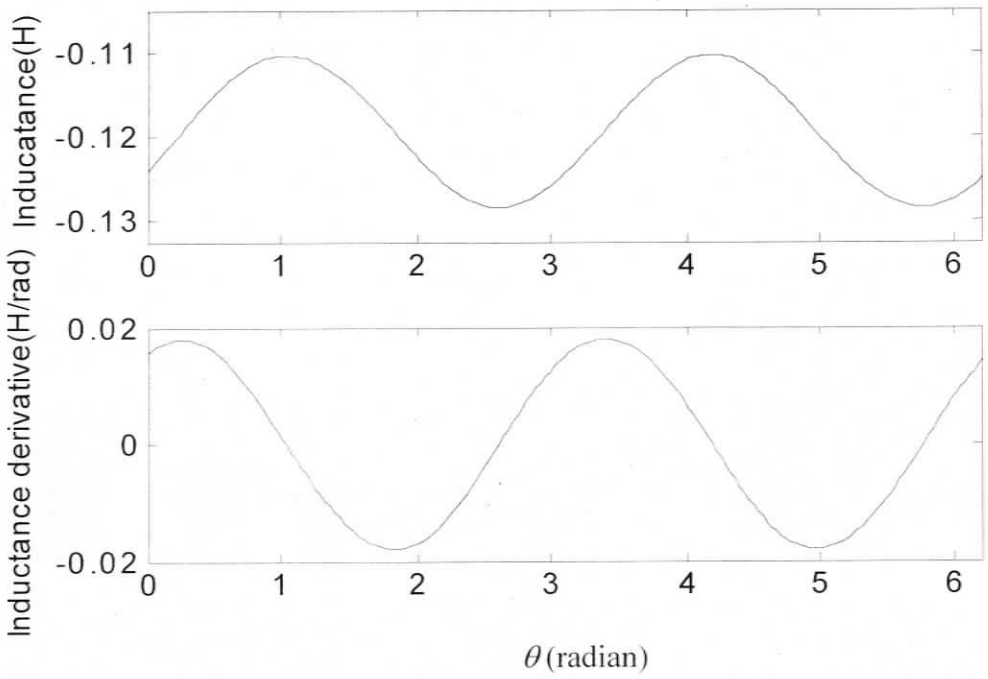

Fig. 4.6 Mutual inductance between stator phases 'a' and phase 'b' and its derivative (bottom). $K_{gsat} \approx 0.06$.

Magnetizing inductances of rotor loops, mutual inductances between stator winding and rotor loops as well as mutual inductances between different rotor loops will be the functions of both θ and θ_r. According to [27], their partial derivation with respect to θ and θ_r will both be used in the voltage equations, but only the partial derivative with respect to θ_r is used in torque computation. Some 3-D inductances and their partial derivative profiles are shown below.

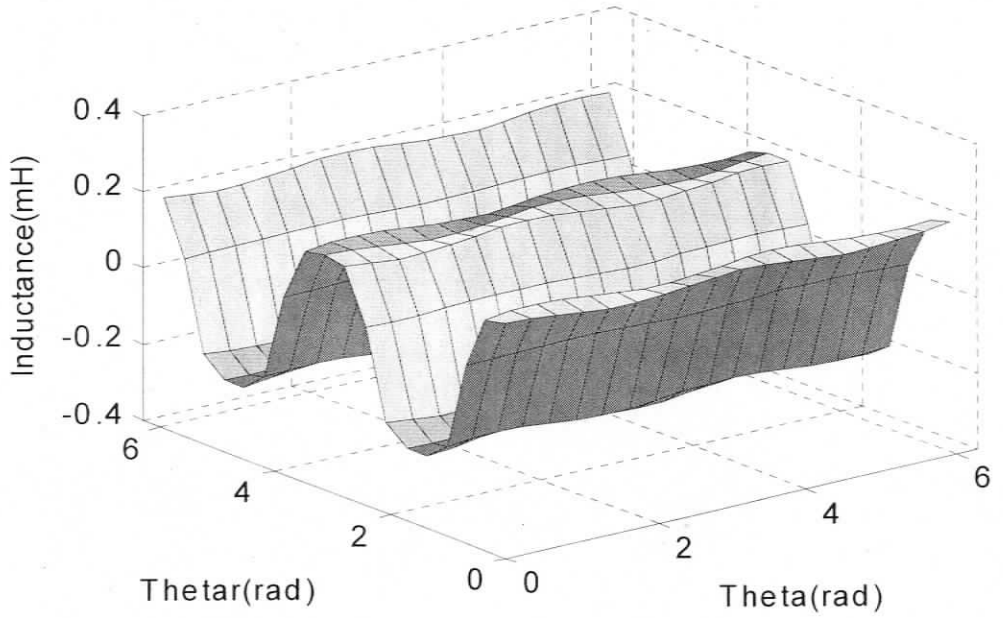

Fig. 4.7 Inductance profile between stator phase 'a' and rotor loop '1'. $K_{gsat} \approx 0.06$.

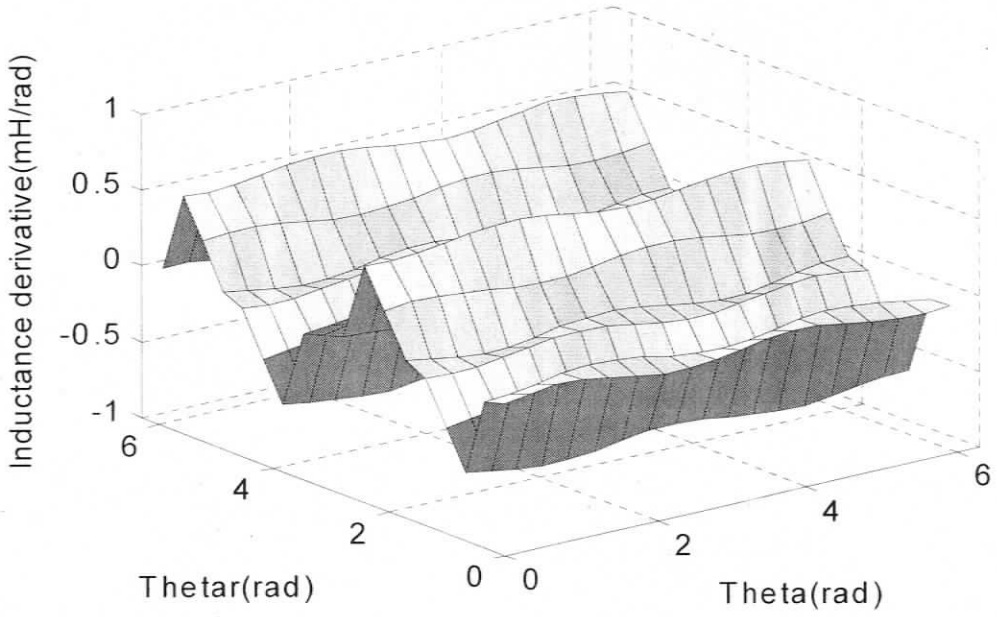

Fig.4.8 Partial derivative of inductance profile between stator phase 'a' and rotor loop '1' with respect to θ_r. $K_{gsat} \approx 0.06$.

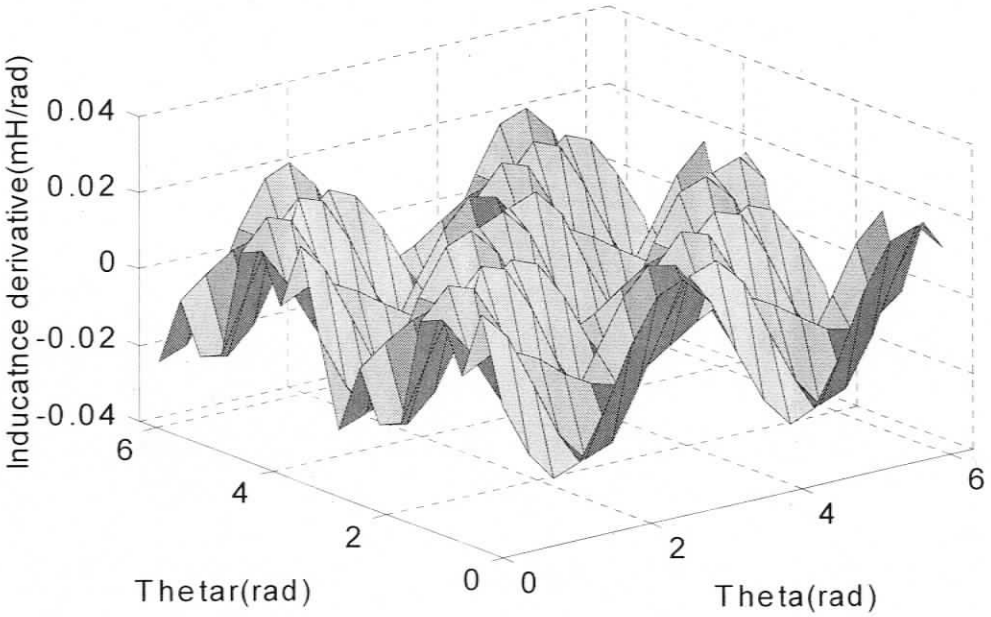

Fig.4.9 Partial derivative of inductance profile between stator phase 'a' and rotor loop '1' with respect to θ. $K_{gsat} \approx 0.06$.

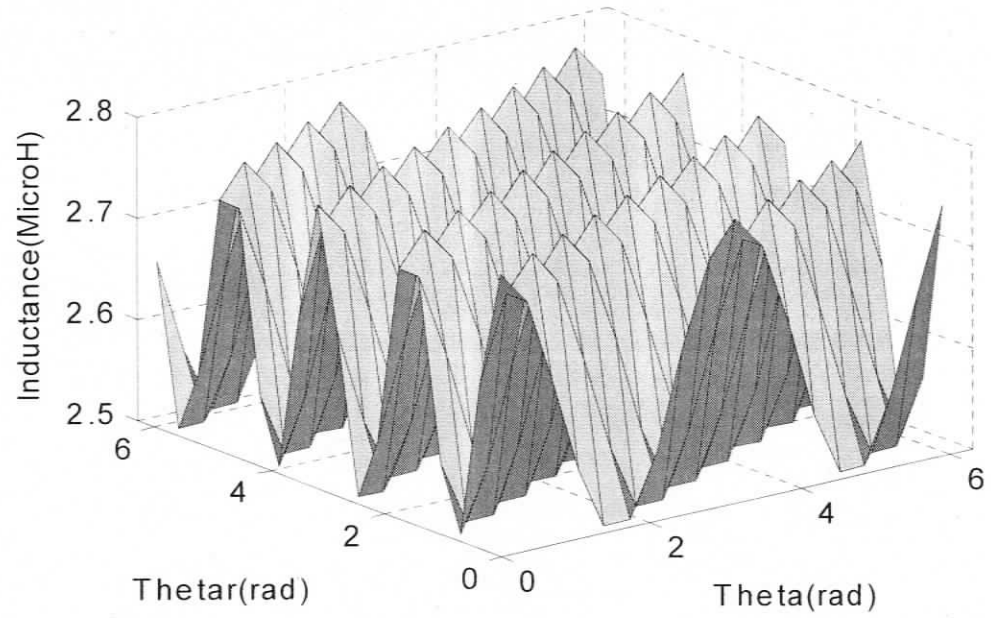

Fig. 4.10 Magnetizing inductance profile for rotor loop '1'. $K_{gsat} \approx 0.06$.

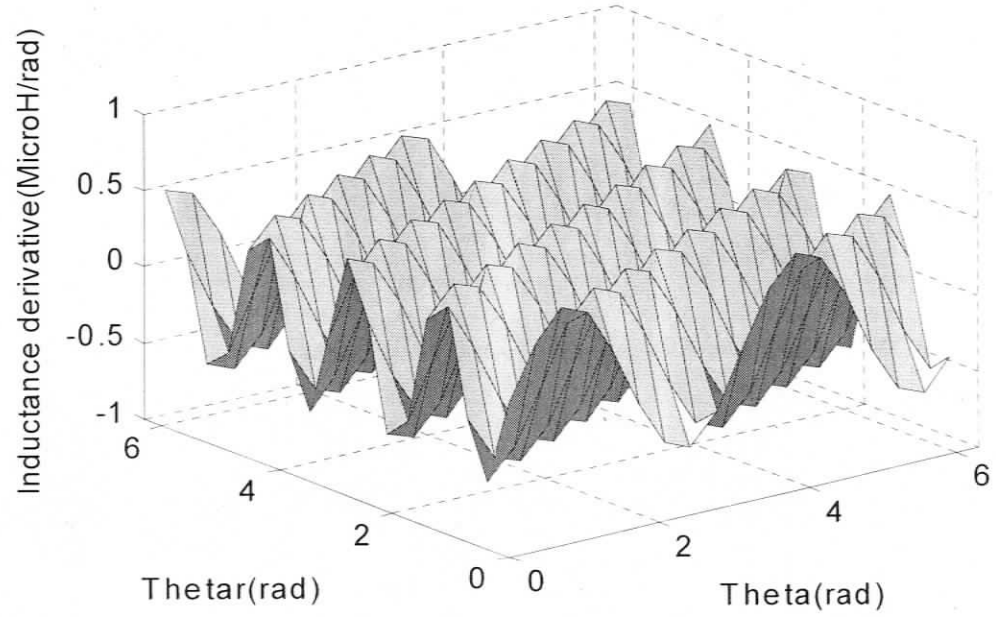

Fig. 4.11 Partial derivative of magnetizing inductance profile for rotor loop '1' with respect to θ_r. $K_{gsat} \approx 0.06$.

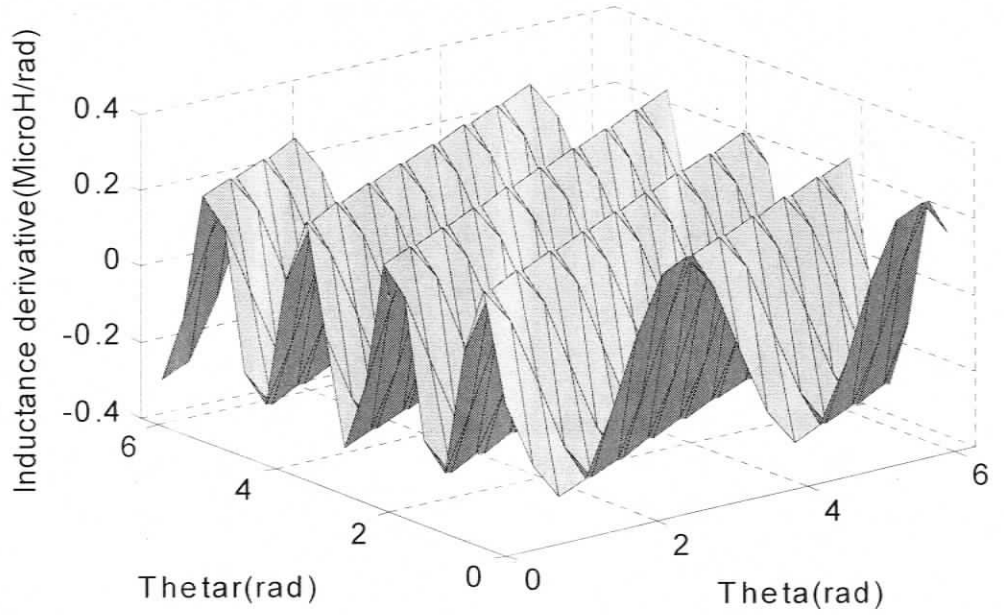

Fig. 4.12 Partial derivative of magnetizing inductance profile for rotor loop '1' with respect to θ. $K_{gsat} \approx 0.06$.

4.3 Dynamic Simulation of Induction Machine

After all the mutual and self inductances have been calculated, the state space model of induction machine can be simulated with one of the built-in MATLAB ordinary differential equation (ODE) solvers. The start-up characteristics of the induction machine can be illustrated by phase 'a' current, rotor bar loop '1' current, rotor rotating speed and position respectively. They are plotted in Fig. 4.13 - 4.16.

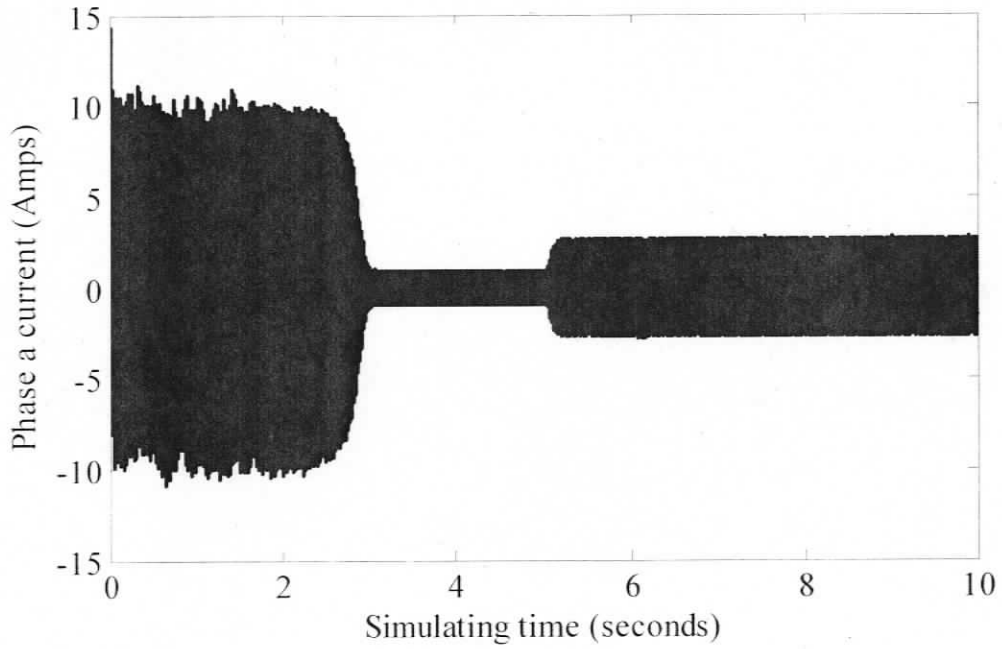

Fig. 4.13 Simulated stator phase a current 'i_a' from start, full load was applied at 5 second.

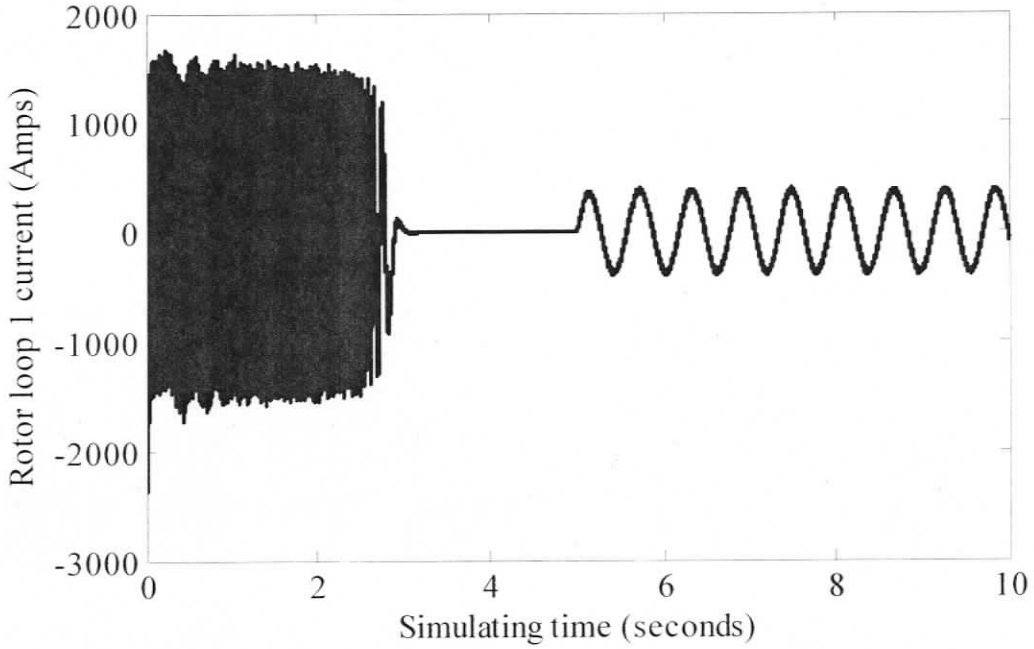

Fig. 4.14 Simulated rotor loop 1 current 'i_{r1}' from start, full load was applied at 5 second.

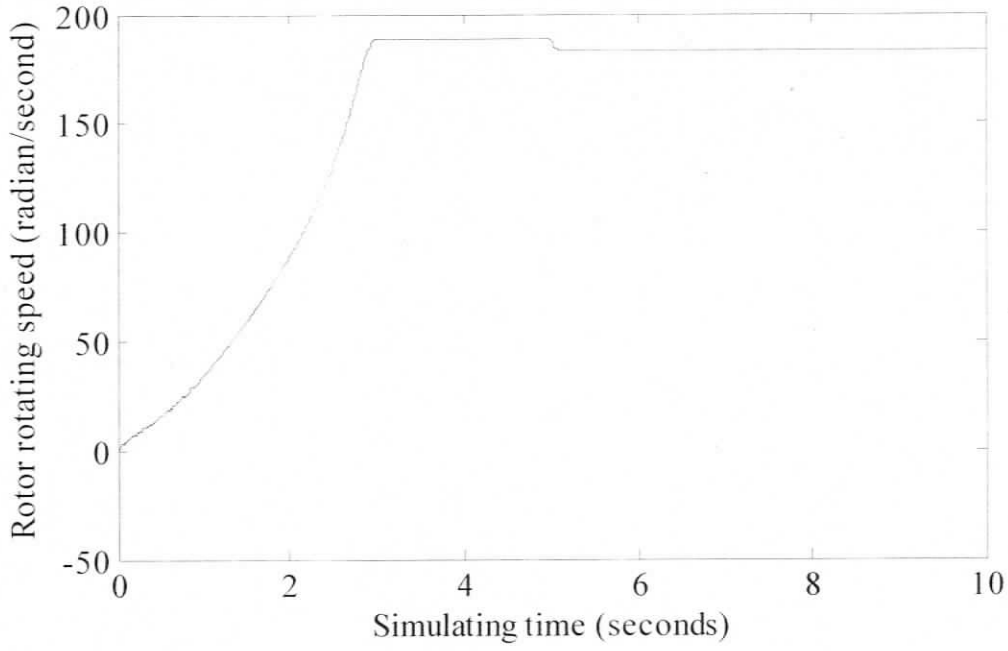

Fig. 4.15 Simulated rotor mechanic speed 'ω_r' from start, full load was applied at 5 second.

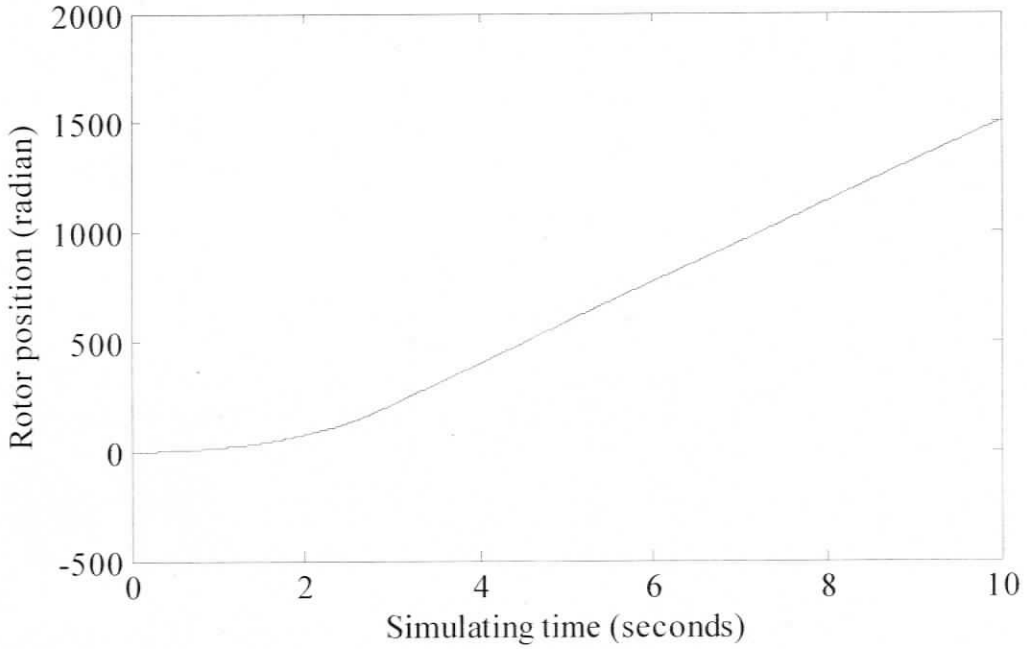

Fig. 4.16 Simulated rotor position 'θ_r' from start, full load was applied at 5 second.

Figs. 4.13 – 4.16 have been obtained by feeding the model with harmonics free supply voltages. Full load is applied after 5 seconds. The starting and loading transients of the motor clearly can be seen. In Figs. 4.17. 4.18, the waveforms of no load and full load line currents under steady-state conditions are displayed. The solver used is ODE 45.

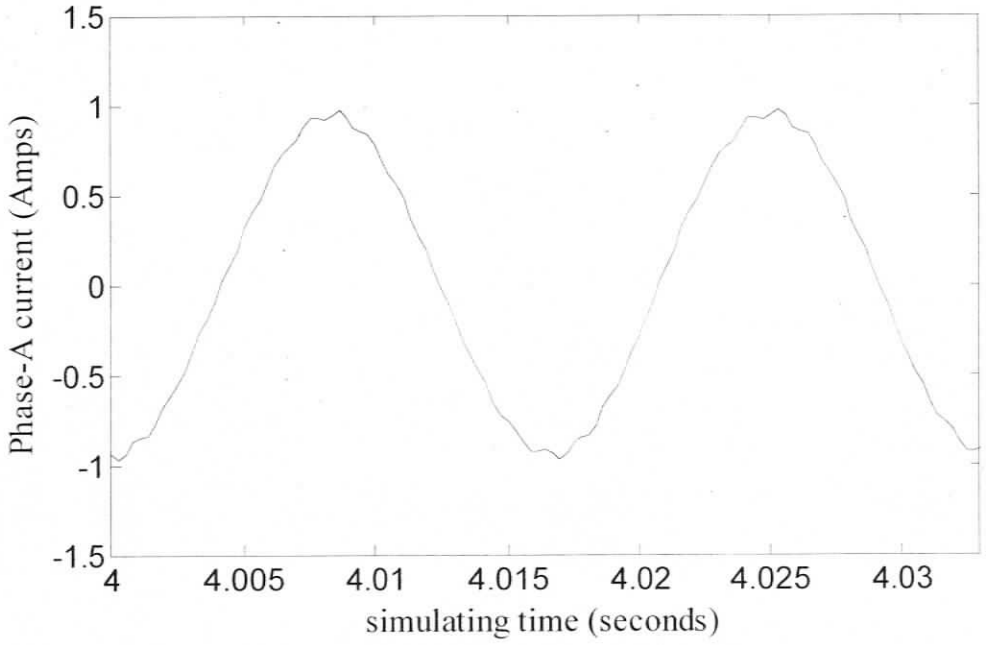

Fig. 4.17 Simulated static state two cycle of stator phase 'a' current 'I_a' under no load.

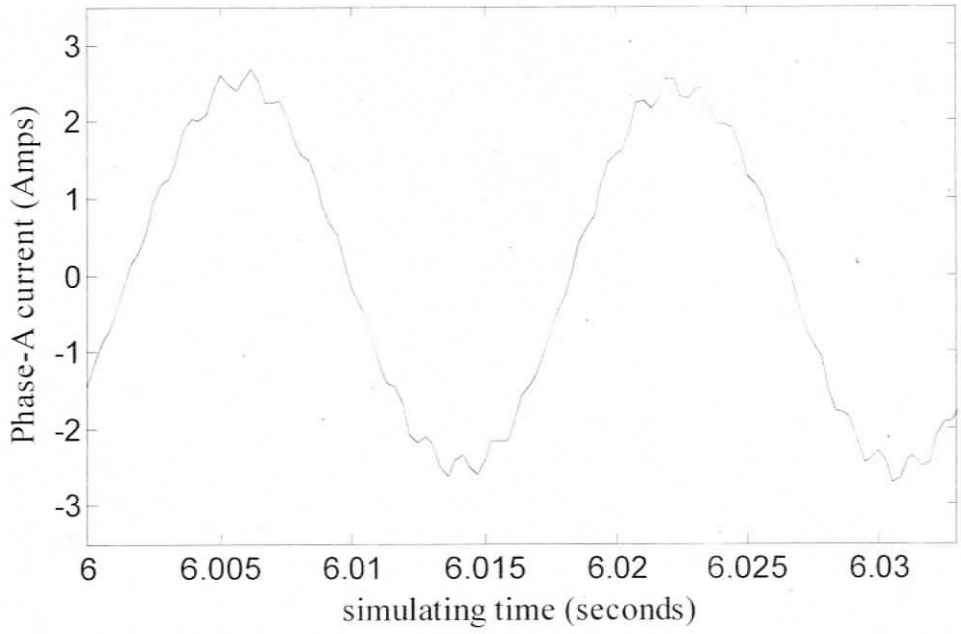

Fig. 4.18 Simulated static state two cycle of stator phase 'a' current 'I_a' under full load.

In Figs. 4.17 and 4.18. the ripples associating with the sinusoidal waveforms indicate that the simulated line current under steady state has higher order harmonics that are slot

related. They are not expected to influence the ±3f components. In the following section, ±3f harmonics analysis by using simulated line current data is conducted.

4.4 Simulated Line Current ±3f Fault Signature Analysis

Initially the model was simulated under ideal balanced and unbalanced voltage condition (harmonics-free). Supply unbalance conditions are introduced by setting three different voltage magnitudes ($0.9\times V$, V and $1.1\times V$, here V is the magnitude of balanced supply voltage). In an attempt to obtain simulated fault signatures under more realistic scenario, this model was later simulated by feeding three phase experimentally collected voltage data (details of realizing supply unbalances and inter-turn faults on induction machines are described in Chapter 5). ±3f signatures are analyzed based on both simulation cases.

4.4.1 Verification of Existence of ±3f Components Based on Line Current Spectra Analysis

Following the space vector analysis given in Chapter 3, simulated three phase line current data are first combined into complex line current space vectors by using equation (3.7). These vectors are then converted into complex frequency-domain signatures through Fourier Transform with the formula given in (3.23). As concluded in chapter 3, theoretically, when fed by ideal balanced three phase power supply, an induction machine associated with perfectly symmetric structure will not generate ±3f components. These components are observable only if the conditions listed below are satisfied:

- Saturation related permeance harmonics are considered and,
- Inherent structural asymmetry and supply unbalance or fault related time harmonics are included.

Moreover, the amplitude of +3f signature is different from that of -3f signature as the order of time and permeance harmonics from which they are introduced are different. Hence, these two components will have different residues in detecting inter-turn faults

when computed following methods proposed in previous chapter. Figs. 4.19 and 4.20 display different complex line current spectra under a variety of operating conditions.

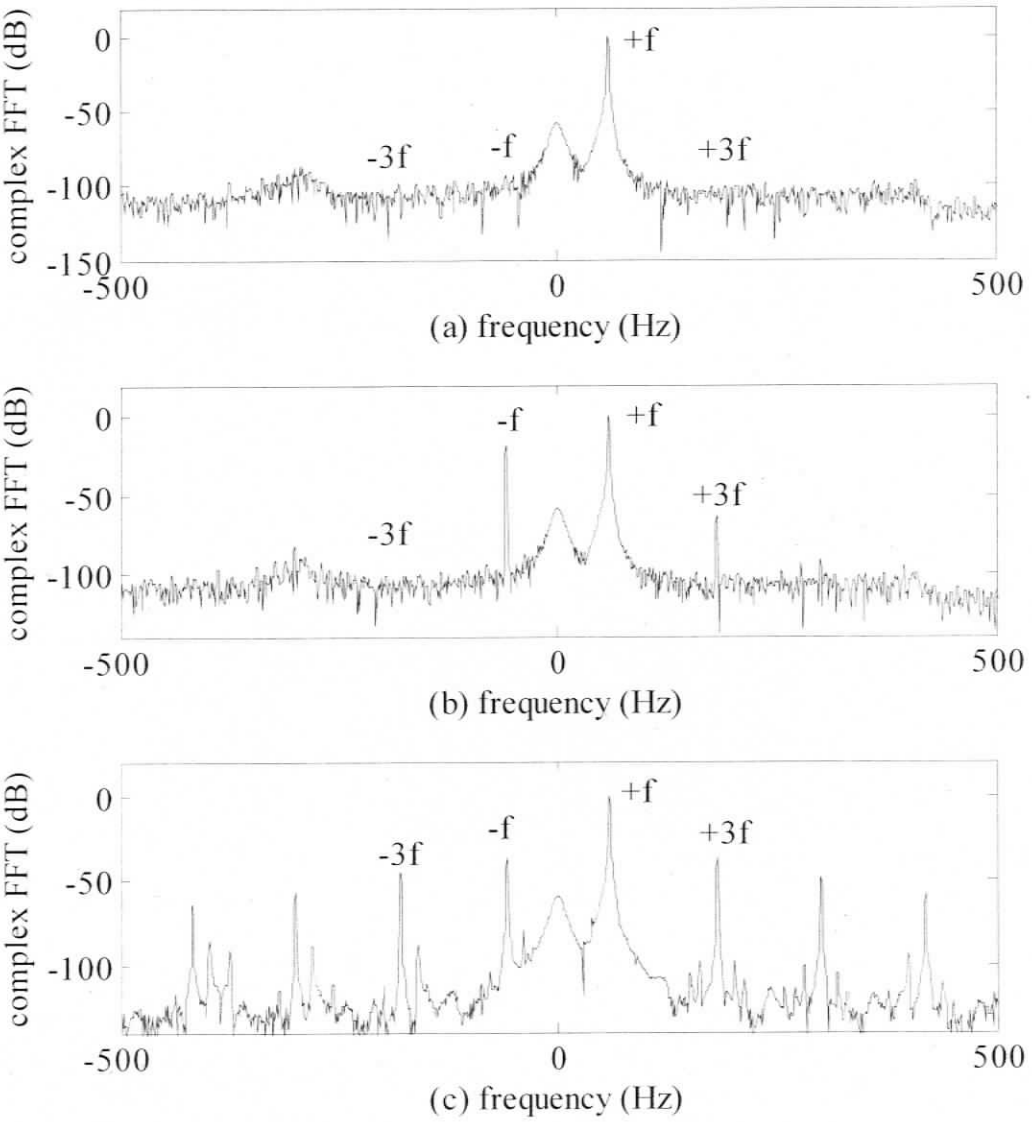

Fig 4.19 Simulated line current spectra under full load conditions: healthy machine with ideally balanced supply (top); healthy machine with unbalanced supply (middle); single-turn fault machine with balanced supply (bottom); simulated by harmonics-free voltage data.

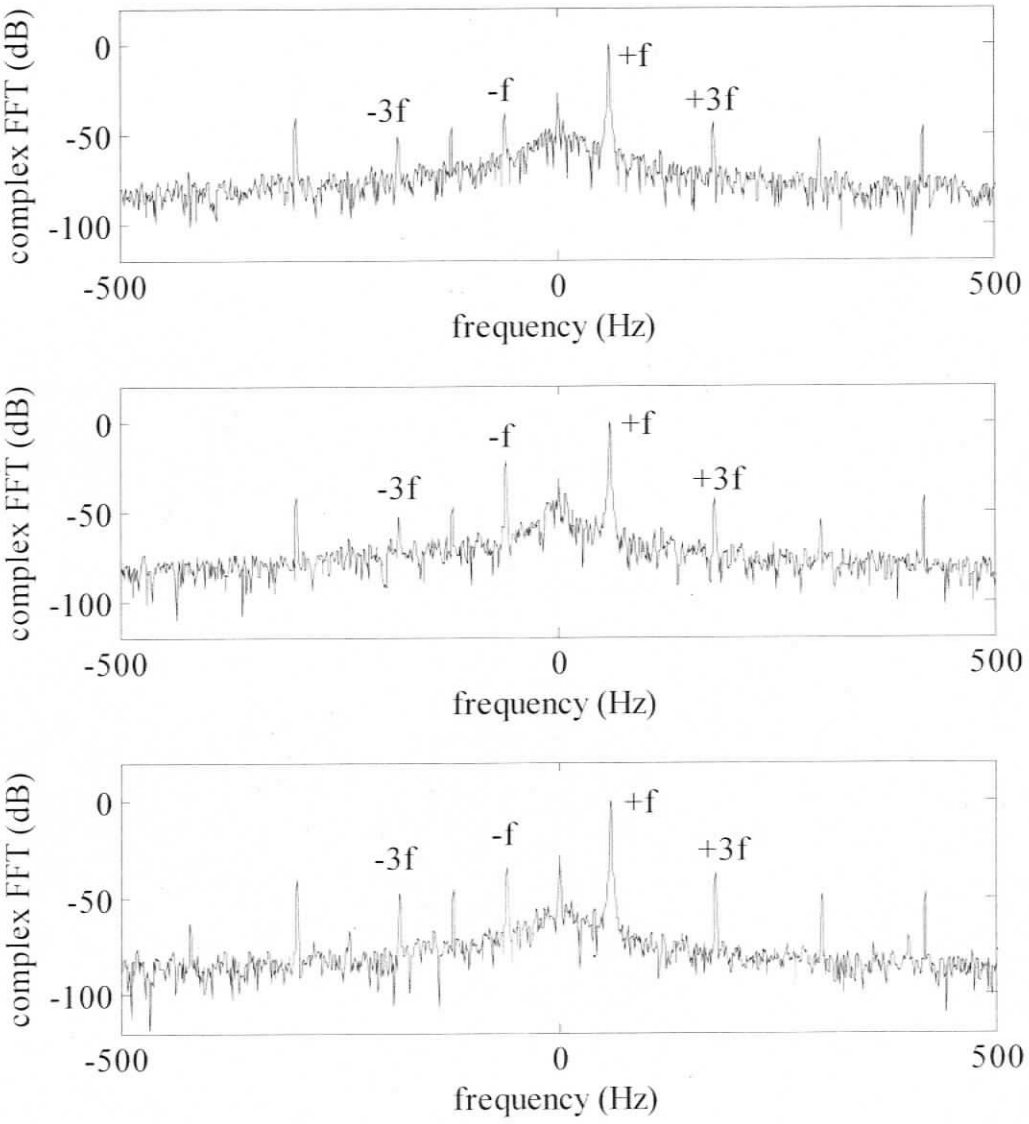

Fig 4.20 Simulated line current spectra under full load condition: healthy machine with balanced supply (top); healthy machine with unbalanced supply (middle); single-turn fault machine with balanced supply (bottom); simulated by experimentally collected voltage data.

In Fig 4.19, complex line current spectra obtained from harmonics-free input voltages are displayed. Clearly, ±3f line current harmonic components will not be introduced for a healthy model supplied by balanced three phase voltages as shown in the top plot in Fig.

4.19. On the contrary, a healthy machine driven by unbalanced supply or a faulty machine will contribute to the presence of ±3f line current harmonics as shown in the middle and bottom plots of Fig 4.19. Also it is noted that normalized magnitude of -3f component is different from that of +3f component under all operating conditions. For instance, a substantial increase of +3f can been seen when balanced power supply is replaced by unbalanced power supply. -3f, however, does not show recognizable difference between these two cases. Explanation can be found from Table 3.7. Supply unbalance will introduce fundamental reverse rotating field which gives rise to +3f while interacting with fundamental permeance harmonic. All odd harmonics are showing up in the bottom plot of Fig. 4.19. This can easily be explained from Table 3.3 and 3.4 that fault gives rise to all the odd flux density harmonics associating with matching pole pair numbers. ±3f component in Figs. 4.20 are all observable with different amplitudes, indicating that when a real three phase supply voltages are supplied, all the inherent time harmonics (including ±3f voltage components) and supply unbalances will be involved and they will give rise to different values of ±3f component under even a healthy machine with balanced supply voltages. Figs. 4.19 and 4.20 show the simulated line current spectra under full load conditions. The spectra associated with no load conditions are given in Appendix C. All the resulting spectra are able to validate the theoretical analysis of chapter 3.

4.4.2 Simulated Fault Detection Scheme Based on Residue Elimination Technique

Spectra showing in Figs. 4.19 and 4.20 validate the theoretical analysis of ±3f components under different conditions. It has been concluded from Fig. 4.20 that due to inherent structural asymmetry and supply unbalance, different values of ±3f components will exist under condition of healthy machine fed by balanced supply voltages. These components will bring ambiguity in detecting stator fault. Therefore, following the residue analysis in chapter 3, these components are estimated using (3.36) and (3.37) and subtracted from measured ±3f fault signatures. One balanced data and five unbalanced data are used to compute coefficients in an attempt to minimize influence of supply

unbalance. The differences of resulting fault signatures between + 3f and -3f from simulated current data clearly can be seen from Figs. 4.21 - 4.24.

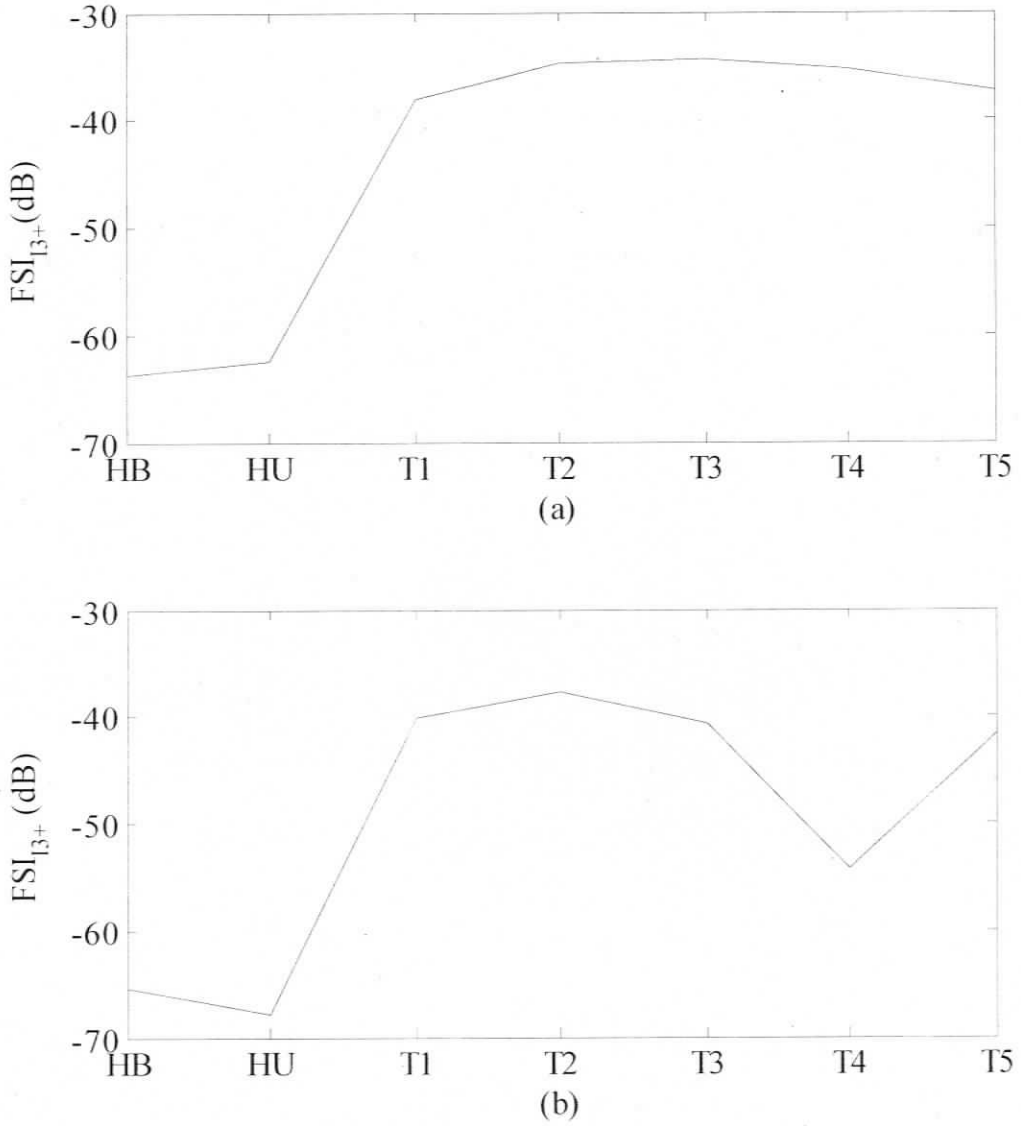

Fig. 4.21 Normalized, residue removed, +3f fault signatures versus fault severities under different load conditions: (a) no load; (b) full load, simulated with harmonics-free three phase voltage data.

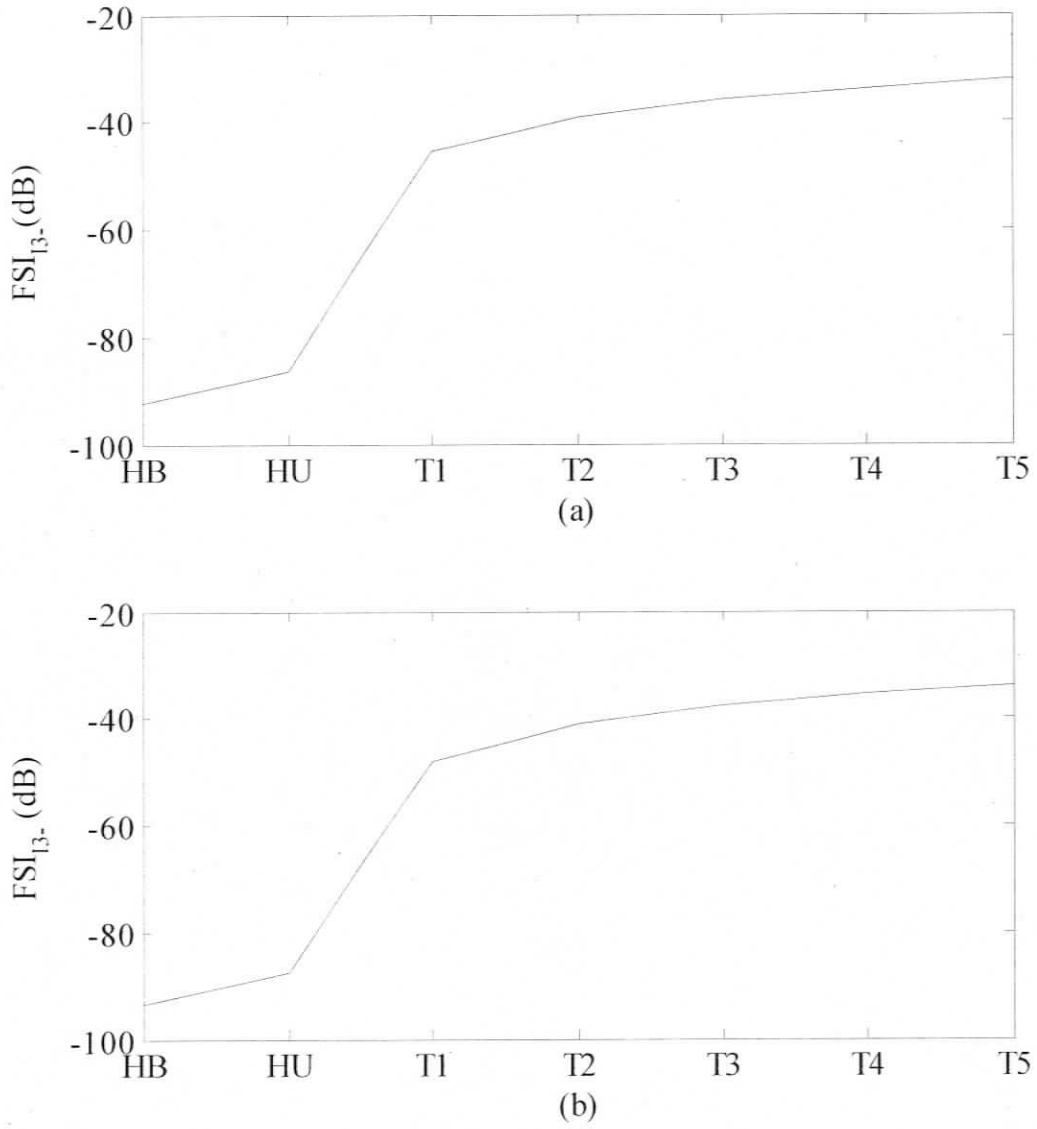

Fig. 4.22 Normalized, residue removed, -3f fault signatures versus fault severities under different load conditions: (a) no load; (b) full load, simulated with harmonics-free three phase voltage data.

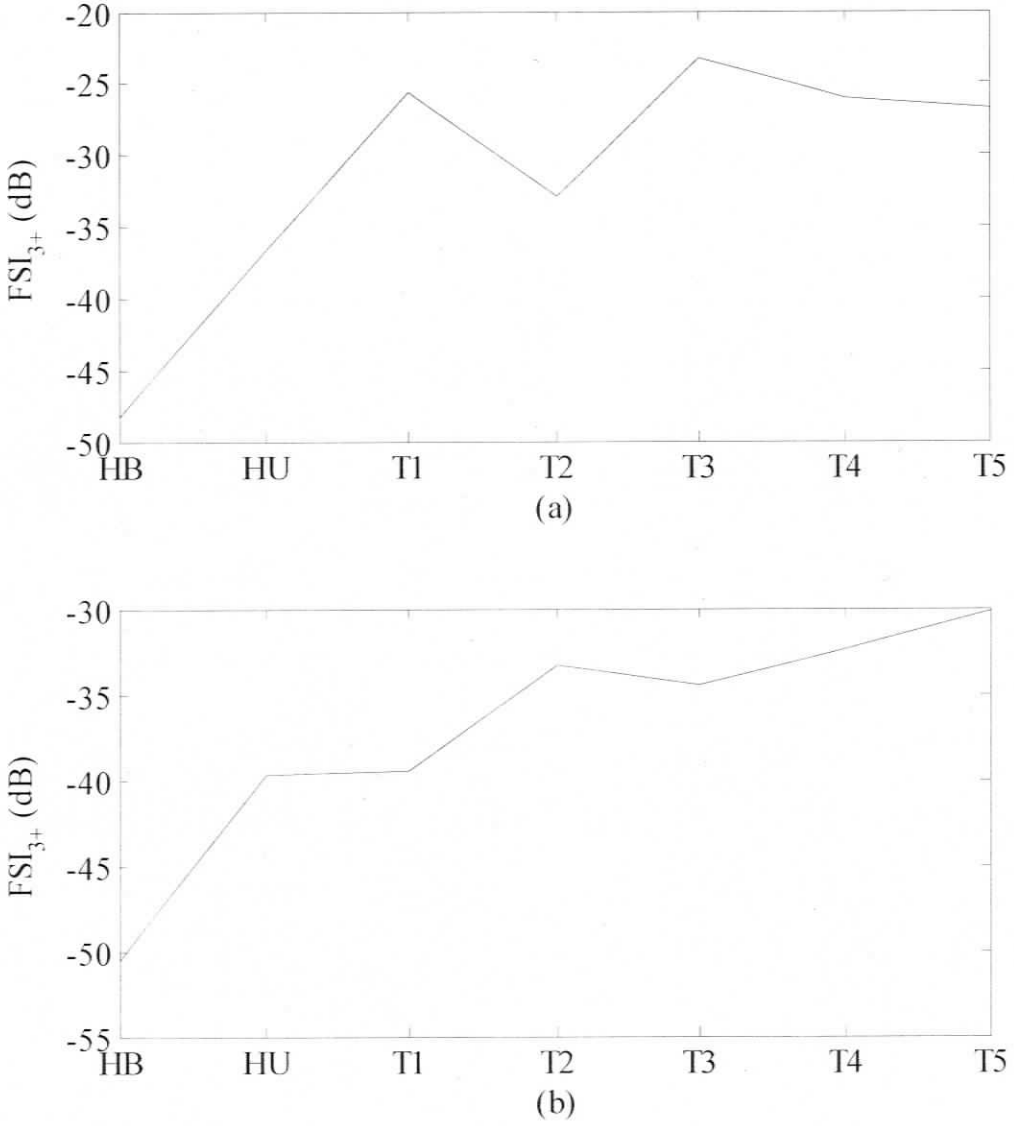

Fig 4.23 Normalized, residues removed, +3f fault signatures versus fault severities under different load conditions: (a) no load; (b) full load; simulated with experimentally collected voltage data.

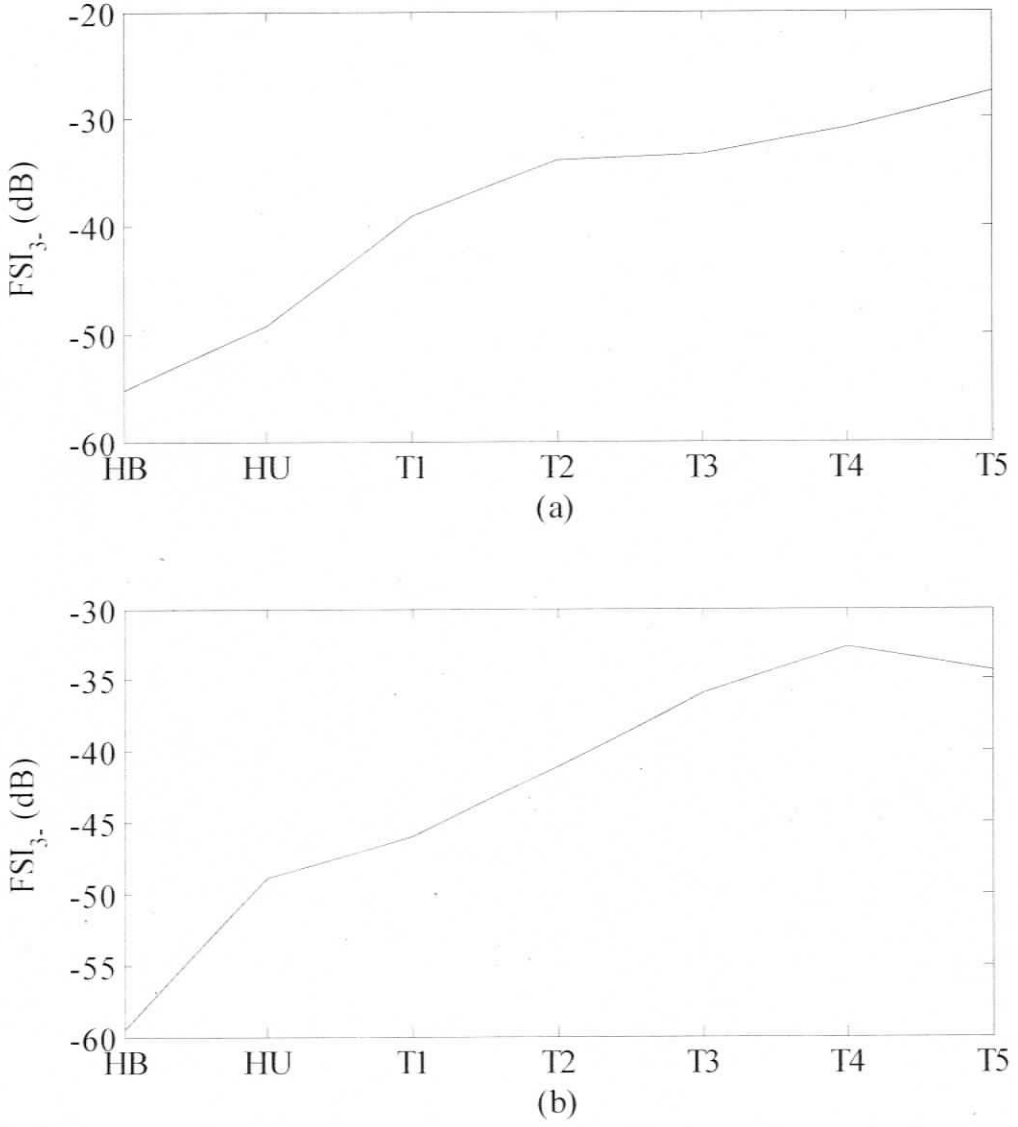

Fig 4.24 Normalized, residues removed, -3f fault signatures versus fault severities under different load conditions: (a) no load; (b) full load; simulated with experimentally collected voltage data.

4.4.3 Evaluation of Simulation Results

Figs. 4.21 - 4.24 obtained in the previous subsection verified the theoretical prediction that the removal of residual ±3f components in line current will minimize the

effect of inherent supply unbalances and hence increase the sensitivities of proposed fault signatures. Further, it is clear the profiles of +3f and -3f fault signatures are following completely different trends. For the simulated cases, -3f fault signatures have better performance in indicating single turn fault under all load conditions. +3f fault signatures, however, display certain ambiguity. Nevertheless, these figures imply that +3f and -3f need to be separately considered for realistic fault detection.

Chapter 5

Experimental Results with Three Phase Line-fed Star-connected Induction Machine

5.1 Introduction to the Squirrel Cage Induction Machine Under Test

In order to validate the theoretical analysis and simulation results obtained earlier, a series of experiments were conducted based on varying operating conditions. In this chapter, the experimental setup was established based upon a three phase dual voltage induction machine. Three phase stator winding schematics of it are shown in Fig 5.1. The machine has been connected in star with two winding in series for the high voltage (460V) mode (Fig 5.2). The detailed specification of the motor has been included in Appendix D.

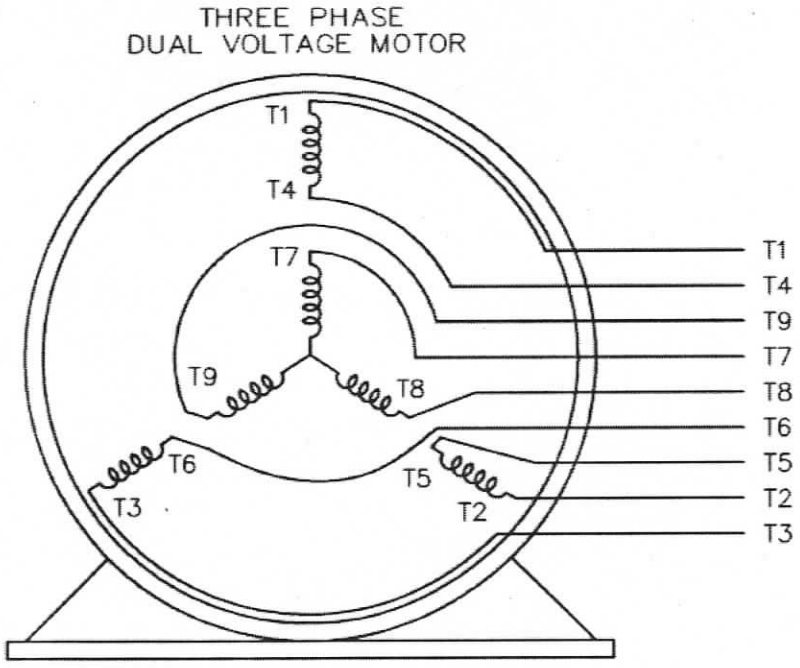

Fig.5.1 Three phase stator winding schematics of dual voltage induction machine.

For the purpose of obtaining experimental data under stator inter-turn faults, the taps have been brought out as given in Fig 5.3. There is one turn between each tap. These taps can be shorted for creating inter-turn fault. For example, to create a one turn fault, tap 1 and 2 are shorted, for two turn faults, taps 1 and 3 are shorted, etc.

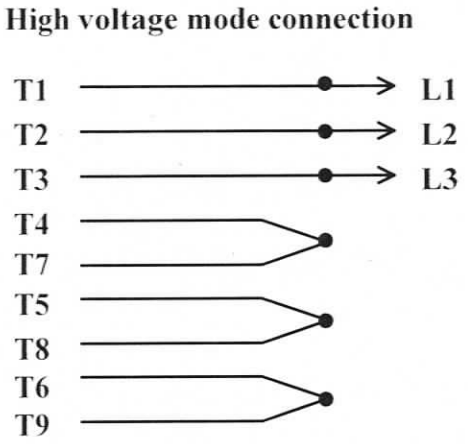

Fig. 5.2 Taps connection scheme for star connected machine.

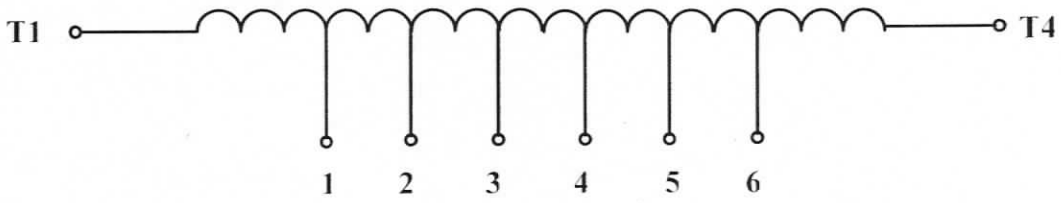

Fig. 5.3 Short-turn creating scheme for line-fed star-connected induction machine.

References [21] and [26] reported that there is a large circulating current in shorted winding which will generate excessive heat. As the result, one cannot short two taps for more than a few seconds as it might destroy the inter-turn insulation and consequently permanently destroy winding and motor. Therefore, as a protective procedure, a contactor with timer was employed to short the loop. The timer operates after a few seconds to open the contactor, so that the heat generated will not do harm to the shorted turn or other areas of the motor. Another point that should be kept in mind is after each fault test, sufficient cooling time (usually a few seconds) should be given before applying the next

short circuit so that the shorted turns and the motor do not suffer from excessive heat build up due to repeated shorted circuit.

5.2 Brief Description of Experimental Setup

In the experimental set-up the three phase voltages come from power supply utility and are fed into a three phase step-up isolation transformer through a three phase variac. The variation in supply unbalance is realized via employing a step-up transformer with three rows of fixed taps on it. When the primary side of transformer is connected to 208 V three-phase power supply, these taps are capable of providing different line voltages such as 448 V, 460 V and 472 V. The variation in three-phase unbalanced voltages can thus be applied to the machine if different taps are selected to connect to the three input terminals of induction machine. These taps are shown in Fig 5.4.

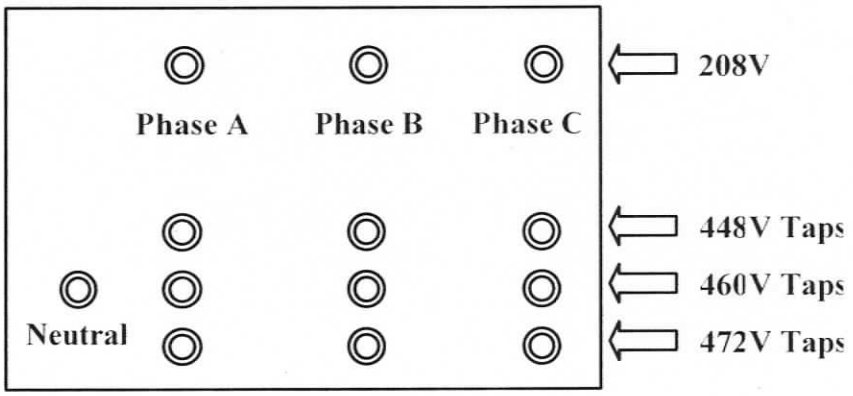

Fig. 5.4 Step-up three phase transformer used for creating supply unbalances.

The variations of loads are achieved by coupling the induction motor with a separately excited DC generator. A group of adjustable resistor modules are connected to the armature winding of the DC generator to vary the motor loading. The field current of the DC generator was supplied from a variable DC power-supply. In order to conveniently observe different load conditions of induction motor, a magnetic disc based speed sensor with digital read out was fixed on the testing bed. The voltage and current data are collected using voltage and current probes attached to a data-acquisition system (DAQ) and fed into a PC. For the purpose of implementing the fault detection scheme in a

practical industry environment, the data acquisition and FFT computation can be done using a real-time digital signal processors (DSP) system. Such a system can also perform other housekeeping function and may be used even to drive converter fed induction motors.

5.3 Analysis of ±3f Fault Signatures for a Practical Machine

As stated earlier, a practical induction motor will have certain magnetic saturation and inherent structural imperfection. In addition, three phase voltages from a practical power supply utility will have inherent unbalance. Also all the time harmonics as described in chapter 3 will be present in line current spectra. In an attempt to verify the theoretical analysis and simulation results, measured ±3f signatures with respect to three cases given as 'HB', 'HU' and 'T1' under two different load conditions, i.e., no load as well as full load conditions are displayed in line current complex spectra. Each spectrum is obtained from averaging of the complex Fourier Transform computed on six contiguous data sets of equal length with each of one sixth of a second duration. Thus the total acquisition time is of one second. Assuming a combined computation and relay trip time is of one second, the total fault clearance time is expected to be around two seconds. The motors tested in lab have been able to withstand 10 – 11 seconds short circuit using external leads without any problem. With adequate tuning of coefficients and faster computation of FFT the fault detection can probably be done within a fraction of a second. The expected cost of such a monitoring and tripping system is expected to be between $500 and $1000. To the best knowledge of the writer, such a sensitive stator fault detection system is not available commercially.

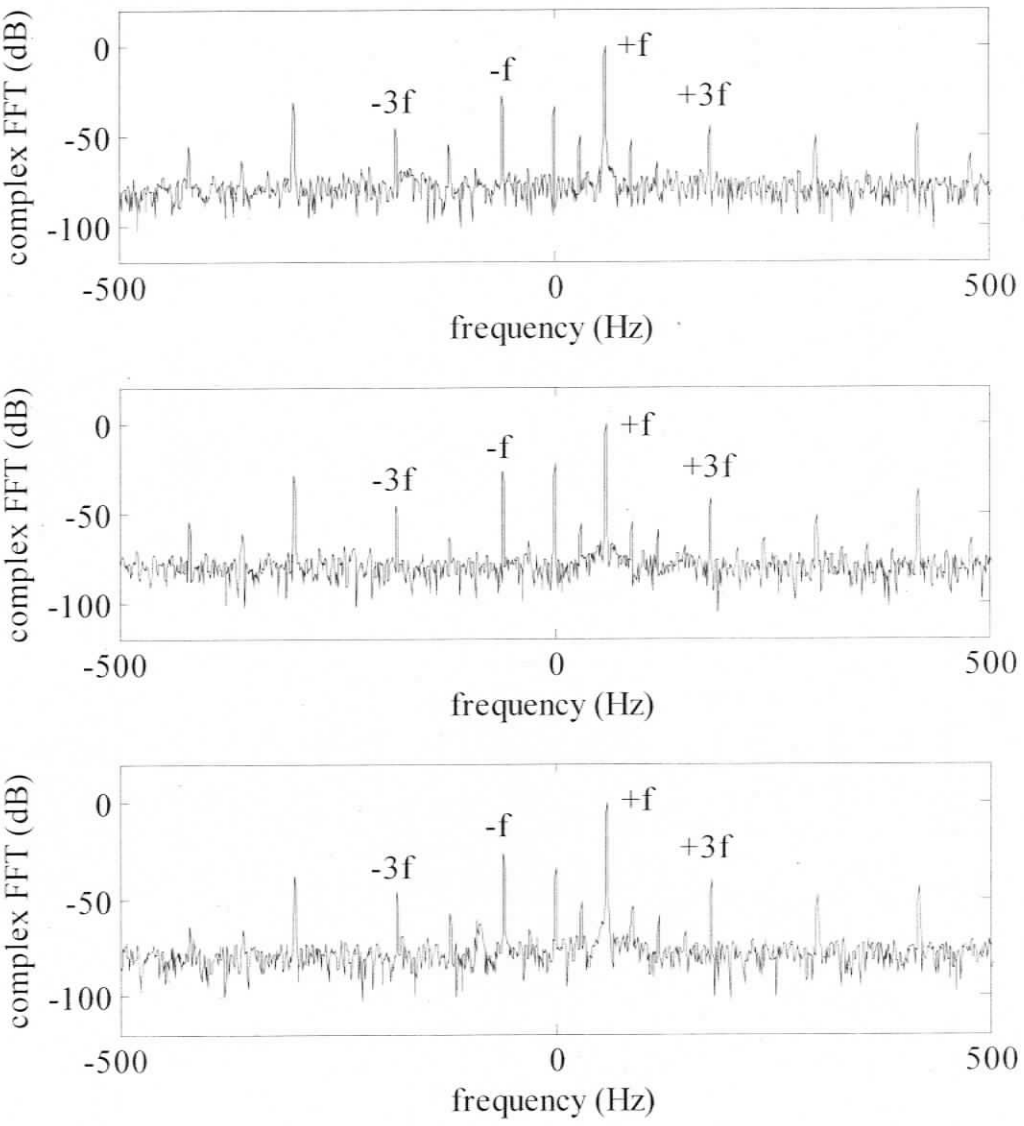

Fig 5.5 Experimentally computed line current spectra under no load condition: healthy machine with balanced supply (top); healthy machine with unbalanced supply (middle); single-turn fault machine with balanced supply (bottom).

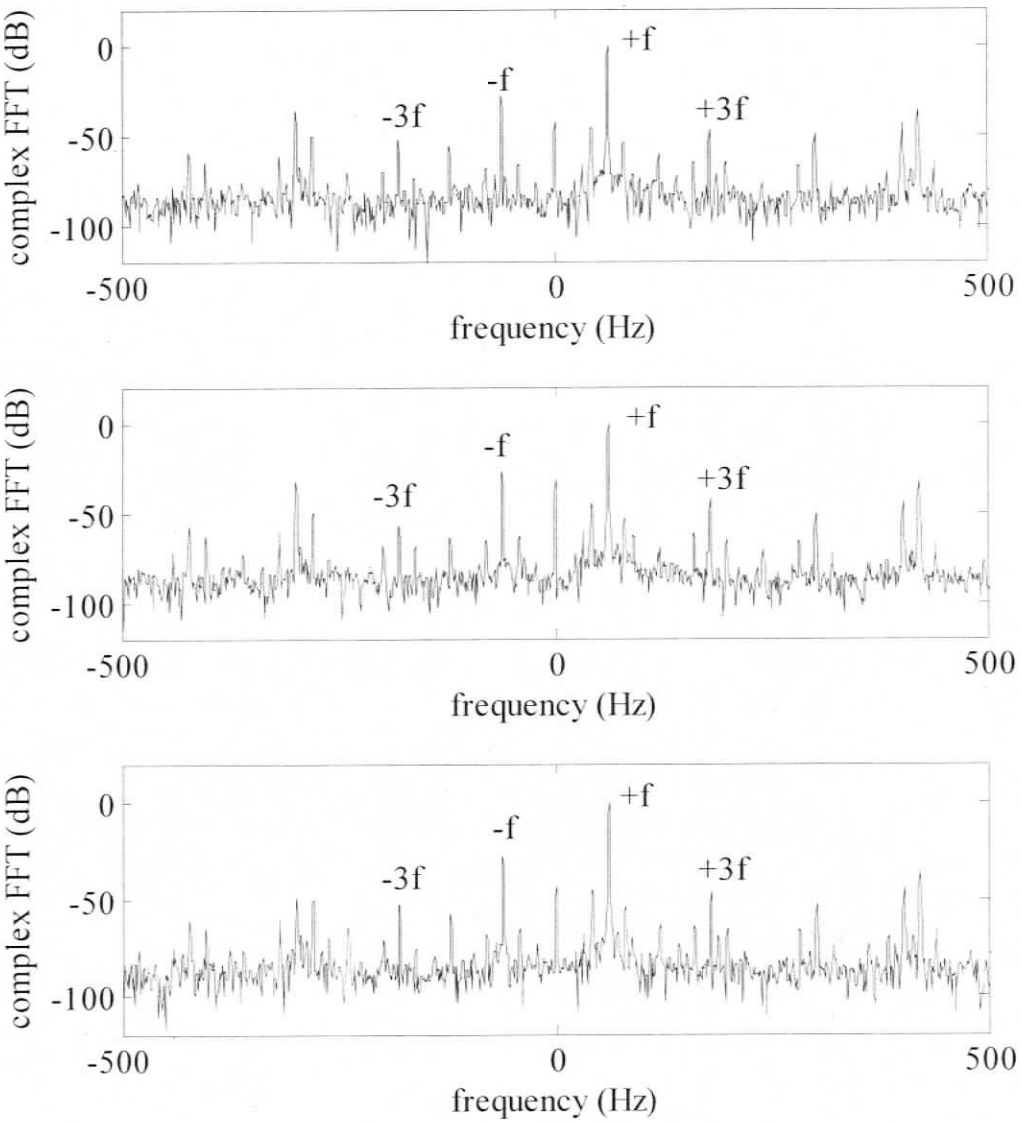

Fig 5.6 Experimentally computed line current spectra under full load condition: healthy machine with balanced supply (top); healthy machine with unbalanced supply (middle); single-turn fault machine with balanced supply (bottom).

As can be seen from Figs. 5.5 and 5.6, considerable line current ±3f signatures can be observed for both no load and full load conditions under all three operating conditions. Even the top plot in Fig 5.5 has them because of structural asymmetry. Thus they are in accordance with theoretical analysis and numerical simulation. Due to the different combinations of time and permeance harmonics in generating +3f and -3f components,

dissimilarity will be seen between measured +3f and -3f signatures when they are plotted with respect to various fault severities as suggested in simulation results. They are shown in Figs 5.7 and 5.8 under different load conditions. It is very clear that structural asymmetry and voltage unbalance can cause lots of ambiguity in fault detection.

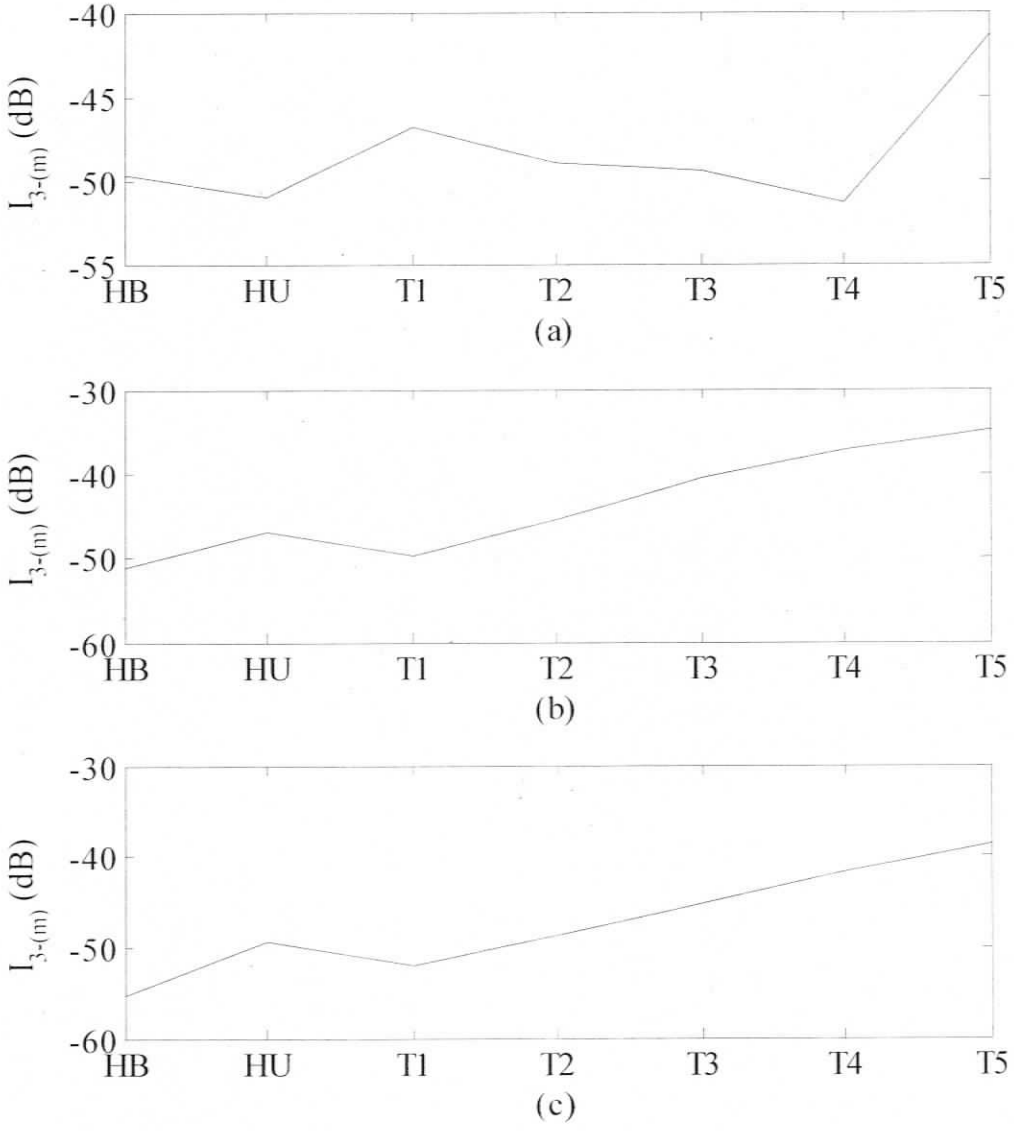

Fig. 5.7 Normalized, measured -3f fault signatures versus fault severities under different load conditions, from top to bottom: (a) 1799 rpm (no load); (b) 1780 rpm (half load); (c) 1770 rpm (full load).

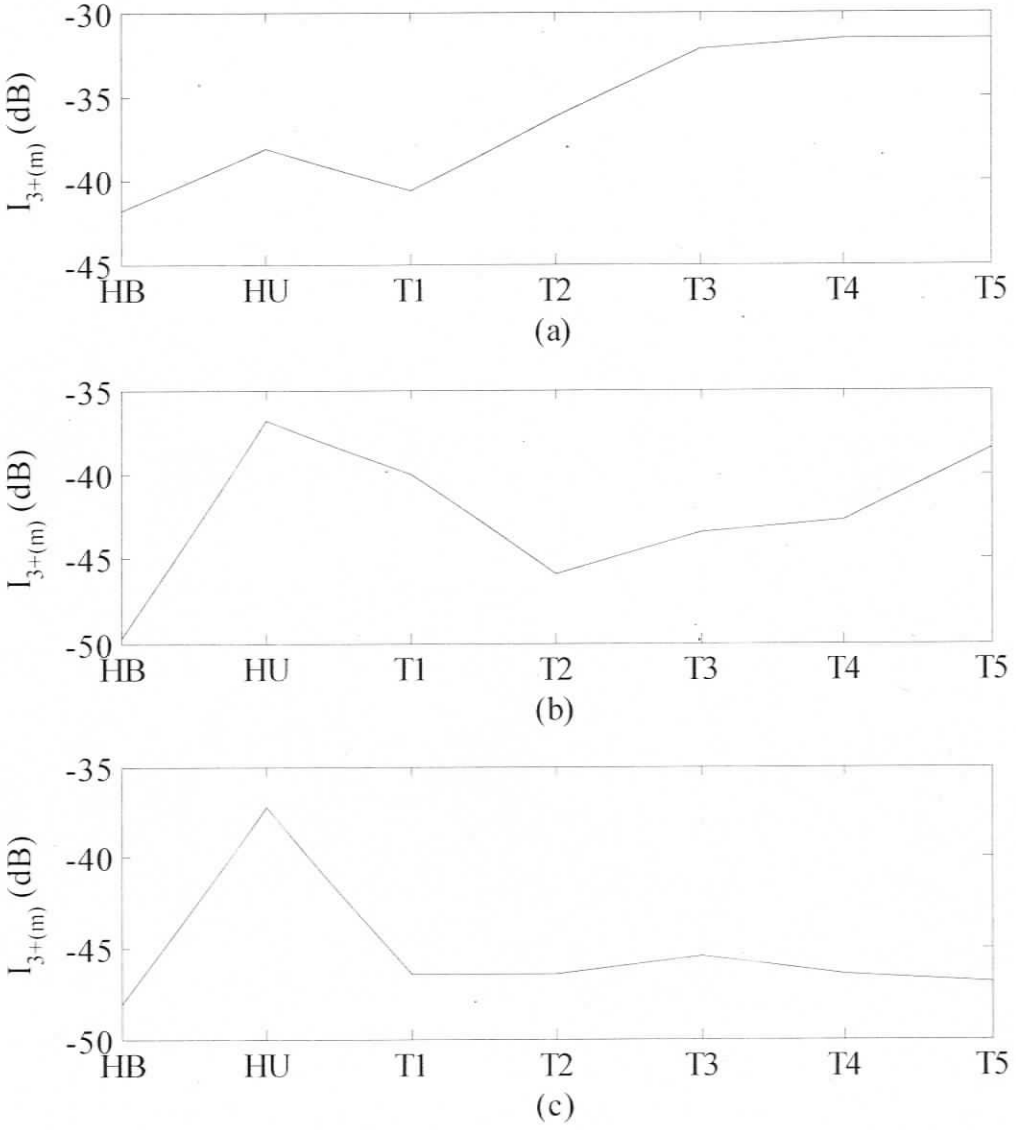

Fig. 5.8 Normalized, measured +3f fault signatures versus fault severities under different load conditions, from top to bottom: (a) 1799 rpm (no load); (b) 1780 rpm (half load); (c) 1770 rpm (full load).

Clearly +3f and -3f fault signatures are following different trends in detecting various fault severities and thus need different coefficients for residue elimination. It is also clear that voltage unbalance affects +3f components much more than -3f components.

5.4 Experimental, Residue-removed ±3f Signature

A signature can be deemed as an effective fault indicator only if it is distinguishable between faulty and other non-ideal operating conditions. Figs 5.7 and 5.8 imply that ±3f signatures will not be decisive fault indicators if residues arising out of non-idealities are not removed from measured quantities. In this section, the sensitivity of ±3f fault signatures are evaluated by subtracting residual ±3f component from initially measured ±3f signatures and plotted with respect to different fault conditions under various load levels. In doing this the same procedure as has been taken in the previous chapter is followed in the following analysis.

For the purpose of eliminating noise and uncertainty of fault signatures, average of several fault signatures computed under similar operating conditions were taken as the final fault signatures. With sampling frequency of 3600 Hz, 3600 samples can be obtained in one second. Complex FFT was conducted on every 600 samples. Hence six fault signatures will be obtained in one second data. The average value of the six fault signature was the final fault signature. This way, reliability of detection increased without compromising on the time of fault detection. Quick fault detection and isolation minimize the chances of fine hazards and explosions.

As for the incipient fault detecting purpose like single turn faults detection, the larger of the differences between 'T1' and 'HB' or 'HU', the clearer are the signatures in indicating single turn faults. In order to obtain the optimized fault signatures, during the course of residues estimation, the numbers of different supply unbalance conditions as well the number of complex coefficients have been optimized. In the fault signatures shown below, six harmonic components, i.e. ±f, ±5f, +7f and -11f (they were primarily selected based on the spectrum of line voltages and currents) associated complex coefficients trained by one balanced data set and eight unbalanced data sets under healthy conditions are used in determining ±3f residues. Hence totally six complex coefficients ($\bar{k}_{10-} - \bar{k}_{15-}$) or ($\bar{k}_{10+} - \bar{k}_{15+}$) are determined for residue estimation. Also, as stated in chapter 3, the other two sets of complex coefficients will be determined if line current

harmonics are replaced by line voltage harmonics which are given as ($\bar{k}_{U0-} - \bar{k}_{U5-}$) and ($\bar{k}_{U0+} - \bar{k}_{U5+}$). Therefore, totally four types of residues are estimated and their expressions are given by following respective equations.

$$\bar{I}_{U3+(e)} = \bar{k}_{U0+}\overline{U}_{1+} + \bar{k}_{U1+}\overline{U}_{1-} + \bar{k}_{U2+}\overline{U}_{5+} + \bar{k}_{U3+}\overline{U}_{5-} + \bar{k}_{U4+}\overline{U}_{7+} + \bar{k}_{U5+}\overline{U}_{11-} \tag{5.1}$$

$$\bar{I}_{I3+(e)} = \bar{k}_{I0+}\bar{I}_{1+} + \bar{k}_{I1+}\bar{I}_{1-} + \bar{k}_{I2+}\bar{I}_{5+} + \bar{k}_{I3+}\bar{I}_{5-} + \bar{k}_{I4+}\bar{I}_{7+} + \bar{k}_{I5+}\bar{I}_{11-} \tag{5.2}$$

$$\bar{I}_{U3-(e)} = \bar{k}_{U0-}\overline{U}_{1+} + \bar{k}_{U1-}\overline{U}_{1-} + \bar{k}_{U2-}\overline{U}_{5+} + \bar{k}_{U3-}\overline{U}_{5-} + \bar{k}_{U4-}\overline{U}_{7+} + \bar{k}_{U5-}\overline{U}_{11-} \tag{5.3}$$

$$\bar{I}_{I3-(e)} = \bar{k}_{I0-}\bar{I}_{1+} + \bar{k}_{I1-}\bar{I}_{1-} + \bar{k}_{I2-}\bar{I}_{5+} + \bar{k}_{I3-}\bar{I}_{5-} + \bar{k}_{I4-}\bar{I}_{7+} + \bar{k}_{I5-}\bar{I}_{11-} \tag{5.4}$$

According to above expressions, for each operating point, four fault signatures will be obtained:

$$\mathrm{FSI}_{U3+} = \left|\bar{I}_{3+(m)} - \bar{I}_{U3+(e)}\right| \tag{5.5}$$

$$\mathrm{FSI}_{U3-} = \left|\bar{I}_{3-(m)} - \bar{I}_{U3-(e)}\right| \tag{5.6}$$

$$\mathrm{FSI}_{I3+} = \left|\bar{I}_{3+(m)} - \bar{I}_{I3+(e)}\right| \tag{5.7}$$

$$\mathrm{FSI}_{I3-} = \left|\bar{I}_{3-(m)} - \bar{I}_{I3-(e)}\right| \tag{5.8}$$

These four types of fault signatures computed by using both balance and balanced data sets are plotted respectively in the Figs. 5.9 – 5.12 followed by the results under all five load levels listed in Tables 5.1 – 5.4. Also, the coefficients associating with four types of fault signatures are shown in Tables 5.5 – 5.8 for quick comparison. The details of eight different unbalanced supply voltages together with one balanced supply voltage under which complex coefficients have been computed are listed in Appendix E. Also in an attempt to show the necessity of including different supply unbalances into the residues estimation, fault signatures obtained under the cases where residues are estimated by using only nine balanced supply voltage data sets are also shown in Appendix E. It is very clear that when residues are estimated by balanced supply voltage

only, the resulting fault signatures cannot distinguish turn fault related ±3f signatures from supply unbalance related ±3f signatures.

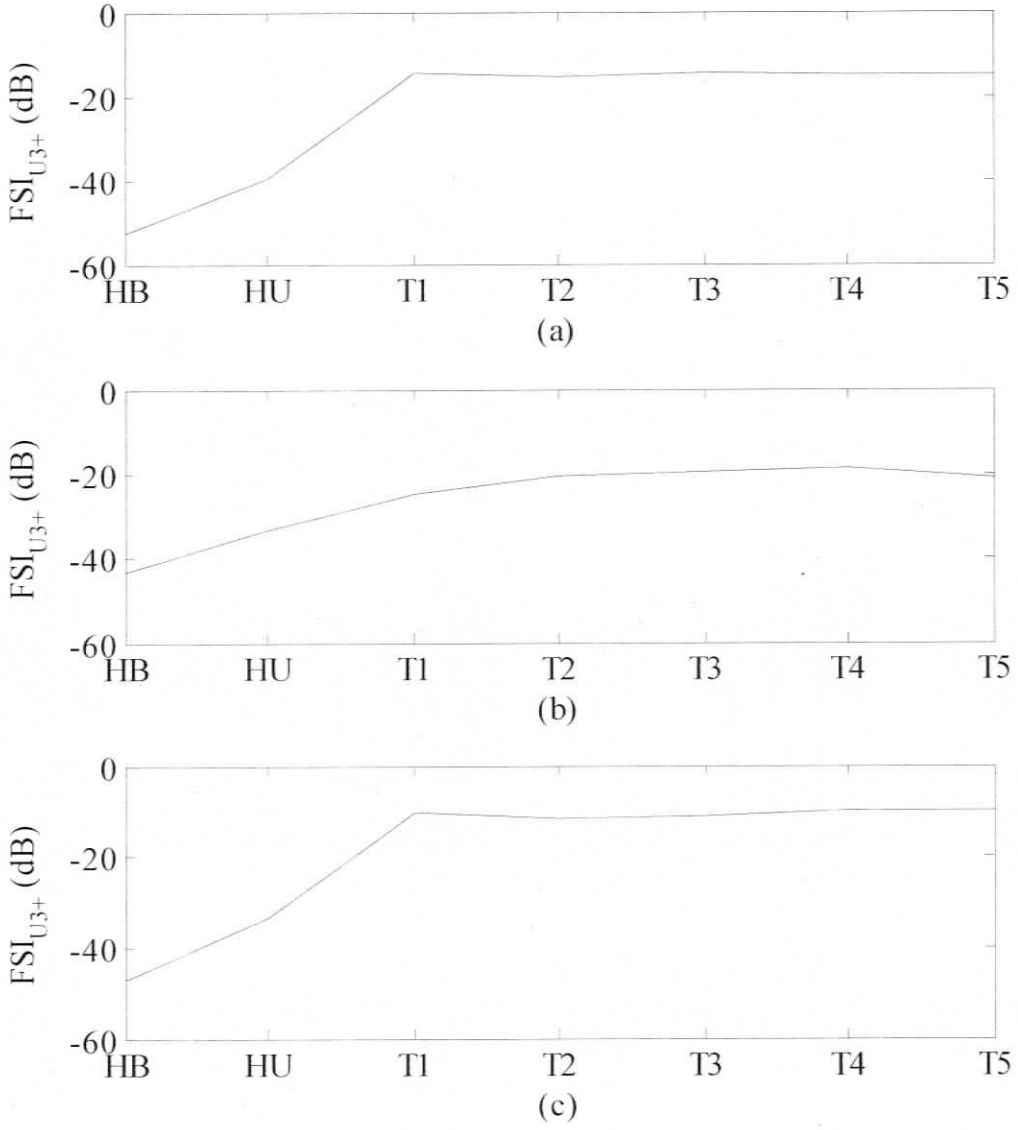

Fig. 5.9 Normalized, FSI_{U3+} versus fault severities under different load levels, from top to bottom: (a) 1799 rpm (no load); (b) 1780 rpm (half load); (c) 1760 rpm (full load).

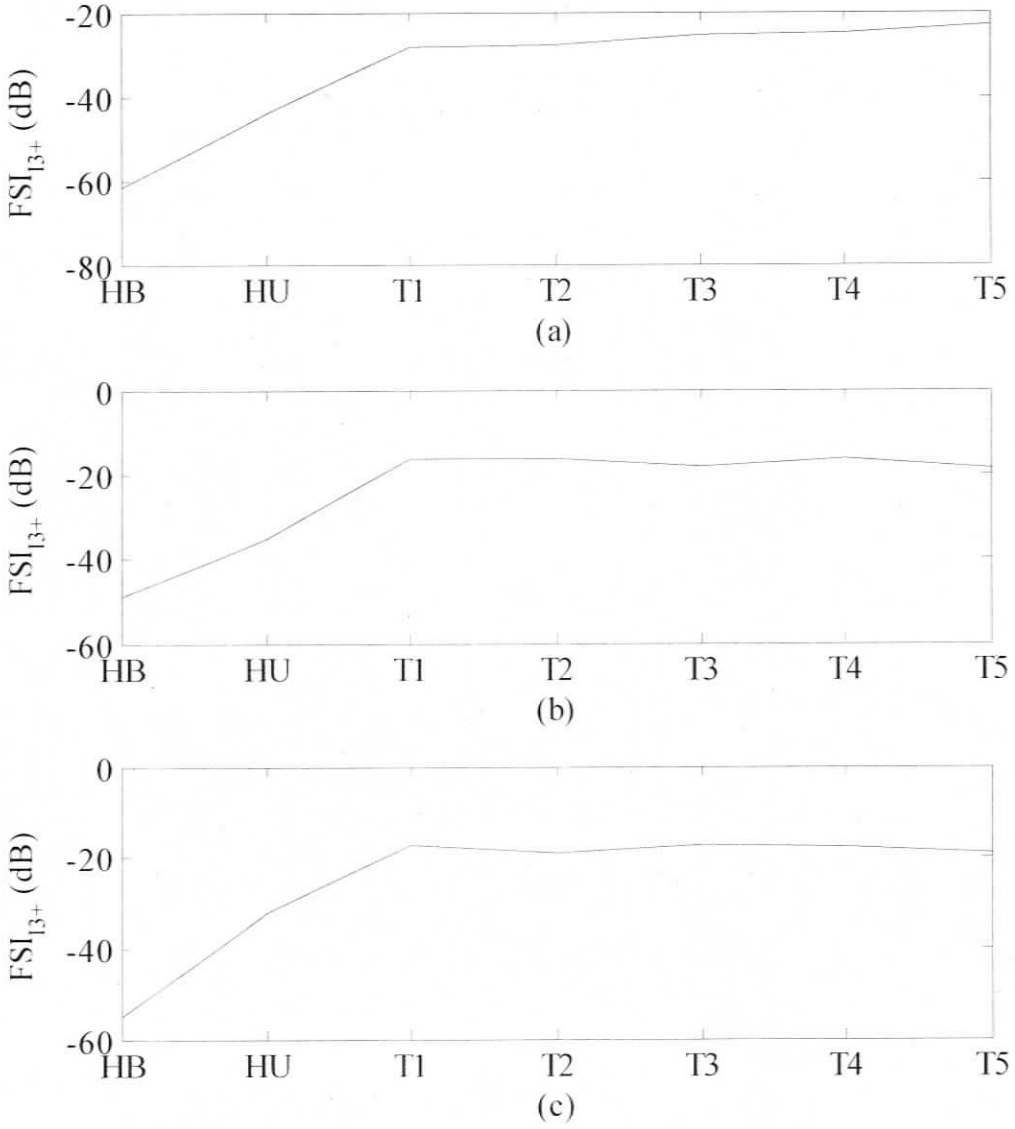

Fig. 5.10 Normalized, FSI_{I3+} versus fault severities under different load levels, from top to bottom: (a) 1799 rpm (no load); (b) 1780 rpm (half load); (c) 1760 rpm (full load).

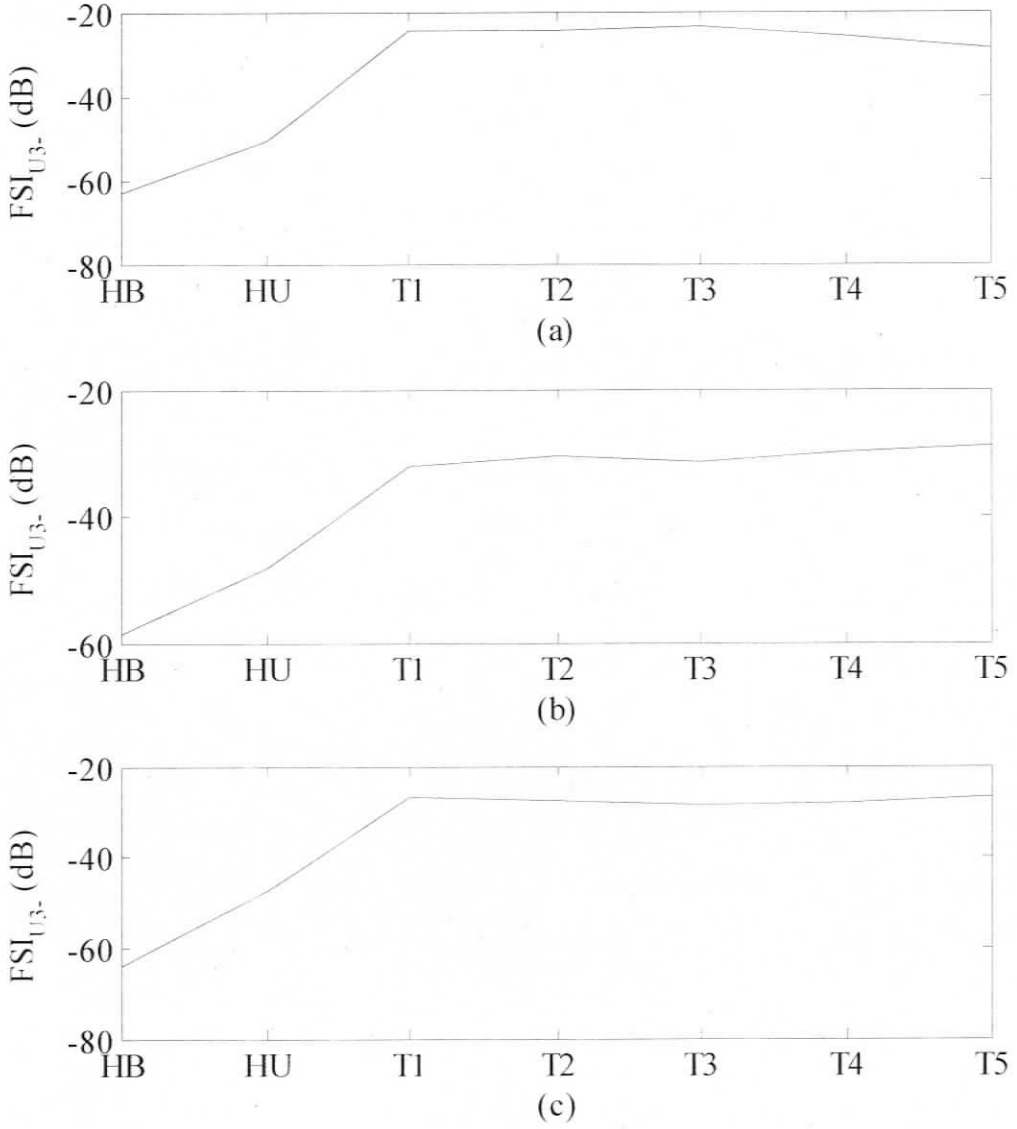

Fig. 5.11 Normalized, FSI_{U3-} versus fault severities under different load conditions, from top to bottom: (a) 1799 rpm (no load); (b) 1780 rpm (half load); (c) 1760 rpm (full load).

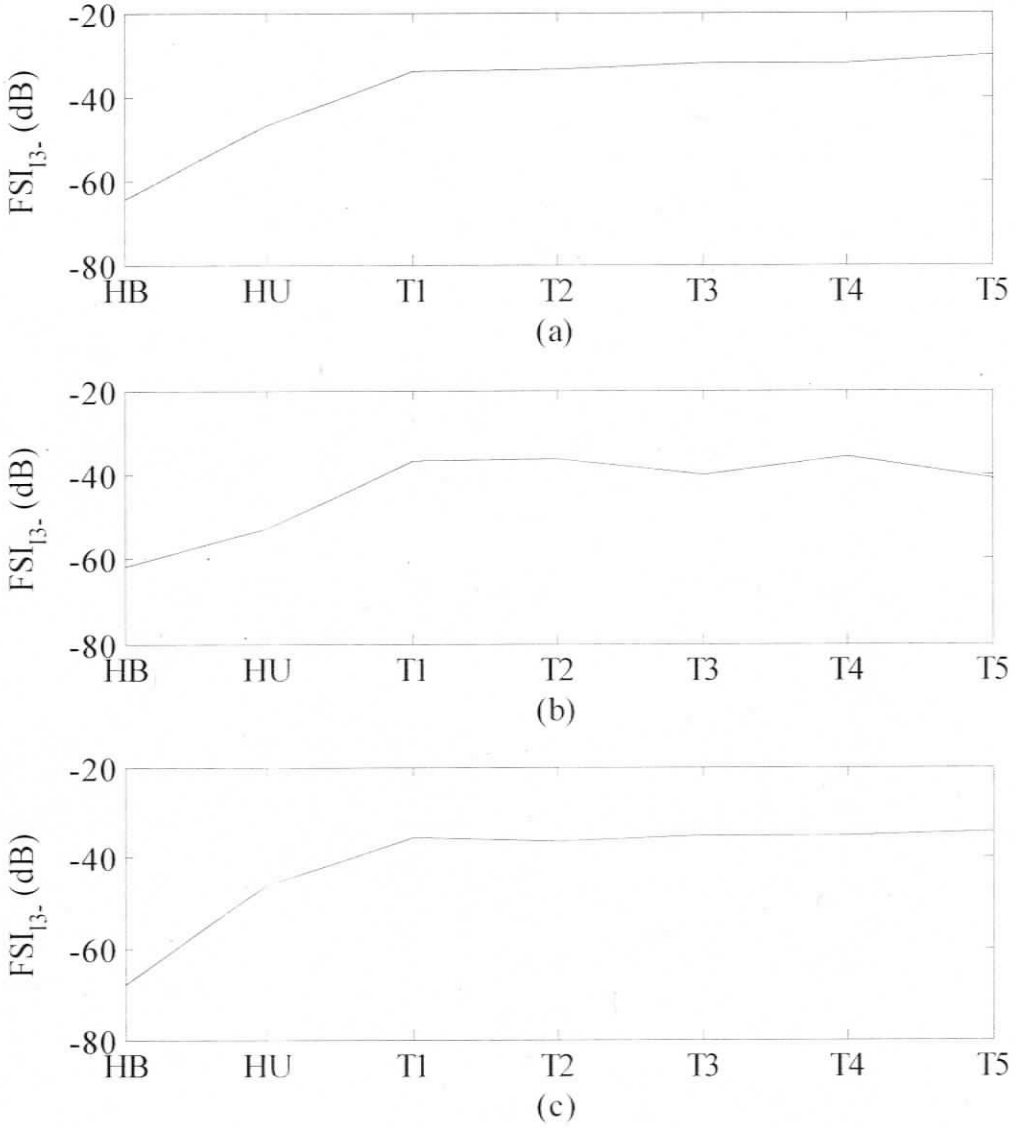

Fig. 5.12 Normalized, FSI_{I3-} versus fault severities under different load conditions, from top to bottom: (a) 1799 rpm (no load); (b) 1780 rpm (half load); (c) 1760 rpm (full load).

Table 5.1 FSI_{U3+} versus fault severities under different load conditions.

Rotating speed (rpm)	Normalized +3f signature (dB) under different operating conditions						
	HB	HU	T1	T2	T3	T4	T5
1799	-52.40	-39.99	-14.52	-15.32	-14.74	-14.94	-15.08
1790	-35.97	-24.20	-14.37	-12.16	-10.16	-10.65	-13.42
1780	-43.06	-33.45	-24.92	-20.36	-19.60	-18.84	-21.13
1770	-40.93	-28.09	-16.70	-19.35	-15.49	-13.63	-15.02
1760	-47.28	-33.71	-10.47	-11.58	-11.22	-10.04	-9.76

Table 5.2 FSI_{I3+} versus fault severities under different load conditions.

Rotating speed (rpm)	Normalized +3f signature (dB) under different operating conditions						
	HB	HU	T1	T2	T3	T4	T5
1799	-61.61	-44.28	-28.12	-28.08	-25.57	-25.23	-23.18
1790	-43.03	-29.07	-16.72	-18.22	-13.32	-12.20	-12.56
1780	-48.95	-35.30	-16.51	-16.46	-18.26	-16.45	-18.44
1770	-51.72	-33.13	-19.97	-18.36	-17.10	-17.35	-16.17
1760	-54.75	-32.15	-17.28	-19.13	-17.46	-17.60	-19.19

Table 5.3 FSI_{U3-} versus fault severities under different load conditions.

Rotating speed (rpm)	Normalized -3f signature (dB) under different operating conditions						
	HB	HU	T1	T2	T3	T4	T5
1799	-63.29	-50.48	-24.36	-24.57	-23.67	-25.84	-28.87
1790	-52.66	-49.47	-27.06	-27.74	-24.48	-23.88	-23.94
1780	-58.62	-48.15	-32.28	-30.71	-31.39	-29.91	-28.87
1770	-56.62	-45.30	-31.63	-33.22	-30.73	-28.87	-28.62
1760	-63.88	-47.18	-26.62	-27.57	-28.75	-27.93	-26.87

Table 5.4 FSI_{I3-} versus fault severities under different load conditions.

Rotating speed (rpm)	Normalized -3f signature (dB) under different operating conditions						
	HB	HU	T1	T2	T3	T4	T5
1799	-64.40	-47.14	-33.92	-33.50	-32.38	-32.26	-30.15
1790	-60.70	-54.42	-31.61	-31.87	-29.79	-26.00	-23.87
1780	-61.99	-52.82	-36.64	-36.22	-40.22	-35.73	-40.89
1770	-64.21	-52.83	-35.47	-32.38	-30.50	-30.23	-29.36
1760	-68.08	-45.99	-35.73	-36.51	-35.12	-35.04	-34.43

Table 5.5 $\bar{k}_{U0+}$ - $\bar{k}_{U5+}$ under different load conditions.

Rotating speed (rpm)	$\bar{k}_{U0+}$	$\bar{k}_{U1+}$	$\bar{k}_{U2+}$	$\bar{k}_{U3+}$	$\bar{k}_{U4+}$	$\bar{k}_{U5+}$
1799	-0.0004 - 0.0001j	-0.0015 - 0.0024j	-0.0059 - 0.0850j	-0.0243 - 0.0060j	-0.0156 - 0.0090j	-0.0050 + 0.0238j
1790	-0.0008 - 0.0018j	-0.0011 + 0.0076j	-0.0497 - 0.1728j	-0.1769 + 0.0324j	-0.0687 - 0.0079j	0.1710 + 0.0783j
1780	-0.0006 + 0.0004j	-0.0017 + 0.0066j	-0.1976 + 0.2522j	0.0060 + 0.0418j	-0.0195 - 0.0078j	0.0401 – 0.0208j
1770	-0.0010 - 0.0001j	-0.0086 + 0.0070j	-0.1113 + 0.1446j	-0.0323 + 0.0074j	-0.0021 - 0.0206j	0.0070 + 0.0234j
1760	-0.0036 + 0.0024j	-0.0006 + 0.0153j	-0.2650 - 0.1199j	-0.1168 + 0.1183j	-0.0918 - 0.1642j	0.0767 + 0.0927j

Table 5.6 $\bar{k}_{I0+}$ - $\bar{k}_{I5+}$ under different load conditions.

Rotating speed (rpm)	$\bar{k}_{I0+}$	$\bar{k}_{I1+}$	$\bar{k}_{I2+}$	$\bar{k}_{I3+}$	$\bar{k}_{I4+}$	$\bar{k}_{I5+}$
1799	0.0010 + 0.0008j	0.0011 + 0.0010j	-0.0452 + 0.0056j	-0.0726 - 0.0219j	-0.0001 + 0.0145j	0.0182 + 0.1598j
1790	-0.0075 - 0.0572j	0.0554 + 0.0852j	1.4983 - 1.2558j	-2.4222 + 5.9650j	3.5071 - 3.2895j	12.2125 - 10.8750j
1780	0.0045 - 0.0007j	-0.0001 - 0.0056j	0.0283 + 0.1661j	-0.1230 - 0.0125j	-0.0600 + 0.0520j	0.0849 + 0.1375j
1770	-0.0003 - 0.0018j	-0.0015 - 0.0041j	0.1364 + 0.0994j	-0.0501 + 0.0683j	0.0181 + 0.0362j	0.1218 + 0.0261j
1760	-0.0018 - 0.0030j	0.0006 - 0.0036j	0.0154 + 0.1733j	-0.0731 + 0.1306j	0.0429 + 0.0359j	0.1565 + 0.0006j

Table 5.7 $\bar{k}_{U0-}$ - $\bar{k}_{U5-}$ under different load conditions.

Rotating speed (rpm)	$\bar{k}_{U0-}$	$\bar{k}_{U1-}$	$\bar{k}_{U2-}$	$\bar{k}_{U3-}$	$\bar{k}_{U4-}$	$\bar{k}_{U5-}$
1799	-0.0001 - 0.0001j	-0.0017 - 0.0001j	-0.0204 + 0.0151j	-0.0056 + 0.0025j	0.0064 + 0.0025j	0.0049 + 0.0029j
1790	-0.0004 - 0.0001j	-0.0007 + 0.0007j	-0.0264 + 0.0101j	-0.0035 + 0.0233j	0.0092 + 0.0137j	0.0130 - 0.0189j
1780	0.0000 - 0.0002j	0.0002 - 0.0011j	-0.0011 - 0.0197j	-0.0061 - 0.0053j	0.0031 + 0.0020j	-0.0020 + 0.0073j
1770	0.0003 - 0.0002j	-0.0004 - 0.0033j	-0.0032 - 0.0656j	0.0046 - 0.0104j	0.0098 + 0.0048j	-0.0071 - 0.0031j
1760	0.0004 - 0.0006j	-0.0012 - 0.0020j	0.0065 - 0.0360j	0.0088 - 0.0258j	0.0234 + 0.0143j	-0.0184 - 0.0089j

Table 5.8 $\bar{k}_{I0-}$ - $\bar{k}_{I5-}$ under different load conditions.

Rotating speed (rpm)	$\bar{k}_{I0-}$	$\bar{k}_{I1-}$	$\bar{k}_{I2-}$	$\bar{k}_{I3-}$	$\bar{k}_{I4-}$	$\bar{k}_{I5-}$
1799	0.0341 - 0.0151j	-0.0354 + 0.0443j	-0.7526 + 0.2529j	-0.4692 + 0.8324j	-0.2727 + 1.0953j	1.2218 - 0.5340j
1790	-0.0333 - 0.0101j	0.0006 + 0.0372j	-0.3831 - 0.3392j	0.9872 - 0.4123j	0.0103 + 0.1187j	-1.9172 + 0.0476j
1780	-0.0253 + 0.0088j	0.0402 + 0.0241j	-1.2667 - 0.8559j	0.7529 - 0.1551j	0.3390 - 0.3839j	-0.9770 - 0.8292j
1770	0.0283 + 0.0117j	0.0053 - 0.0029j	-0.7863 + 0.2913j	-0.4570 - 1.0724j	-0.4746 + 0.1342j	-0.9867 + 1.0251j
1760	0.0236 + 0.0195j	-0.0203 - 0.0256j	0.3856 - 0.1434j	0.1467 - 1.3099j	-0.4327 - 0.0093j	-1.2398 + 0.5962j

5.5 Evaluation of Experimental Results

Figures and tables shown in the proceeding section displayed ±3f fault signatures under different operating points. All the four types of fault signatures FSI_{U3+}, FSI_{I3+}, FSI_{U3-} and FSI_{I3-} can effectively discriminate 'T1' from 'HB' as well as 'HU'. That is, fault signatures obtained above can effectively indicate single turn faults. In Table 5.6 – 5.8, the differences among four types of complex coefficients clearly can be seen. Hence conclusions of Chapter 3 and simulation results obtained in chapter 4 have been verified.

In order to show the detectability of the fault signatures in detecting single turn faults under various conditions, differences between 'HU' and 'T1' given in Tables 5.1 – 5.4 are calculated and summarized in Table 5.9.

Table 5.9 Comparisons of differences between 'HU' and 'T1' with respect to different type of residues.

Rotating speed (rpm)	Differences between 'HU' and 'T1' (dB)			
	FSI_{U3+}	FSI_{I3+}	FSI_{U3-}	FSI_{I3-}
1799	25.47	16.16	26.12	13.22
1790	9.83	12.35	22.41	22.81
1780	8.53	18.79	15.87	16.18
1770	11.39	13.16	13.67	17.36
1760	23.24	14.87	20.56	10.26

As can be seen from Table 5.9, sensitivities of FSI_{U3+}, FSI_{I3+}, FSI_{U3-} and FSI_{I3-} are varied with respect to different load conditions. Besides, for each load level, the sensitivities are changing significantly among the four types of fault signatures. This can be attributed to the variations of permeance and time harmonics from which fault signatures were derived. But, in practical applications, all the values shown in Table 5.9 are sufficient enough to distinguish inter-turn faults from other abnormal conditions of the machine. Therefore, all the computed four fault signatures can be deemed as reliable fault indictors for line-fed star-connected induction machine.

Chapter 6

Experimental Results with Three Phase Inverter-fed, Star-connected Induction Machine

6.1 Introduction of Inverter-fed Induction Machine Setup

After adding a three phase uncontrolled rectifier followed by an inverter between isolation transformer and motor in line-fed star-connected machine setup, the versatility of proposed fault detection scheme can be validated for solid state induction motor drive also. The block diagram of the experimental setup is shown in Fig. 6.1.

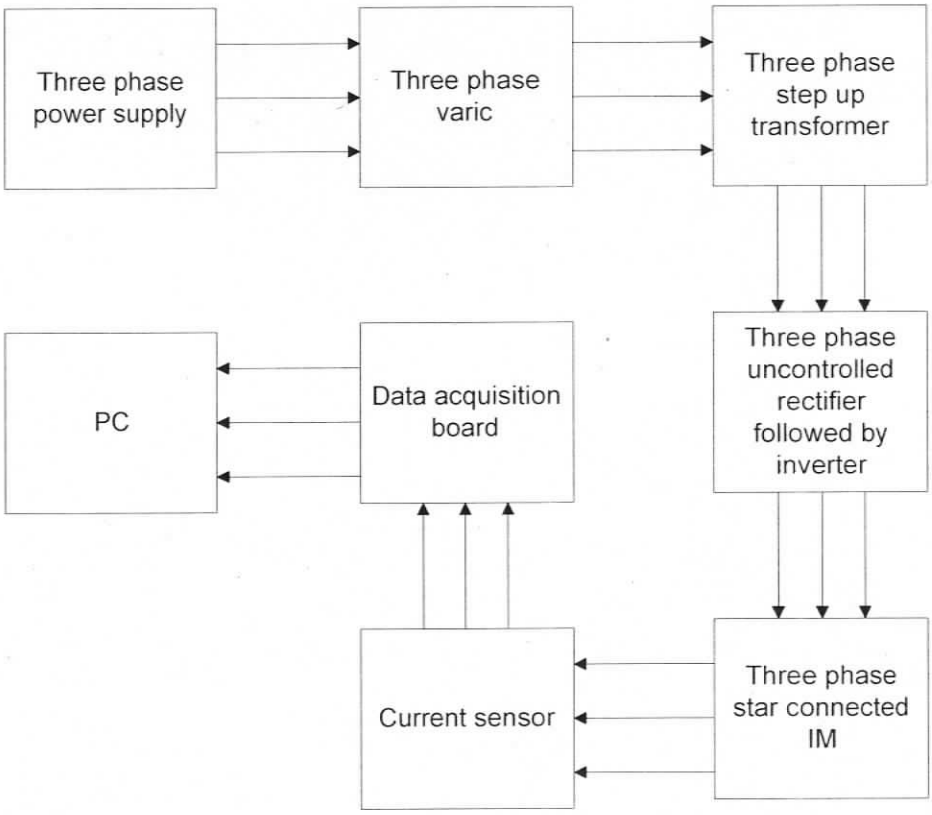

Fig. 6.1 Experimental setup for the inverter-fed star-connected induction machine.

6.2 Experimental Results for Operating Frequency of 60 Hz

Using experimental setup described above, the line current time and frequency domain signatures obtained under 60 Hz supply frequency are displayed in Fig. 6.2.

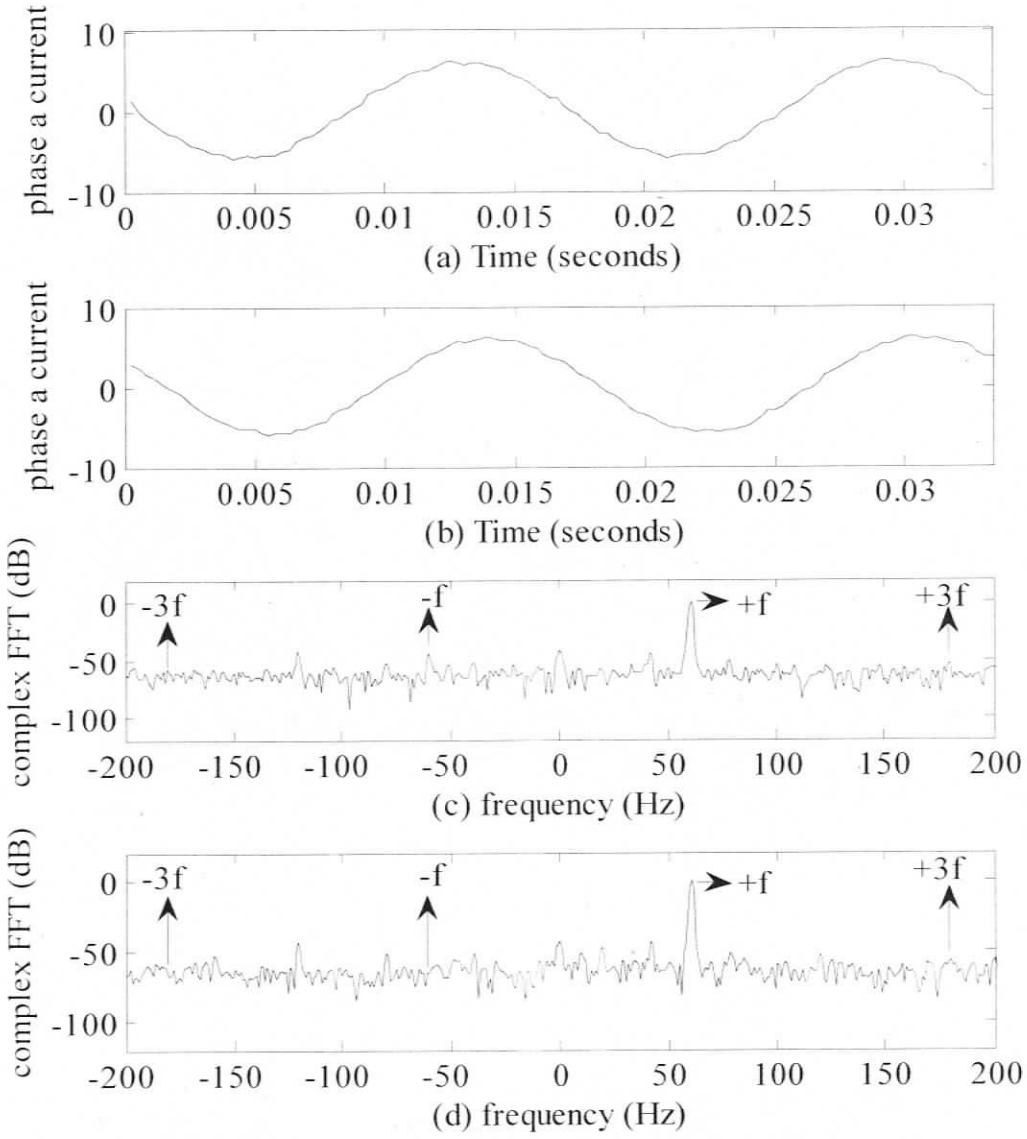

Fig 6.2 Full load, (a) two cycles of healthy phase 'a' current; (b) two cycles of single turn fault phase 'A' current; (c) complex FFT of healthy machine; (d) complex FFT of single turn fault machine; plots obtained under 60 Hz of inverter output frequency and at the speed of 1760 rpm.

6.2.1 Measured ±3f Signatures

Initially, measured ±3f signatures are plotted with respect to the varying fault severities. The results are as shown in Figs 6.3 and 6.4.

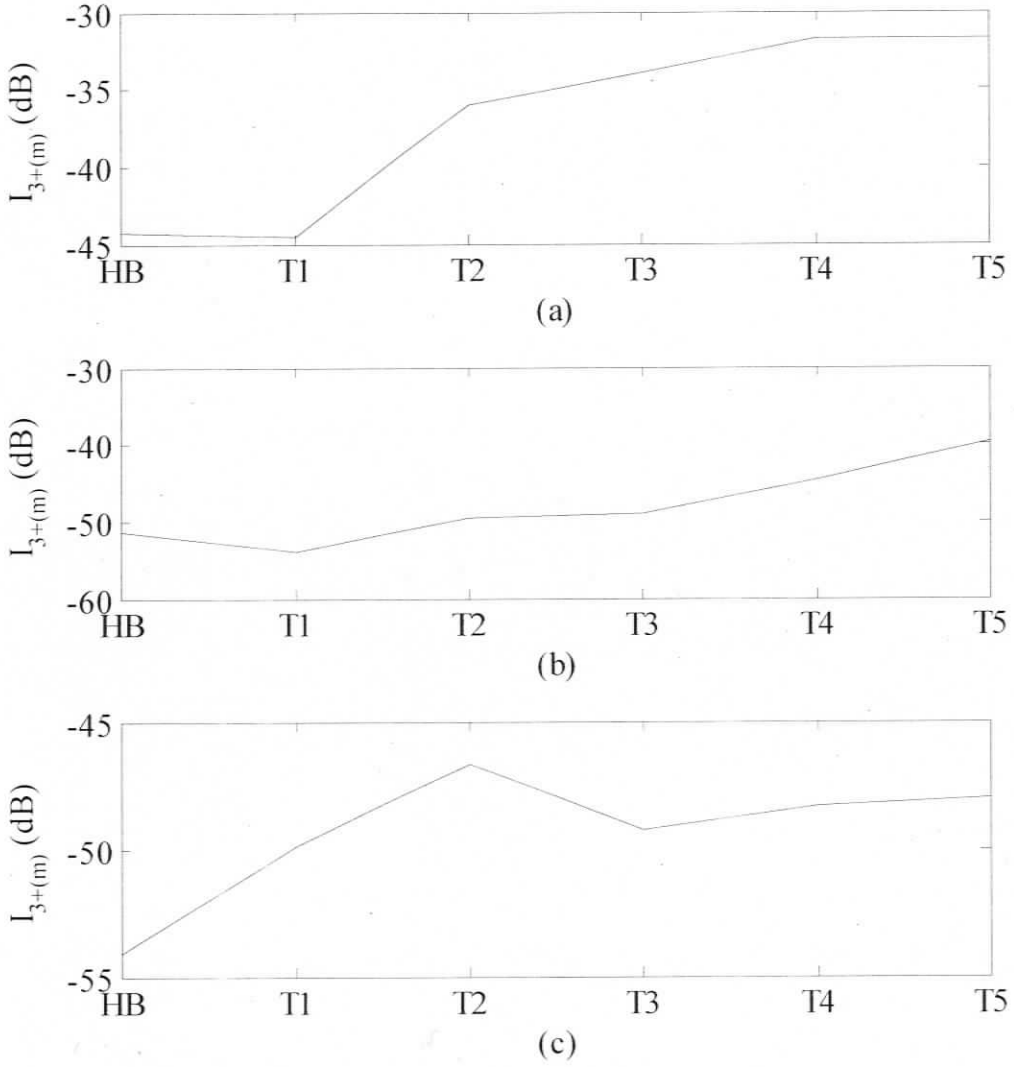

Fig 6.3 Normalized, measured +3f fault signatures versus fault severities under different load levels, from top to bottom: (a) 1799 rpm (no load); (b) 1780 rpm (half load); (c) 1760 rpm (full load).

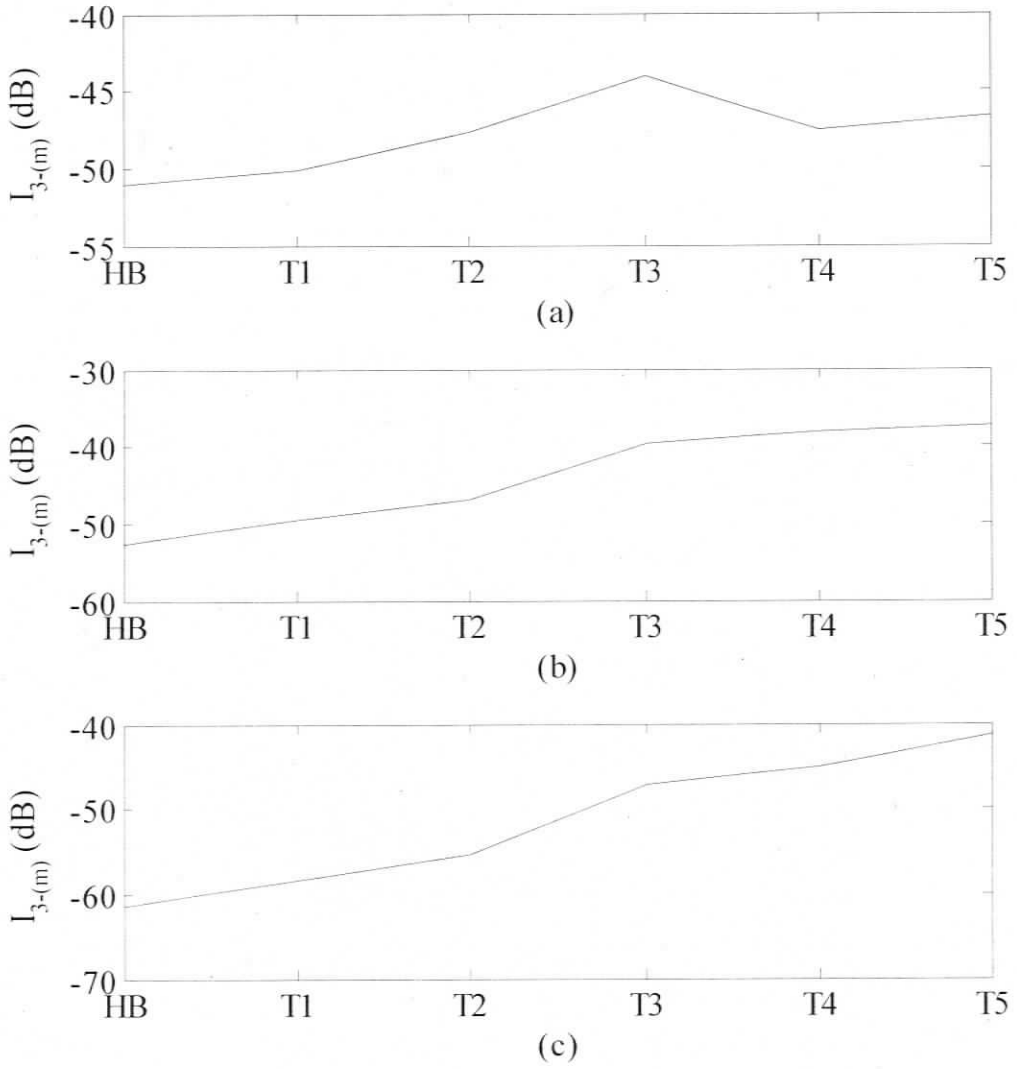

Fig 6.4 Normalized, measured -3f fault signatures versus fault severities under different load levels (a) 1799 rpm (no load); (b) 1780 rpm (half load); (c) 1760 rpm (full load).

In this experiment, 'HU' is not included as it unlikely that voltage drops in switches and diodes will produce any significant unbalance. This can be easily realized when Fig. 6.2 (c) is compared with Fig. 5.6 (middle plot)). Again, the effects of inherent structural asymmetry make current spectra and ±3f signatures very random which makes conclusive inter-turn fault indicator impossible to achieve. Therefore, residues are

estimated and subtracted from measured ±3f signatures. Procedure similar to that has been carried out in chapter 5 has been followed.

6.2.2 Experimental ±3f Fault Signatures

Since sampling terminal voltages of an inverter driven induction motor necessitates the use of a high frequency voltage probe and fast DAQ, only current based detection technique is used. Resulting fault signatures are shown in Figs. 6.5, 6.6 respectively.

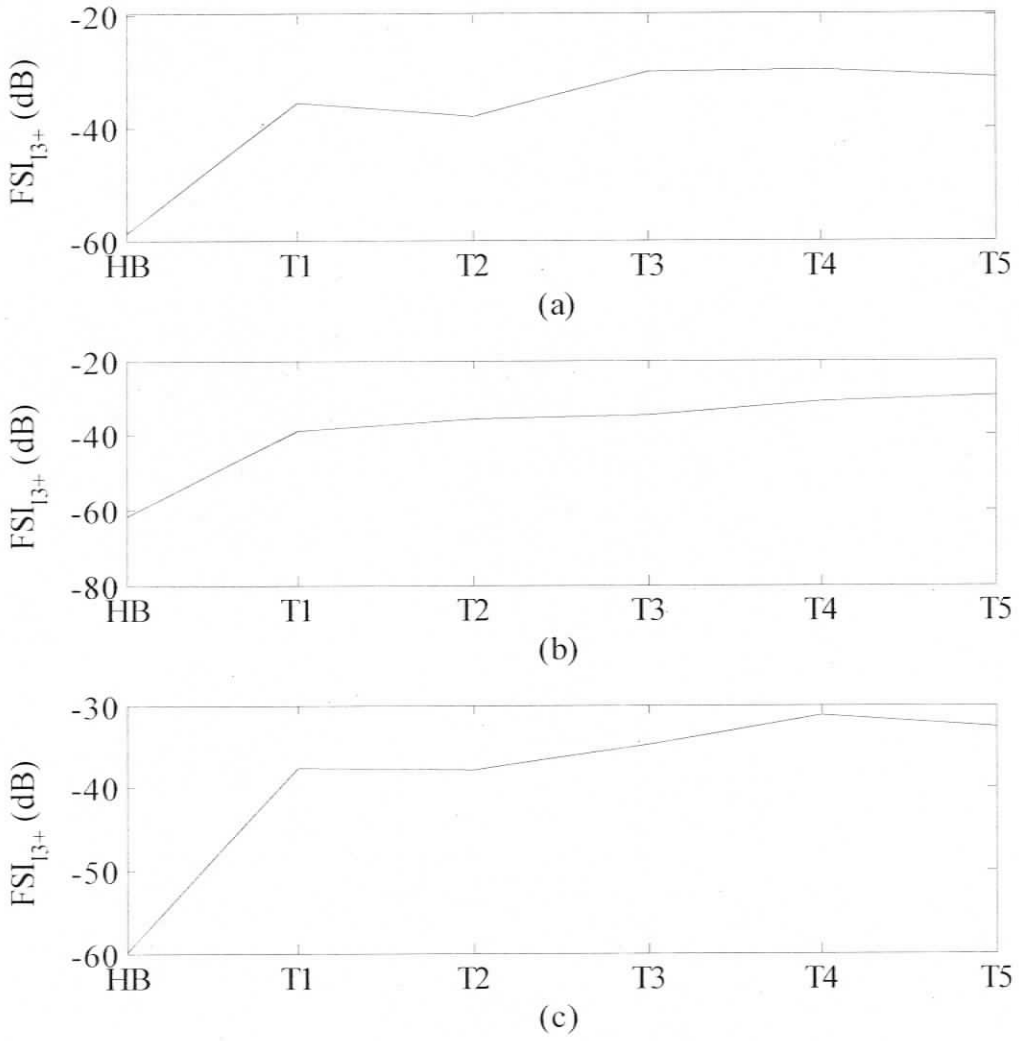

Fig 6.5 FSI_{I3+} versus fault severities under different load levels, from top to bottom: (a) 1799 rpm (no load); (b) 1780 rpm (half load); (c) 1760 rpm (full load).

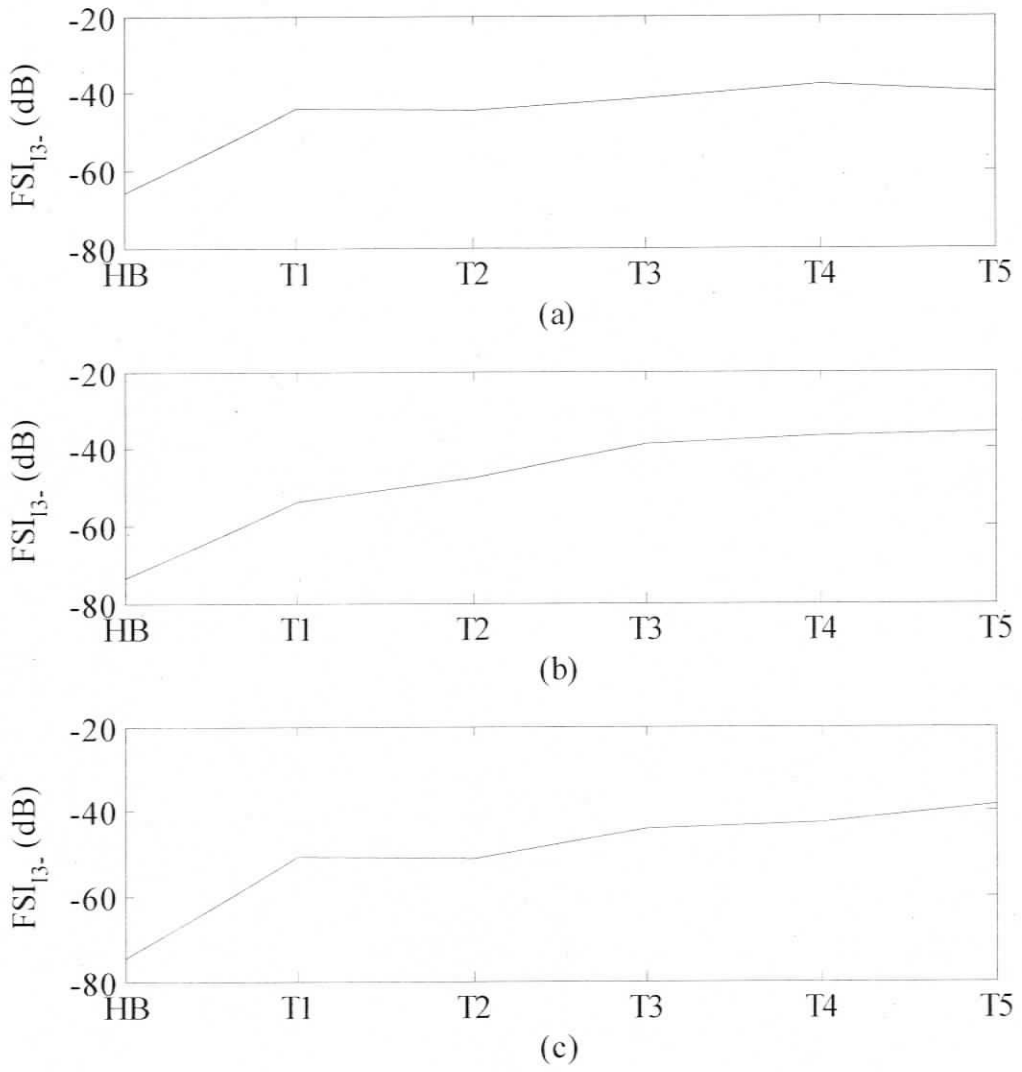

Fig 6.6 FSI_{I3-} versus fault severities under different load levels, from top to bottom: (a) 1799 rpm (no load); (b) 1780 rpm (half load); (c) 1760 rpm (full load).

The feasibility of using current probe directly can be explained that the line currents are sufficiently filtered by the machine inductances and their acquisitions only require instruments that can be used for utility driven motors. Residues are estimated by four complex coefficients ($\bar{k}_{I0+}$ - $\bar{k}_{I3+}$) or ($\bar{k}_{I0-}$ - $\bar{k}_{I3-}$) which are computed from six data sets, i.e., they are computed using (3.36) and (3.37) respectively. Again, fault signatures obtained under all five testing load levels are given in Tables 6.1, 6.2.

Table 6.1 FSI_{I3+} versus fault severities under different load conditions.

Rotating speed (rpm)	Normalized +3f signature (dB) under different operating points					
	HB	T1	T2	T3	T4	T5
1799	-58.73	-35.63	-37.95	-30.09	-29.98	-31.19
1790	-53.66	-38.39	-33.02	-29.19	-25.85	-26.36
1780	-61.54	-38.72	-36.03	-34.83	-30.94	-29.73
1770	-63.71	-46.69	-41.09	-45.85	-35.41	-32.68
1760	-59.87	-37.65	-37.83	-34.73	-31.28	-32.78

Table 6.2 FSI_{I3-} versus fault severities under different load conditions.

Rotating speed (rpm)	Normalized -3f signature (dB) under different operating points					
	HB	T1	T2	T3	T4	T5
1799	-65.88	-43.88	-44.48	-41.25	-37.86	-39.69
1790	-65.89	-49.37	-43.82	-36.85	-35.58	-32.57
1780	-73.67	-54.02	-47.51	-39.06	-37.06	-35.73
1770	-76.00	-50.50	-48.07	-47.70	-41.52	-37.63
1760	-74.52	-50.73	-51.34	-44.36	-42.65	-38.67

Complex coefficients obtained accordingly are listed in Tables 6.3 and 6.4 respectively.

Table 6.3 $\bar{k}_{I0+}$ - $\bar{k}_{I3+}$ under different load conditions.

Rotating speed (rpm)	$\bar{k}_{I0+}$	$\bar{k}_{I1+}$	$\bar{k}_{I2+}$	$\bar{k}_{I3+}$
1799	-0.0087 + 0.0099j	0.0123 – 0.0669j	1.3468 – 1.7855j	0.2389 + 0.7489j
1790	0.0027 + 0.0131j	-0.1342 – 0.0423j	-3.9922 + 2.0195j	-0.9581 + 0.1191j
1780	-0.0068 + 0.0145j	0.1275 + 0.0125j	-1.3928 – 2.4727j	0.4540 – 0.9994j
1770	-0.0004 + 0.0028j	0.0874 + 0.0526j	-1.4343 – 5.4780j	0.4343 + 0.4640j
1760	0.0249 – 0.0158j	0.0165 + 0.2094j	-1.3448 – 2.9150j	1.3438 + 2.7802j

Table 6.4 $\bar{k}_{I0-}$ - $\bar{k}_{I3-}$ under different load conditions.

Rotating speed (rpm)	$\bar{k}_{I0-}$	$\bar{k}_{I1-}$	$\bar{k}_{I2-}$	$\bar{k}_{I3-}$
1799	0.0001 + 0.0025j	0.0048 – 0.0415j	0.1194 – 0.2859j	-0.0823 + 0.0261j
1790	-0.0001 – 0.0016j	0.1074 – 0.0474j	-0.5322 – 0.9230j	0.2376 + 0.1592j
1780	0.0006 – 0.0010j	0.0249 – 0.0146j	-0.0534 – 0.1208j	0.0541 + 0.0625j
1770	0.0019 + 0.0000j	0.0183 – 0.0158j	0.3091 + 0.0296j	0.0194 + 0.0519j
1760	0.0019 + 0.0011j	0.0071 – 0.0264j	-0.1378 – 0.2188j	-0.1613 + 0.2321j

From Figs. 6.3 and 6.4 as well as Tables 6.1 and 6.2 one can clearly observe that FSI_{I3+} and FSI_{I3-} can decisively indicate single turn fault. In addition, different coefficients are corresponding with FSI_{I3+} and FSI_{I3-} under different load levels as shown in Tables 6.3 and 6.4.

6.3 Experimental Results under Operating Frequencies of 30 Hz and 10 Hz

As the speed variation of the induction motor driven by an inverter are realized by adjusting the operating frequency. Hence, fault detection under different frequencies of solid state induction motor drive becomes necessary. In the following experiments, fault tests are conducted based on induction motor driven by the inverter operating under the frequencies of 30 Hz and 10 Hz. For each frequency, fault signatures are computed under two different load levels respectively.

6.3.1 Experimental Results under Frequency of 30 Hz

Figs. 6.7 – 6.9 as well as Tables 6.5 and 6.6 show the experimental results obtained under operating frequency of 30 Hz.

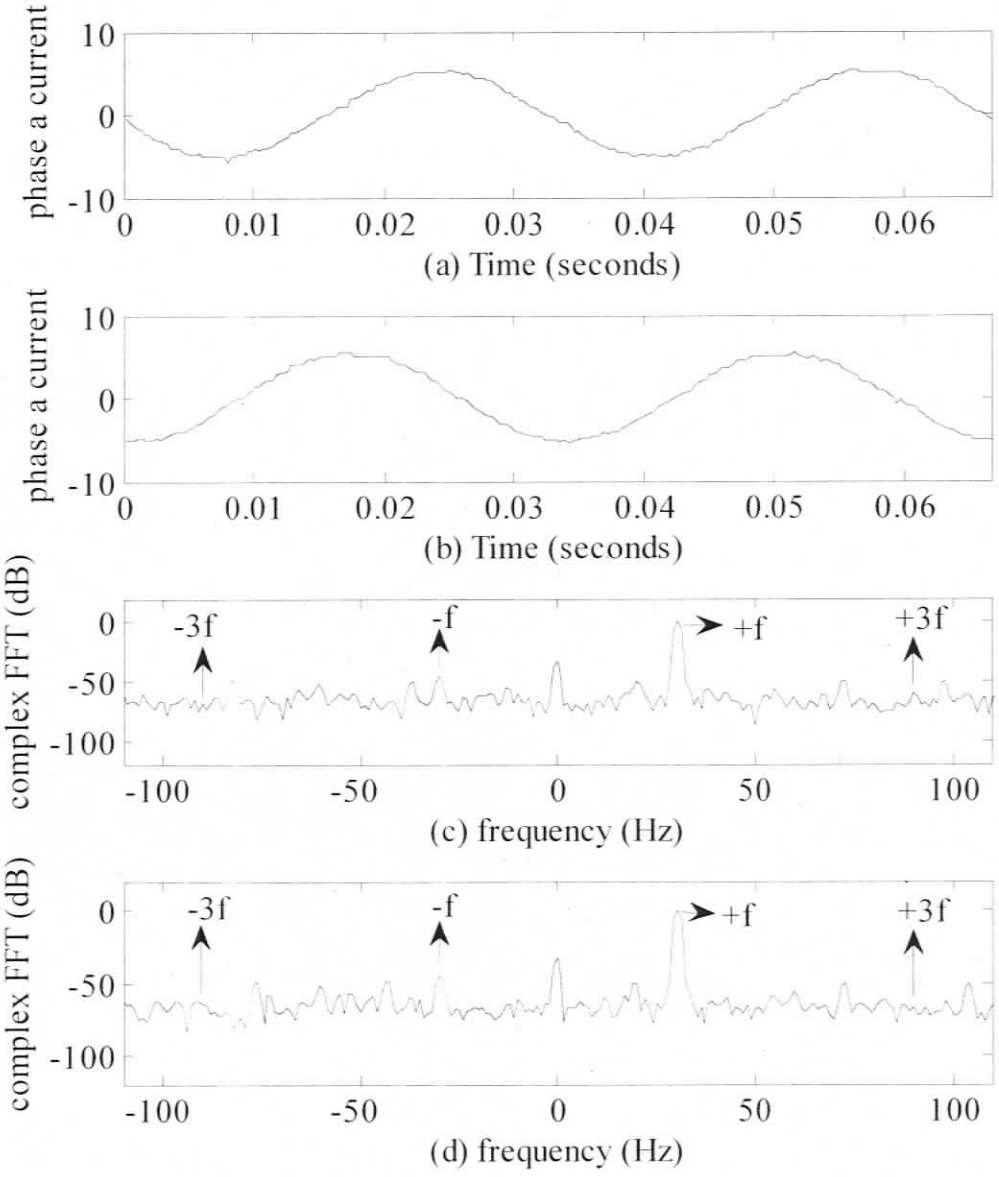

Fig 6.7 (a) two cycles of healthy phase 'a' current; (b) two cycles of single turn fault phase 'a' current; (c) complex FFT of healthy machine; (d) complex FFT of single turn fault machine; plots obtained under frequency of 30 Hz with rotating speed of 874 rpm.

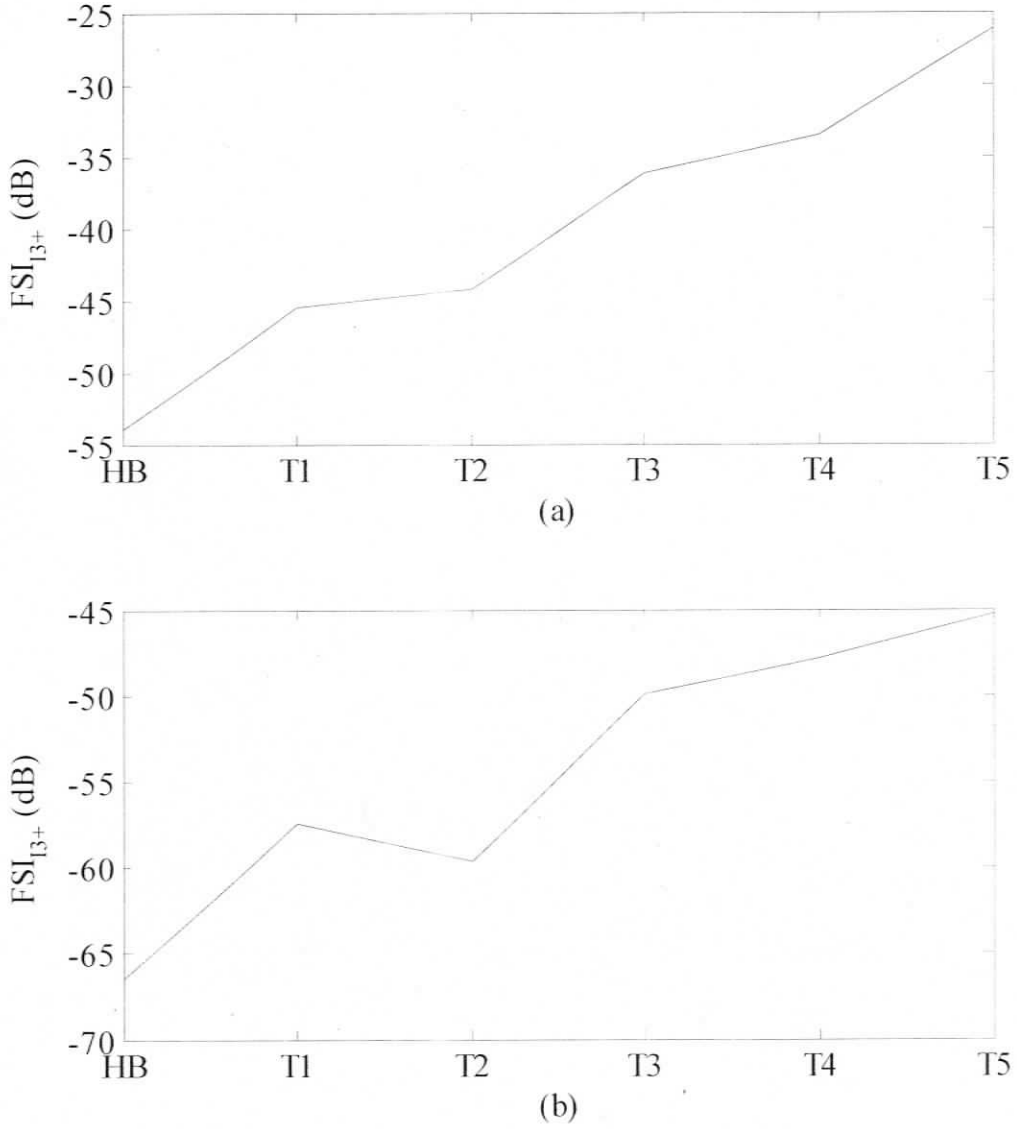

Fig 6.8 FSI_{I3+} versus fault severities under frequency of 30 Hz: (a) at speed of 898 rpm; (b) at speed of 874 rpm.

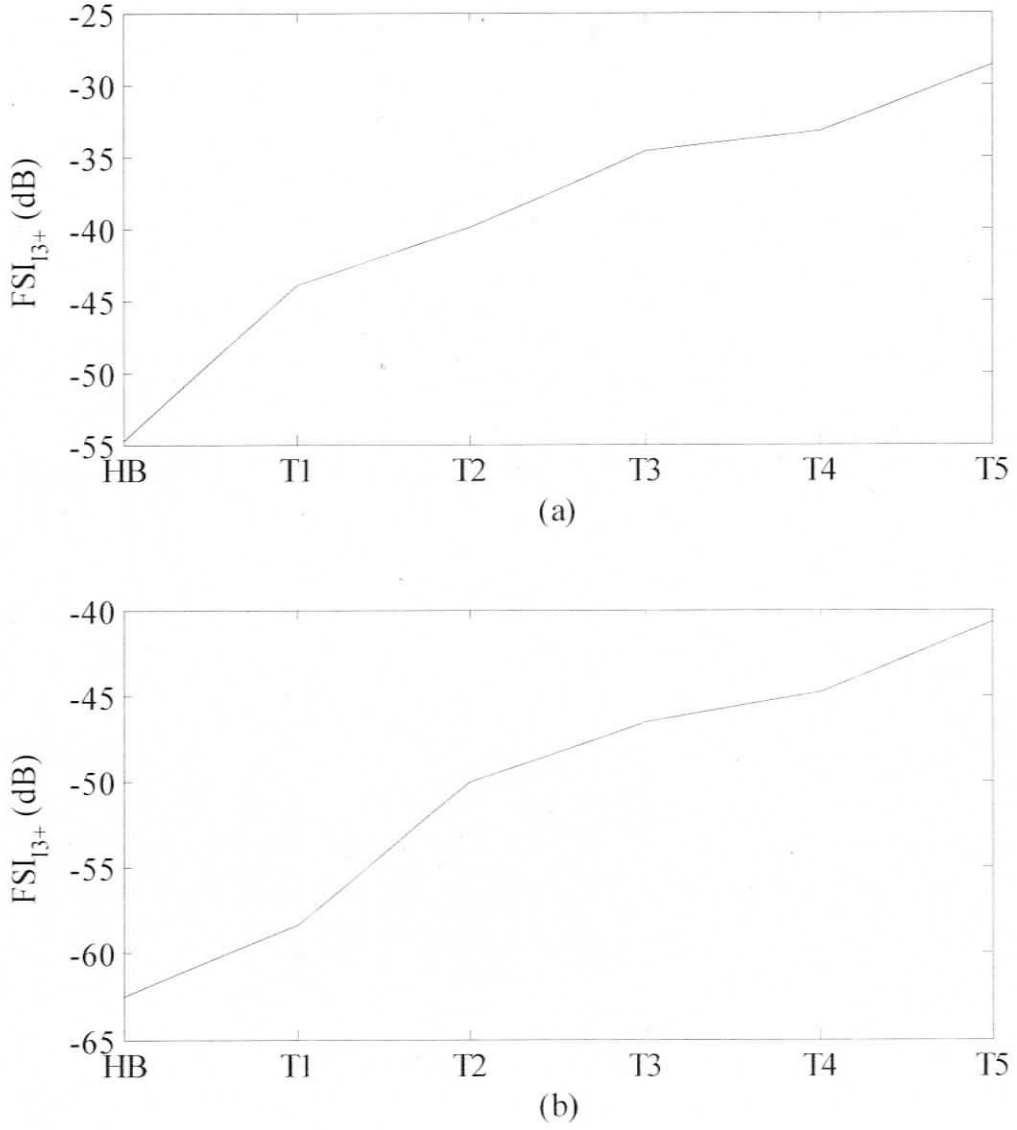

Fig 6.9 FSI_{I3-} versus fault severities under frequency of 30 Hz: (a) at speed of 898 rpm; (b) at speed of 874 rpm.

Table 6.5 FSI_{I3+} versus fault severities under frequency of 30 Hz.

Rotating speed (rpm)	Normalized +3f signature (dB) under different operating points					
	HB	T1	T2	T3	T4	T5
898	-53.95	-45.52	-44.17	-36.21	-33.59	-26.15
874	-66.46	-57.43	-59.59	-49.93	-47.88	-45.26

Table 6.6 FSI_{I3-} versus fault severities under frequency of 30 Hz.

Rotating speed (rpm)	Normalized -3f signature (dB) under different operating points					
	HB	T1	T2	T3	T4	T5
898	-54.76	-43.92	-39.94	-34.67	-33.31	-28.72
874	-62.47	-58.37	-50.05	-46.48	-44.85	-40.73

6.3.2 Experimental Results under Frequency 10 Hz

In Figs. 6.10 – 6.12 as well as Tables 6.7 and 6.8, experimental results obtained under operating frequency of 10 Hz are displayed.

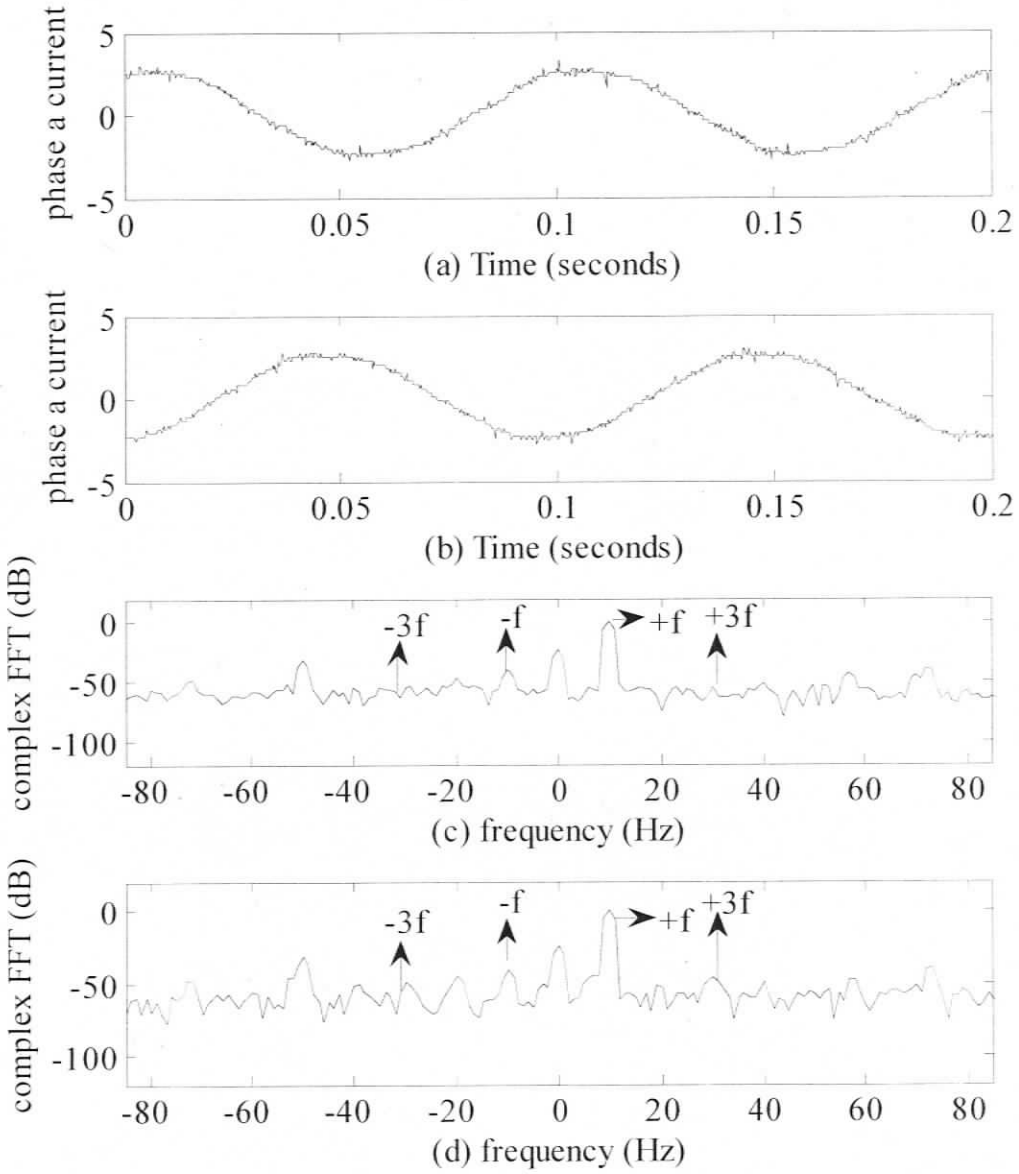

Fig 6.10 (a) two cycles of healthy phase 'A' current; (b) two cycles of single turn fault phase 'A' current; (c) complex FFT of healthy machine; (d) complex FFT of single turn fault machine; plots obtained under frequency of 10 Hz with rotating speed of 293 rpm.

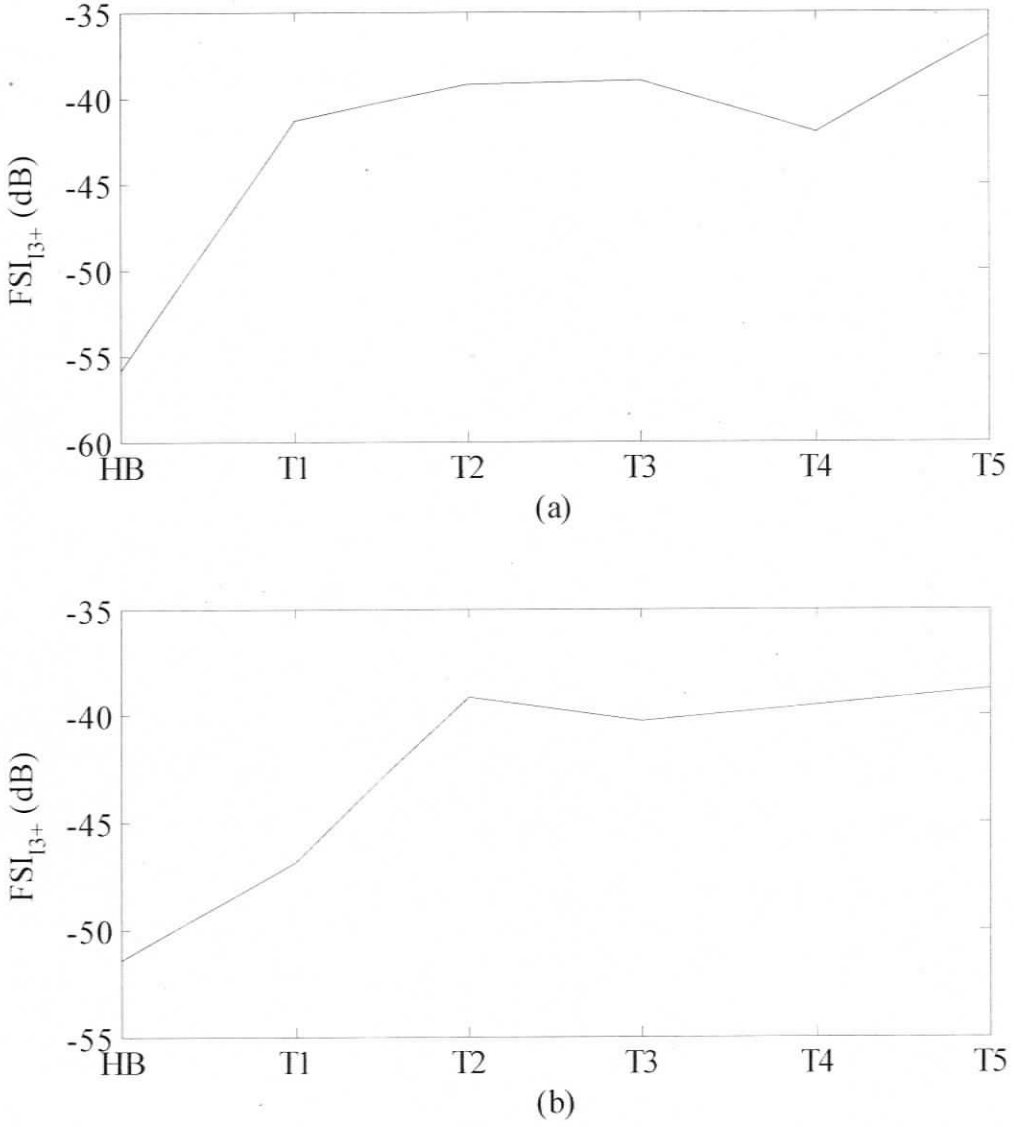

Fig 6.11 FSI_{I3+} versus fault severities under frequency of 10 Hz: (a) at speed of 299 rpm; (b) at speed of 293 rpm.

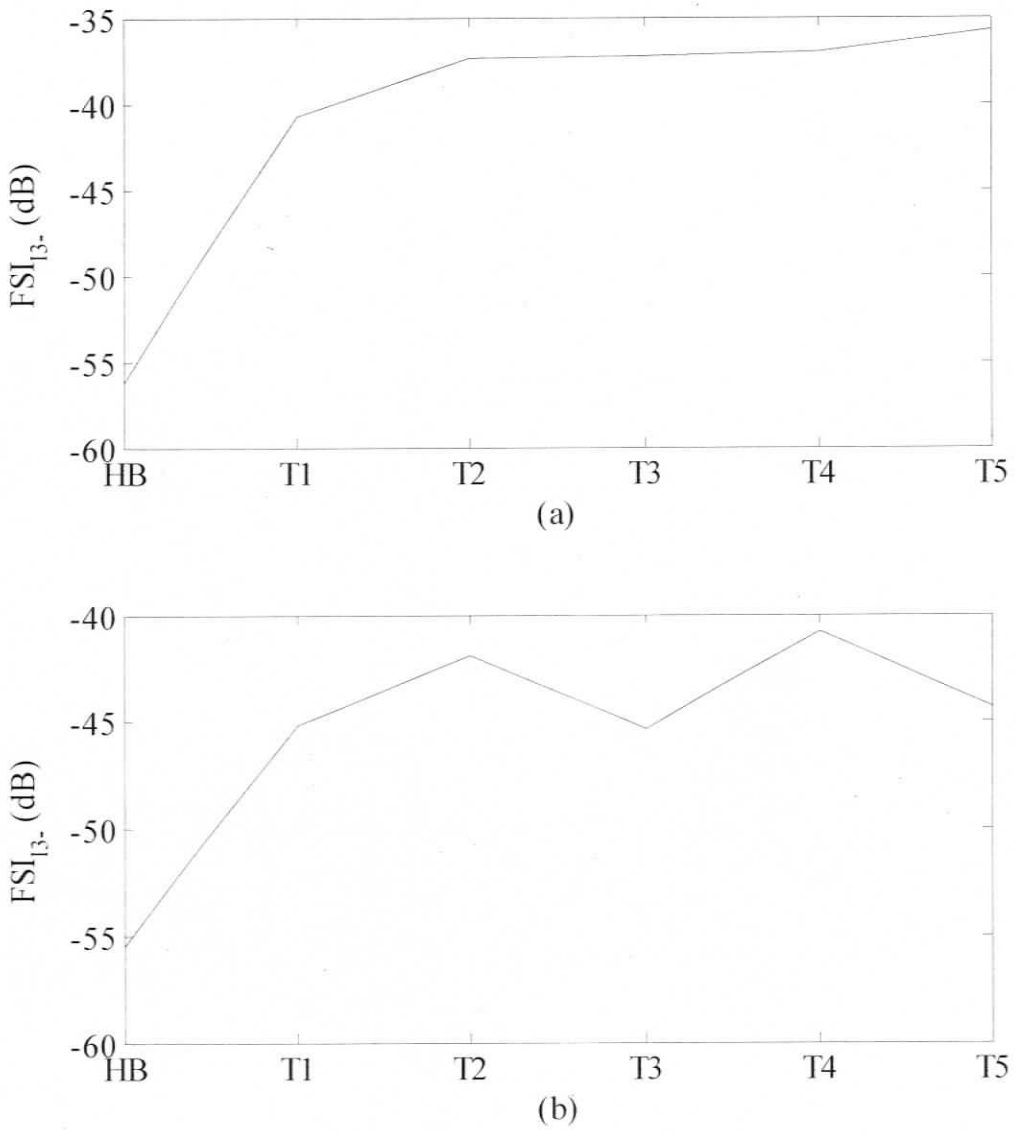

Fig 6.12 FSI_{I3-} versus fault severities under frequency of 10 Hz: (a) at speed of 299 rpm; (b) at speed of 293 rpm.

Table 6.7 FSI_{I3+} versus fault severities under frequency of 10 Hz.

Rotating speed (rpm)	Normalized +3f signature (dB) under different operating points					
	HB	T1	T2	T3	T4	T5
299	-55.89	-41.33	-39.28	-39.02	-42.03	-36.51
293	-51.42	-46.84	-39.11	-40.26	-39.50	-38.73

Table 6.8 FSI_{I3-} versus fault severities under frequency of 10 Hz.

Rotating speed (rpm)	Normalized -3f signature (dB) under different operating points					
	HB	T1	T2	T3	T4	T5
299	-56.18	-40.78	-37.33	-37.27	-37.05	-35.76
293	-55.48	-45.19	-41.95	-45.34	-40.80	-44.30

Additional complex coefficients associating with different types of fault signatures with respect to 30 Hz and 10 Hz can be found in Appendix F.

6.4 Evaluation of Experimental Results

Experimental results based on an inverter-driven induction machine have been shown in this chapter. From fault signatures obtained one can conclude that the effectiveness of proposed ±3f fault signatures in detecting single turn fault have been proved under different operating frequencies and load levels. That is, the inherent structural asymmetry of the machine has been successfully suppressed by subtracting estimated residual ±3f signatures. This proves that the fault signature scheme is robust enough for solid state motor drives also.

Chapter 7
Experiments with Three Phase Delta-connected Induction Machine

7.1 Delta-connected Induction Machine under Test

In order to validate the stator inter-turn fault detection scheme with a different stator winding configurations, in this chapter, faults detection are conducted on a line-fed, delta-connected induction machine. The specification of the motor can be found in Appendix F. The stator winding of induction machine under test has six available terminals as shown in Fig 7.1. Hence either star-connection or delta-connection can be realized. For example, if T4, T5 and T6 are connected together while T1, T2 and T3 are respectively connected to a three phase power supply, then it will form a star-connected stator winding. Otherwise, a delta-connected machine will be obtained if connection is made between T1 and T6, T2 and T4, T3 and T5 with T1, T2, T3 connected to the three phase power supply. The stator winding connection schematic of a delta-connected machine is shown in Table 7.2.

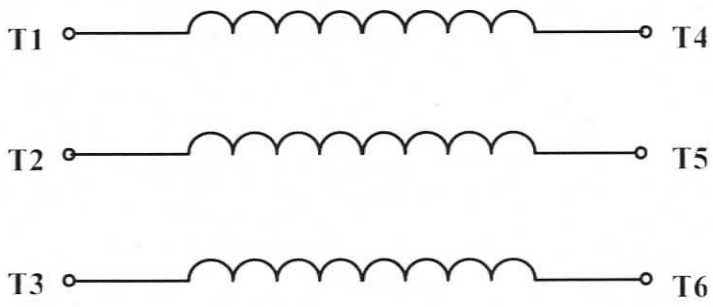

Fig 7.1 Terminals T1 - T6 available for customize connection of the induction machine.

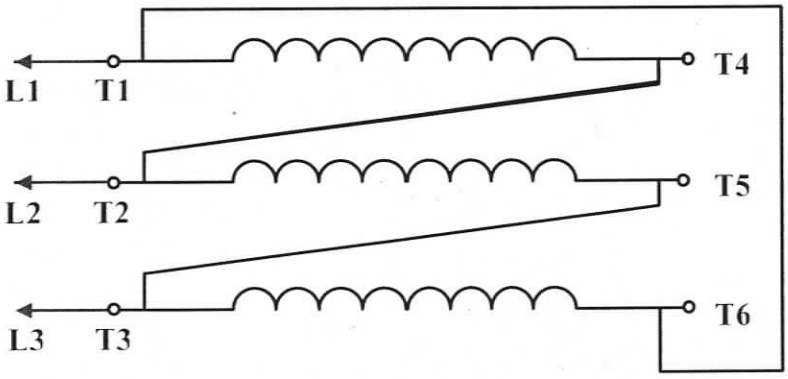

Fig. 7.2 Three phase delta-connection schematic.

In addition to these winding terminals the induction machine also has some other customized terminals for the purpose of carrying out stator inter-turn faults detection. The relative positions of them on stator winding are illustrated in Fig 7.3. It can be seen that the scheme of creating a specific number of shorted turns is different from that of star-connected machine. For example, in delta-connected machine, if five turns need to be shorted, tap "7" and "9" can be connected. This way rewinding cost for motors to be tested for turn-turn faults can be minimized.

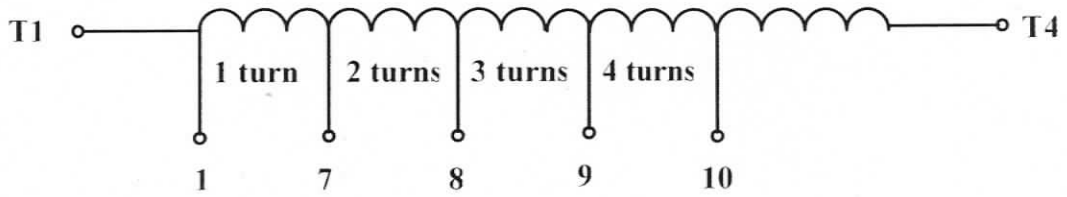

Fig. 7.3 Short-turn creating scheme for line-fed delta-connected induction machine.

While phase voltages are always equal to line voltages in a delta-connected machine, it is not possible to access the phase currents directly from the test. Circuit analysis of three phase systems suggests, however, line currents are correlated with phase currents in a manner which can be described by the following figure.

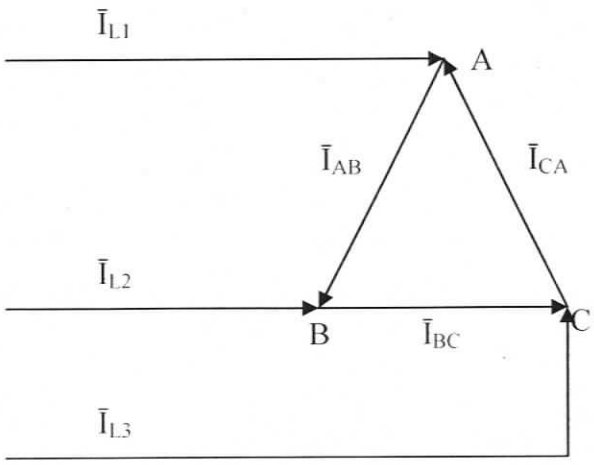

Fig. 7.4 Stator three phase schematic of a delta-connected induction machine.

According to Fig. 7.4 as well as explanation given in [3], relationships between three line and phase currents under balanced condition can be described by the following vector expressions:

$$\bar{I}_{AB} = \frac{\bar{I}_{L1}}{\sqrt{3}} \angle \frac{\pi}{6} \tag{7.1}$$

$$\bar{I}_{BC} = \frac{\bar{I}_{L2}}{\sqrt{3}} \angle \frac{\pi}{6} \tag{7.2}$$

$$\bar{I}_{CA} = \frac{\bar{I}_{L3}}{\sqrt{3}} \angle \frac{\pi}{6} \tag{7.3}$$

As can been seen from above equations, for a delta-connected system, phase current vectors are proportional to line current vectors. Hence, it is possible to conduct proposed stator inter-turn fault detection based on experimentally collected line current data. Experimental results and evaluation are shown in the following sections.

7.2 Experimental Setup and Results

The experimental setup is similar as that has been built for line-fed, star-connected machine test. However, the isolation transformer now works as a step-down transformer (208 V/120 V) because the lower voltage rating of the delta-connected machine. The

variation in supply unbalance is realized through high voltage terminals of the transformer. The rest of the set–up is the same as in star-connected machine.

Following residue estimation accomplished on line-fed, star-connected machine, four types of complex coefficient sets (each has six coefficients), i.e., ($\bar{k}_{I0-} - \bar{k}_{I5-}$), ($\bar{k}_{I0+} - \bar{k}_{I5+}$), ($\bar{k}_{I'0-} - \bar{k}_{I'5-}$) and ($\bar{k}_{I'0+} - \bar{k}_{I'5+}$) are computed separately by nine data sets (one balanced data set + eight unbalanced data sets) from equations (5.1 – 5.4) with $\bar{I}_{I3\pm(e)}$ and $\bar{I}_{I'3\pm(e)}$ replaced by $\bar{I}_{I3\pm(m)}$ and $\bar{I}_{I'3\pm(m)}$. Details of balance and different unbalanced supply voltages can be found from Appendix E. Fault signatures are obtained from equations (5.5 – 5.8) respectively. The resulting ±3f fault signatures are shown in the Figs. 7.5 – 7.8 and Tables 7.1 – 7.4. The different coefficients are listed in Tables 7.5 – 7.8. Also in Appendix H, line current spectra obtained under different operating conditions with respect to different load levels are displayed.

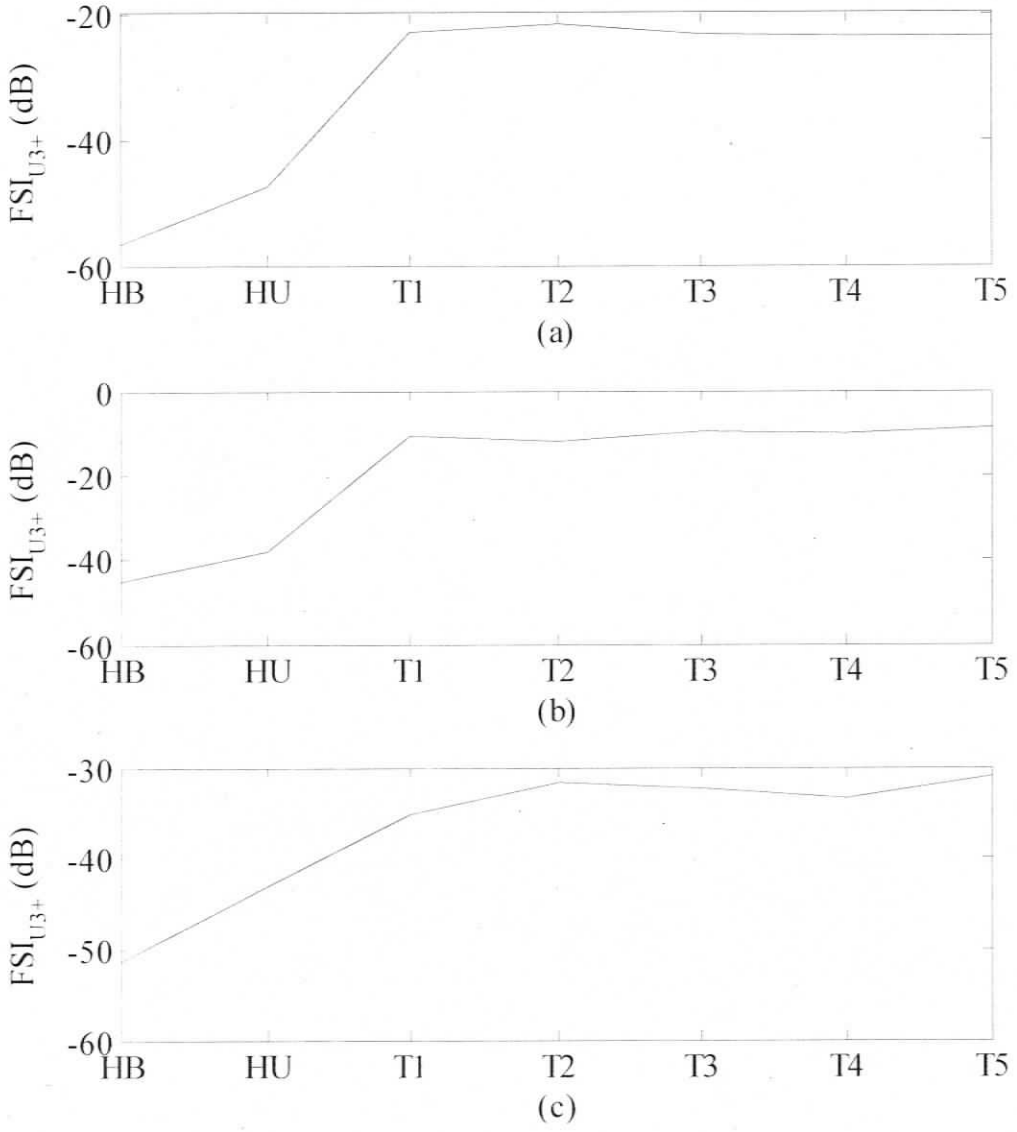

Fig. 7.5 Normalized, FSI_{U3+} versus fault severities under different load conditions, from top to bottom: (a) 1799 rpm (no load); (b) 1780 rpm; (c) 1770 rpm (full load).

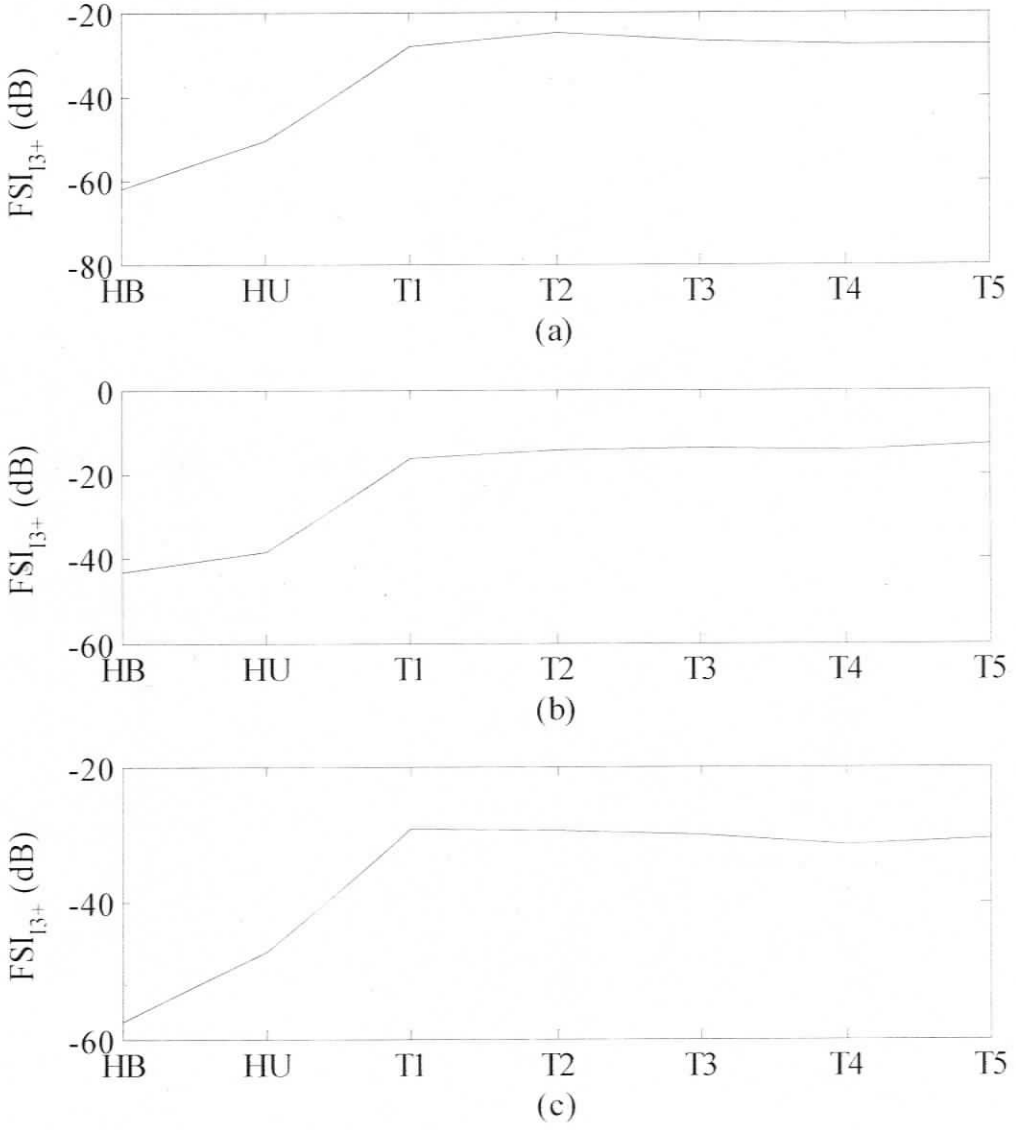

Fig. 7.6 Normalized. FSI_{I3+} versus fault severities under different load conditions, from top to bottom: (a) 1799 rpm (no load); (b) 1780 rpm; (c) 1770 rpm (full load).

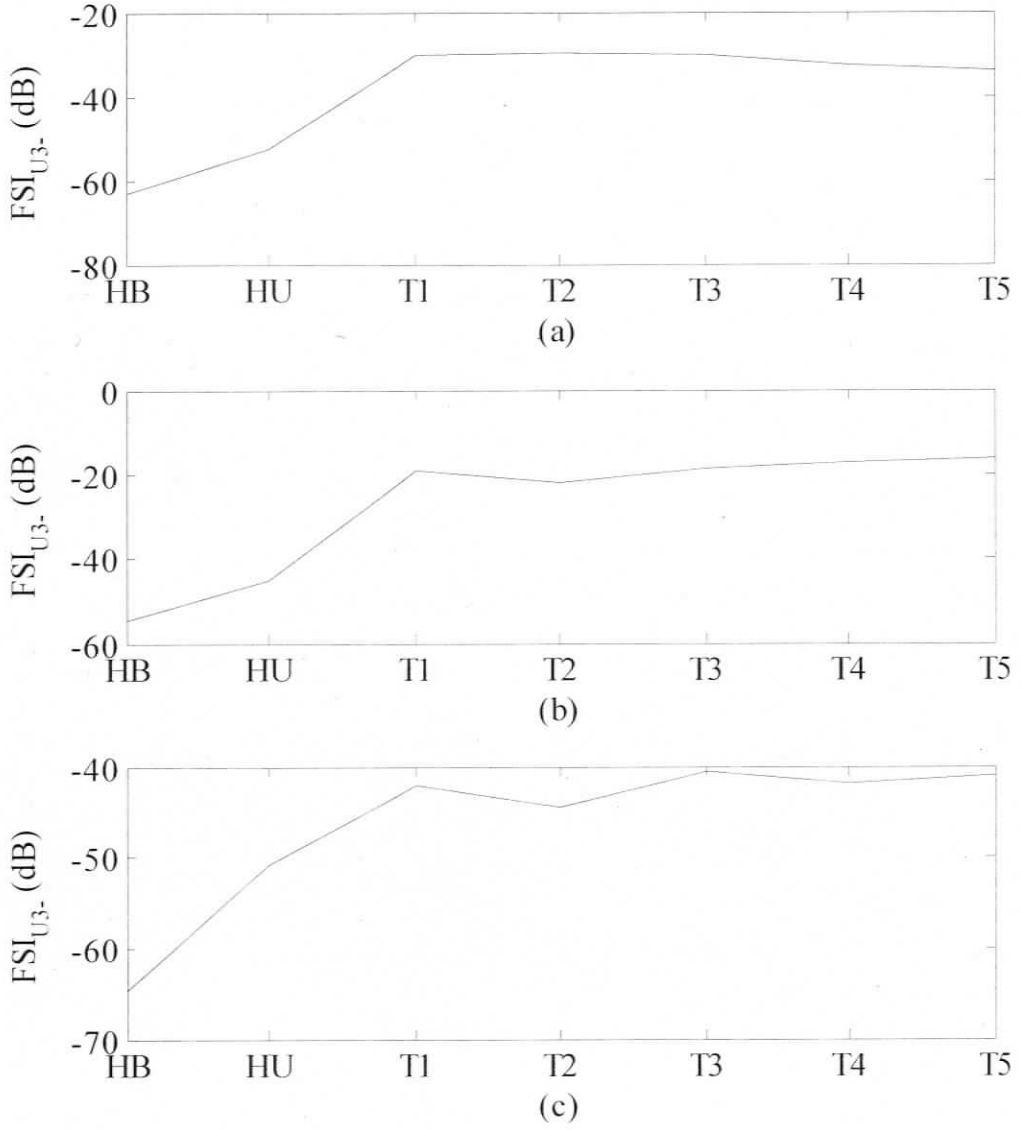

Fig. 7.7 Normalized, FSI_{U3-} versus fault severities under different load conditions. from top to bottom: (a) 1799 rpm (no load); (b) 1780 rpm; (c) 1770 rpm (full load).

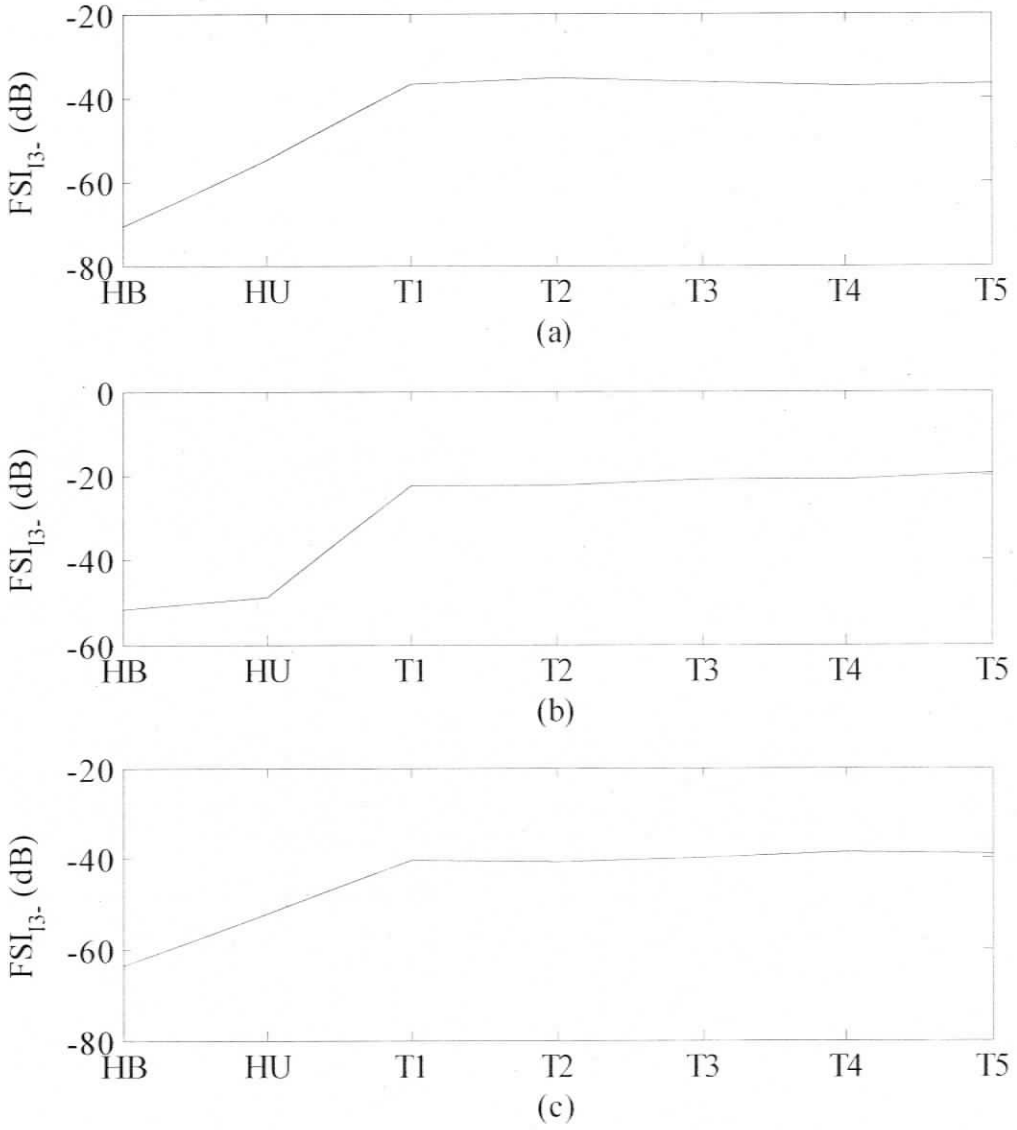

Fig. 7.8 Normalized, FSI_{I3-} versus fault severities under different load conditions, from top to bottom: (a) 1799 rpm (no load); (b) 1780 rpm; (c) 1770 rpm (full load).

Table 7.1 FSI_{U3+} versus fault severities under different load conditions.

Rotating speed (rpm)	Normalized +3f signature (dB) under different operating conditions						
	HB	HU	T1	T2	T3	T4	T5
1799	-56.71	-47.46	-23.09	-21.71	-23.30	-23.69	-23.55
1790	-46.19	-49.86	-24.44	-24.16	-24.92	-22.60	-22.12
1780	-45.07	-38.14	-10.42	-12.23	-9.80	-10.15	-8.90
1770	-51.43	-43.04	-35.04	-31.70	-32.38	-33.48	-31.07

Table 7.2 FSI_{I3+} versus fault severities under different load conditions.

Rotating speed (rpm)	Normalized +3f signature (dB) under different operating conditions						
	HB	HU	T1	T2	T3	T4	T5
1799	-62.3	-50.7	-28.5	-25.0	-26.9	-28.0	-28.0
1790	-51.0	-45.4	-27.2	-25.8	-27.8	-23.7	-23.4
1780	-43.2	-38.5	-16.2	-14.6	-14.0	-14.6	-13.1
1770	-57.4	-47.2	-29.2	-29.5	-29.9	-31.6	-30.6

Table 7.3 FSI_{U3-} versus fault severities under different load conditions.

Rotating speed (rpm)	Normalized -3f signature (dB) under different operating conditions						
	HB	HU	T1	T2	T3	T4	T5
1799	-62.93	-52.64	-30.30	-29.77	-30.13	-32.40	-34.03
1790	-55.55	-56.89	-39.23	-38.84	-39.67	-34.76	-34.34
1780	-54.46	-44.96	-19.08	-22.00	-18.47	-17.31	-16.27
1770	-64.61	-50.79	-42.16	-44.42	-40.58	-41.94	-41.07

Table 7.4 FSI_{I3-} versus fault severities under different load conditions.

Rotating speed (rpm)	Normalized -3f signature (dB) under different operating conditions						
	HB	HU	T1	T2	T3	T4	T5
1799	-70.81	-54.95	-36.72	-35.59	-36.60	-37.28	-36.85
1790	-58.97	-54.89	-37.96	-37.80	-36.16	-33.53	-31.83
1780	-51.74	-48.98	-22.30	-22.49	-21.00	-21.12	-19.61
1770	-63.40	-52.28	-40.25	-40.97	-39.93	-38.69	-39.14

Complex coefficients obtained accordingly are listed in Tables 7.5 and 7.8 respectively for the purpose of comparison.

Table 7.5 $\bar{k}_{U0+} - \bar{k}_{U5+}$ under different load conditions.

Rotating speed (rpm)	$\bar{k}_{U0+}$	$\bar{k}_{U1+}$	$\bar{k}_{U2+}$	$\bar{k}_{U3+}$	$\bar{k}_{U4+}$	$\bar{k}_{U5+}$
1799	0.0060 + 0.0017j	0.0363 - 0.0056j	0.3634 + 0.4166j	0.0876 - 0.0302j	-0.0611 + 0.1964j	0.0773 + 0.0401j
1790	0.0017 - 0.0036j	-0.0272 - 0.0320j	-0.2214 + 2.6195j	-0.0671 + 0.1773j	0.1093 - 0.0665j	-0.0144 - 0.0276j
1780	-0.0108 - 0.0160j	-0.1319 - 0.0020j	-3.1354 + 1.0052j	1.6724 - 0.6969j	-0.2847 + 0.5678j	0.4052 + 0.1983j
1770	0.0033 - 0.0002j	-0.0141 - 0.0112j	0.9037 + 0.0589j	0.1764 + 0.2075j	0.1973 - 0.0922j	0.0557 + 0.1001j

Table 7.6 $\bar{k}_{I0+} - \bar{k}_{I5+}$ under different load conditions.

Rotating speed (rpm)	$\bar{k}_{I0+}$	$\bar{k}_{I1+}$	$\bar{k}_{I2+}$	$\bar{k}_{I3+}$	$\bar{k}_{I4+}$	$\bar{k}_{I5+}$
1799	0.0170 + 0.0478j	0.0485 - 0.0064j	0.2204 + 0.8240j	-1.3808 - 0.0973j	-1.2537 + 0.5322j	0.6136 + 0.0047j
1790	0.0187 + 0.0140j	0.0009 - 0.1383j	-5.6190 + 5.4398j	-0.8610 + 0.7017j	0.6480 - 0.7357j	0.4221 - 0.2407j
1780	0.0077 - 0.0580j	-0.1789 - 0.1249j	-5.7722 - 1.9101j	-8.9213 + 1.3978j	-0.7792 - 0.7549j	-1.1692 - 3.4838j
1770	0.0063 + 0.0175j	-0.0532 - 0.0386j	0.1426 - 1.6996j	0.1272 - 2.7301j	-0.3863 + 0.6070j	1.0543 + 0.3427j

Table 7.7 $\bar{k}_{U0-}$ - $\bar{k}_{U5-}$ under different load conditions.

Rotating speed (rpm)	$\bar{k}_{U0-}$	$\bar{k}_{U1-}$	$\bar{k}_{U2-}$	$\bar{k}_{U3-}$	$\bar{k}_{U4-}$	$\bar{k}_{U5-}$
1799	0.0023 - 0.0008j	0.0104 - 0.0086j	0.1938 + 0.1229j	-0.0219 - 0.0826j	0.0289 + 0.0765j	0.0081 + 0.0008j
1790	0.0002 + 0.0008j	0.0172 + 0.0045j	-0.2264 - 0.3327j	0.0364 - 0.0232j	0.0046 + 0.0059j	-0.0101 + 0.0060j
1780	-0.0068 + 0.0057j	-0.0001 + 0.0685j	0.8127 + 1.3852j	-0.3772 - 0.7551j	0.2302 + 0.1200j	0.0920 - 0.2038j
1770	0.0001 + 0.0008j	-0.0091 + 0.0119j	0.4856 + 0.1089j	-0.0009 + 0.0777j	0.0515 - 0.0293j	-0.0045 + 0.0426j

Table 7.8 $\bar{k}_{I0-}$ - $\bar{k}_{I5-}$ under different load conditions.

Rotating speed (rpm)	$\bar{k}_{I0-}$	$\bar{k}_{I1-}$	$\bar{k}_{I2-}$	$\bar{k}_{I3-}$	$\bar{k}_{I4-}$	$\bar{k}_{I5-}$
1799	0.0118 + 0.0063j	0.0182 - 0.0115j	0.3356 + 0.0923j	-0.5079 + 0.3756j	-0.2490 + 0.4208j	-0.0588 + 0.1146j
1790	-0.0063 + 0.0012j	0.0125 + 0.0083j	0.4621 - 0.6504j	0.1123 - 0.5304j	0.0532 + 0.1896j	0.0368 + 0.2670j
1780	-0.0212 - 0.0080j	-0.0267 + 0.0783j	-0.2781 + 1.6533j	-0.9678 + 3.2527j	-0.4411 + 0.0165j	-1.3894 - 0.1716j
1770	-0.0020 + 0.0057j	0.0015 + 0.0348j	0.3405 + 0.2386j	-0.3540 - 1.0902j	-0.0669 + 0.2317j	0.5466 - 0.0226j

7.3 Evaluation of Experimental Results

Obviously for both +3f and -3f fault signatures, after estimated residues are removed from measured values, very distinctive T1 fault signatures can be obtained. i.e., very clear discrimination can be achieved between 'T1' and 'HB' as well as 'HU'. Distinguishable coefficients with respect to different type of fault signatures and operating point have also been obtained. Conclusion can thus be made that +3f and -3f signatures are trustable fault indictors for delta-connected induction machines also.

Chapter 8

Conclusions and Future Work

8.1 Conclusions

In this work, the condition monitoring of induction machines has been addressed for stator inter-turn faults. Initially the concept of negative frequency is established based on line voltage as well as current space vectors. Feasibility of detecting stator inter-turn faults is conducted by analyzing ±3f line current components under varying operating conditions. The origin of ±3f line current components was attributed to a variety of influencing factors such as permeance harmonics, space harmonics, time harmonics as well as fault current. Based on the results from the analysis, the methodology of estimating inherent machine structural asymmetry and supply unbalance are developed by employing least-square estimation technique.

The model of three phase induction machine has been built based on MWFA. The machine transient can be seen clearly from the results of dynamic simulation. By including saturation, stator inter-turn faults into the model, simulated line currents were utilized to validate proposed fault signatures. Theoretical prediction to distinguish +3f and -3f fault signatures with respect to different operating conditions have been proved from both ideally (harmonics-free) as well as experimentally collected voltage data.

A series of rigorous experiments have been carried out which involves testing the induction machines under healthy, stator inter-turn fault and supply unbalance conditions. In order to test the machines under faulty condition, customized induction machine with different taps have been used to emulate inter-turn fault of stator windings. Prior to detecting proposed ±3f fault signatures, another very common fault signature, i.e., line current negative sequence component (-f) was tested and its inadequacy in detecting incipient inter-turn fault is demonstrated. Subsequently, proposed ±3f fault signatures are computed based on the theoretical analysis. It can be seen clearly that despite changing

stator winding configuration and voltage supplies, both +3f and -3f fault signatures can decisively indicate single turn faults. The universal effectiveness of proposed fault signature is thereby verified.

To sum up, the contributions arising out of the work presented in this thesis are the following:

- Experimentally prove that residue-elimination method applied on a line current negative sequence component cannot clearly indicate single turn faults.
- Explicit analysis of the cause of ±3f line current harmonic components under different operating conditions. Application of least-square method in estimating residual ±3f components.
- Verify the differences among different types of fault signatures under same operating conditions by using simulated current data. Simulations are conducted based on either harmonics-free as well as experimentally collected voltage data.
- The robustness of proposed fault signatures is claimed by carrying out a variety of experiments including line-fed, star-connected, delta-connected and inverter-fed induction machines. In each case, computed fault signatures can very decisively indicate single turn faults.

8.2 Future Scope

Based on the results furnished in this thesis, different complex coefficients have been computed in an attempt to attain unambiguous fault indicators under some particular load levels. However fault detection should be made possible at any load level. However it is physically impossible to compute the complex coefficients for all possible load points. Therefore, as the next stage of this scheme, the development of a set of coefficients which are capable of decisively indicate a single turn fault under any load level becomes necessary. It is to be researched whether these coefficients can be derived by using interpolation of sets of coefficients obtained at other load points.

Secondly, although the fault detection scheme has been validated through a series of experiments, its real-time implementation in an attempt to disconnect a faulty machine unambiguously has not been included in this thesis. This also needs to be addressed to in the next part of the research. Although quite powerful DSP devices are available, fast computation of complex FFT and interpolation remain as major hurdles to be overcome.

Bibliography

[1]. A. R. Hambley, *Electrical Engineering Principles and Applications*, Third Edition, Upper Saddle River, New Jersey, 2004.

[2]. M. S. Sarma, *Electric Machines Steady-State Theory and Dynamic Performance*, Dubuque, Iowa, 1985.

[3]. P.C Sen, *Principles of Electrical Machines and Power Electronics*, John Wiley & Sons Inc. 1996.

[4]. P. L. Alger, *Induction Machines Their Behavior and Uses*, Troy, New York, 1970.

[5]. W. Leonhard, *Control of Electrical Drives*. Springer-Verlag: Berlin, 2001.

[6]. Li. Xiaodong, *Performance Analysis of a 3-Phase Induction Machine with Inclined Static Eccentricity*, M. A. Sc thesis, University of Victoria, Victoria, 2004.

[7]. P. Neti, *Stator Fault Analysis of Synchronous Machines*, Ph. D thesis, University of Victoria, Victoria. 2007.

[8]. S. Nandi, H. A. Toliyat and X. Li, "Condition monitoring and fault diagnosis of electrical motors - a review," *IEEE Transactions on Energy Conversion*, Vol. 20, No. 4, pp. 719-729, Dec. 2005.

[9]. A. J. Ellison and S. J. Yang, "Effects of rotor eccentricity on acoustic noise from induction machines," *Proceedings of IEE*, Vol. 118, no. 1, pp. 174-184, 1971.

[10]. J. R. Cameron, W.T. Thomson, and A. B. Dow, "Vibration and current monitoring for detecting air-gap eccentricity in large induction motors," *Proceedings of IEE*, Vol. 133, pt. B, No. 3, pp. 155-163, May 1986.

[11]. D. G. Dorrell, W. T. Thomson, and S. Roach, "Analysis of airgap flux, current, vibration signals as a function of the combination of static and dynamic airgap eccentricity in 3-phase induction motors," *IEEE Transactions on Industry Applications*, Vol. 33, no. 1, pp. 24–34, Jan./Feb. 1997.

[12]. S. A. McInerny and Y. Dai, "Basic vibration signal processing for bearing fault detection," IEEE Transactions on Education, Vol. 46, no. 1, pp. 149–156, Feb. 2003.

[13]. H.A. Toliyat, Mohammed S. Arefeen, Alexander, G. Parlos, "A Method for Dynamic Simulation of Air-Gap Eccentricity in Induction Machines," *IEEE transactions on Industry Applications*, Vol. 32, Issue 4, July-Aug, pp. 910 – 918, 1996.

[14]. M. E. H. Benbouzid, E. Hachemi, "A review of induction motors signature analysis as a medium for faults detection," *IEEE Transactions on Industrial Electronics,* Vol. 47, No. 5, pp. 984–993, Oct. 2000.

[15]. M. E. H. Benbouzid, G. B. Kliman, "What stator current processing based technique to use for induction motor rotor faults diagnosis?" *IEEE Transactions on Energy Conversion,* Vol. 18, No. 2, pp. 238–244, Jun. 2003.

[16]. F. Filippetti, G. Franceschini, and C. Tassoni, "Neural networks aided on-line diagnostics of induction motor faults," IEEE Transaction on Induction Applications, Vol. 31, No. 4, Jul./Aug. 1995

[17]. J. Penman and C. M. Yin, "Feasibility of using unsupervised learning, artificial neural networks for the condition monitoring of electrical machines," *IEE Proceeding of Electrical and Power Applications*. Vol. 141, No. 6, pp. 317-322, Nov. 1994

[18]. P. Vas, *Ariificial-Intelligence-Based Electrical Machines and Drives: Applications of Fuzzy, Neural, Fuzzy-Neural and Genetic Algorithm Based Techniques*. New York, Oxford University Press, 1999.

[19]. F. Filippetti, G. Franceschini, C. Tassoni, and P. Vas, "Recent developments of induction motor drives fault diagnosis using AI techniques," *IEEE Transactions on Industrial Electronics*, Vol. 47, NO. 5, pp. 994–1004, Oct. 2000.

[20]. M. Y. Chow, *Methodologies of Using Neural Network and Fuzzy Logic Technologies for Motor Incipient Fault Detection*, Singapore: World Scientific, 1997.

[21]. G. B. Kliman, W. J. Premerlani, R. A. Koegl, and D. Hoeweler, "A new approach to on-line fault detection in ac motors," *IEEE Industry Applications Society Annual Meeting Conference,* San Diego, CA, pp. 687–693, Oct. 1996.

[22]. S. Nandi and H. A. Toliyat, "Novel frequency domain based technique to detect stator inter-turn faults in induction machines using stator induced voltage after switch-off," *IEEE Transaction on Industrial Applications*, Vol. 38, No. 1, pp. 101–109, Jan./Feb. 2002.

[23]. S. Nandi, "Detection of Stator Faults in Induction Machines Using Residual Saturation Harmonics," *IEEE Transactions on Industry Applications,* Vol. 42, Issue 5, Sep. – Oct. pp. 1201– 1208, 2006.

[24]. G. Stone and J. Kapler, "Stator winding monitoring," *IEEE Industry Applications Magazine*, Vol. 4, No. 5, pp. 15–20, Sep./Oct. 1998.

[25]. A. K. Sawhney, *Electrical Machine Design*, Nai Sarak, Delhi, 1984.

[26]. Gojko M. Joksimovic', and Jim Penman "The Detection of Inter-Turn Short Circuits in the Stator Windings of Operating Motors," *IEEE Transactions on Industrial Electronics*, Vol. 47, Issue 5, Oct. 2000, pp. 1078 – 1084, 2000.

[27]. S. Nandi, "A Detailed Model of Induction Machines With Saturation Extendable for Fault Analysis," *IEEE Transaction on Industry Applications*, Vol. 40, No. 5, Sep/Oct, 2004.

[28]. H. A. Toliyat and T. A. Lipo, "Transient analysis of cage induction machines under stator, rotor bar and end ring faults," *IEEE Transactions on Energy Conversion*, Vol. 10, No. 2, pp. 241–247, Jun. 1995.

[29]. Rangarajan M. Tallam, Thomas G. Habetler and Ronald G. Harley, "Transient Model for Induction Machines with Stator Winding Turn Faults", *Industry Applications Conference*, Vol. 1, pp. 304 - 309, Oct. 2000.

[30]. P. Neti and S. Nandi, "An Improved Strategy to Detect Stator Inter-turn Faults in Synchronous Reluctance Motors Using Both Negative Sequence Quantities and Stored Magnetic Energy After Supply Disconnection", *IEEE Industry Applications Conference*, Page(s), 2234-2241, Sept., 2007.

[31]. M. Arkan, D. K. Perovic, and P. Unsworth, "Online stator fault diagnosis in induction motors," *Proceeding of IEE, Electric Power Applications*, Vol. 148, No. 6, pp. 537–547, Nov. 2001.

[32]. J. L. Kohler, J. Sottile and F. C. Trutt, "Alternatives for assessing the electrical integrity of induction motors", *IEEE Transactions on Industry Applications*, Vol. 28, no. 5, pp.1109-1117, Sept./Oct. 1992.

[33]. J. L. Kohler, J. Sottile and F. C. Trutt, "Condition monitoring of stator windings in induction motors. I. Experimental investigation of the effective negative-sequence impedance detector," *IEEE Transactions on Industry Applications*, Vol. 38, no. 5, pp. 1447-1453, Sept./Oct. 2002.

[34]. J. Sottile F. C. Trutt and J. L. Kohler, "Condition monitoring of stator windings in induction motors. II. Experimental investigation of voltage mismatch detectors," *IEEE Transactions on Industry Applications*, Vol. 38, no. 5, pp. 1454-1459, Sept./Oct. 2002.

[35]. Sang Bin Lee, R. M. Tallam and T. G. Habetler, "A robust, on-line turn-fault detection technique for induction machines based on monitoring the sequence component impedance matrix," *IEEE Transactions on Industry Applications*, Vol. 18, no.3, pp. 865-872, May 2003.

[36]. S. M. A. Cruz and A. J. M. Cardoso, "Diagnosis of stator inter-turn short circuits in DTC induction motor drives," in *Proceeding, IEEE Industry Applications Conference Annual Meeting Conference*, Salt Lake City, UT, pp. 1332–1339, 2003.

[37]. S. M. A. Cruz, A. J. M. Cardoso, and H. A. Toliyat, "Diagnosis of stator, rotor, and airgap eccentricity faults in three-phase induction motors based on the multiple reference frames theory," in *Proceeding, 38th Industry Applications Annual Meeting Conference*, Salt Lake City, UT, Oct, pp. 1340–1346, 2003.

[38]. M. E. H. Benbouzid, M. Vieira, and C. Theys, "Induction motors faults detection and localization using stator current advanced signal processing techniques," *IEEE Transactions on Power Electronics*, Vol. 14, No. 1, pp. 14–22, Jan. 1999.

[39]. S. M. A. Cruz and A. J. M. Cardoso, "Stator winding fault diagnosis in three-phase synchronous and asynchronous motors, by the extended Park's vector approach," *IEEE Transactions on Industry Applications*, Vol. 37, no.5, pp. 1227-1233, Sept./Oct. 2001.

[40]. L. Collamati, F. Filippetti, G. Franceschini, S. Pirani, and C. Tassoni, "Induction motor stator fault on-line diagnosis based on labview environment," in *Proceeding of Mediterranean Electrotechnical Conference*, Vol. 1, pp. 495–498, 1996.

[41]. J. Penman, H. G. Sedding, B. A. Lloyd, and W. T. Fink, "Detection and location of interturn short circuits in the stator windings of operating motors," *IEEE Transactions on Energy Conversion*, Vol. 9, No. 4, pp. 652–658, Dec. 1994.

[42]. H. Henao, C. Demian, and G. A. Capolino, "A frequency-domain detection of stator winding faults in induction machines using an external flux sensor," *IEEE Transactions on Industry Application*, Vol. 39, No. 5, pp. 1272–1279, Sep./Oct. 2003.

[43]. T. Liu and J. Huang, "A Novel Method for Induction Motors Stator Interturn Short Circuit Fault Diagnosis by Wavelet Packet Analysis," *Proceedings of 8th International Conference on Electrical Machines and Systems*, Vol. 3, pp. 2254-2258, Sept. 2005.

[44]. M. A. Cash, T. G. Habetler and G. B. Kliman, "Insulation failure prediction in AC machines using line-neutral voltages," *IEEE Transactions on Industry Applications*, Vol. 34, no.6, pp. 1234-1239, Nov./Dec. 1998.

[45]. A. Stavrou, H. Sedding, and J. Penman, "Current monitoring for detecting inter-turn short circuits in induction motors," in *Proceeding of International Conference of Electric Machines Drives*, May 9–12, pp. 345–347, 1999.

[46]. F. Briz, M. W. Degner, A. Zamarron, and J. M. Guerrero, "Online stator winding fault diagnosis in inverter-fed AC machines using high-frequency signal injection," *IEEE Transactions of Industry Applications Society*, Vol. 39, No. 4, pp. 1109–1117, Jul./Aug. 2003.

[47]. D. Kostic-Perovic, M. Arkan, and P. Unsworth, "Induction motor fault detection by space vector angular fluctuation," in *Proc. IEEE Industry Applications Conference*, Vol. 1, Oct. 8–12, pp. 388–394, 2000.

[48]. Julio C. Moreira, and Thomas A. Lipo, "Modeling of Saturated AC Machines Including Air Gap Flux Harmonic Components," *IEEE Transactions on Industry Applications*, Vol. 28, Issue 2, March-April, pp. 343 – 349, 1992.

[49]. G. Kron, Equivalent Circuits of Electric Machinery. New York, John Wiley & Sons Inc., 1951.

[50]. J. H. McClellan, R. W. Schafer, and M. A. Yoder, *Signal Processing First*, Prentice Hall, New Jersey, 2003.

[51]. Neti. P, Nandi. S, "Performance Analysis of a Reluctance Synchronous Motor under Abnormal Operating Condition", *IEEE Canadian Conference on Electrical and Computer Engineering*, Vol. 1, 2-5 May 2004, 2004.

[52]. Alexander S. Langsdorf, *Theory of alternating-current machinery*, 2nd Edition, McGraw Hill, Kogakusha, Tokyo, 1955.

[53]. M. Gopal, *Modern Control System Theory*, 2nd Edition, New Age International Publishers, New Delhi, 1993.

[54]. "MATLAB" 7.0, The MathWorks Inc., 2004.

[55]. N. A. Al-Nuaim and H. A. Toliyat, "A Novel Method for Modeling Dynamic Air-Gap Eccentricity in Synchronous Machines Based on Modified Winding Function Theory", *IEEE Transactions on Energy Conversion*, Vol. 13, No. 2, June 1998.

Appendix A

Detailed Description of Least-square Method

Considering non-homogeneous linear algebraic equations given as below [53]:

$$\mathbf{A.x} = \mathbf{b} \tag{A.1}$$

where

$$\mathbf{A} \overset{\Delta}{=} \begin{bmatrix} a_{11} & a_{12} & \dots a_{1n} \\ a_{21} & a_{22} & \dots a_{2n} \\ \vdots & \vdots & \vdots \\ a_{m1} & a_{m2} & \dots a_{mn} \end{bmatrix}$$

$$\mathbf{x} \overset{\Delta}{=} \begin{bmatrix} x_1 \\ x_2 \\ \vdots \\ x_n \end{bmatrix}; \quad \mathbf{b} \overset{\Delta}{=} \begin{bmatrix} b_1 \\ b_2 \\ \vdots \\ b_m \end{bmatrix}$$

$$\mathbf{(A: b)} = \begin{bmatrix} a_{11} & a_{12} & \dots a_{1n} & b_1 \\ a_{21} & a_{22} & \dots a_{2n} & b_2 \\ \vdots & \vdots & \vdots & \vdots \\ a_{m1} & a_{m2} & \dots a_{mn} & b_n \end{bmatrix} \overset{\Delta}{=} \left[\mathbf{a}_1\ \mathbf{a}_2 \dots \mathbf{a}_n\ \mathbf{b}\right]$$

Define

$\rho(\mathbf{A})$ = rank of matrix **A**;

$\rho(\mathbf{A: b})$ = rank of matrix **(A: b)**:

n = the number of columns in matrix **A**.

(i) If $\rho(\mathbf{A}) = \rho(\mathbf{A: b})$ then equations (A.1) are consistent and have one or more solutions.

(ii) If $\rho(\mathbf{A}) < \rho(\mathbf{A: b})$ then equations (A.1) are inconsistent and only have least square solution.

The equations used in this thesis are given as (3.40). Matrix **A** is formed from measured different line current or voltage harmonic components with each row is obtained by repeating the same data acquisition process. Hence, slight variations can be observed

between different rows which will results in an inconsistency between any two rows. In addition, more rows than columns in **A** will lead to $\rho(\mathbf{A}) < \rho(\mathbf{A}: \mathbf{b})$. As the result the solving of (3.40) will follow the principles presented in case (ii). i.e., only a least square solution can be obtained. The solution of case (ii) can be further discussed under two different conditions which are given as below.

If $\rho(\mathbf{A}) = n$, suppose the sum of squares of the residues of (A.1) is given as

$S = (\mathbf{b} - \mathbf{Ax})^T (\mathbf{b} - \mathbf{Ax})$ or (A.2)

$S = \mathbf{b}^T\mathbf{b} - \mathbf{x}^T\mathbf{A}^T\mathbf{b} - \mathbf{b}^T\mathbf{Ax} + \mathbf{x}^T\mathbf{A}^T\mathbf{Ax}$

Setting

$$\frac{\partial S}{\partial x_j} = 0; \quad j = 1, 2, \ldots, n$$

One can get

$\mathbf{A}^T\mathbf{Ax} = \mathbf{A}^T\mathbf{b}$

The matrix $\mathbf{A}^T\mathbf{A}$ is non-singular. Therefore, a unique solution can be obtained as:

$\mathbf{x} = (\mathbf{A}^T\mathbf{A})^{-1}\mathbf{A}^T\mathbf{b}$ (A.3)

If $\rho(\mathbf{A}) < n$, suppose the sum of squares of the residues and the sum of the squares of the unknowns are respectively given as $(\mathbf{b} - \mathbf{Ax})^T (\mathbf{b} - \mathbf{Ax})$ and $\mathbf{x}^T\mathbf{x}$. Then by minimizing both of them the following least square solution can be obtained,

$\mathbf{x} = \mathbf{C}^T(\mathbf{CC}^T)^{-1}(\mathbf{B}^T\mathbf{B})^{-1}\mathbf{B}^T\mathbf{b}$ (A.4)

here $\mathbf{A} = \mathbf{BC}$; **A**, **B** and **C** are respectively $m \times n$, $m \times k$, $k \times n$ matrices and all the three matrices are of rank k ($k < n$).

According to the observation of equations (3.40), matrix **A** established in this thesis is in accordance with the first case. i.e., $\rho(\mathbf{A}) = n$. Therefore, (A.3) is followed to obtain the least square solution.

Appendix B

Mathematical Derivation of Generalized MMF Harmonics

In [49], a generalized expression of air gap MMF harmonics of a polyphase system is derived. Following the similar procedure, n^{th} MMF space harmonics produced by h^{th} time harmonic of a healthy and balanced three phase system is derived. Procedures are given as below.

A set of positive sequence MMF waves generated from three phase system fed by three phase sinusoidal power supply are expressed as,

$$\begin{aligned} f_{A+} &= F_m \sin(np\theta)\cos(h\omega t) \\ f_{B+} &= F_m \sin(np(\theta - \frac{2\pi}{3}))\cos(h(\omega t - \frac{2\pi}{3})) \\ f_{C+} &= F_m \sin(np(\theta - \frac{4\pi}{3}))\cos(h(\omega t - \frac{4\pi}{3})) \end{aligned} \tag{B.1}$$

By employing the following trigonometric identity

$$\sin A\cos B = \frac{1}{2}[\sin(A+B) + \sin(A-B)]$$

(B.1) can be summed into one expression which represents total air gap MMF distribution from all the three phase windings,

$$f_{sum+} = \frac{3F_m}{2}\sum_{k=1}^{3}\left(\begin{array}{l} \sin[np\theta + h\omega t - (k-1)(n+h)\frac{2\pi}{3}] \\ +\sin[np\theta - h\omega t - (k-1)(n-h)\frac{2\pi}{3}] \end{array}\right) \tag{B.2}$$

(B.2) can be further simplified after a series of mathematical transform shown as below,

$$f_{sum+} = \frac{3F_m}{2}\left(\begin{array}{l} \frac{\sin(n+h)\pi}{\sin[(n+h)\pi/3]}\sin(P - \frac{2(n+h)\pi}{3}) \\ +\frac{\sin(n-h)\pi}{\sin[(n-h)\pi/3]}\sin(Q - \frac{2(n-h)\pi}{3}) \end{array}\right) \tag{B.3}$$

Here P and Q are given respectively as,

$P = np\theta + h\omega t$

$Q = np\theta - h\omega t$

Note here that both sin $(n + h)\ \pi$ and sin $(n - h)\ \pi$ are always zero hence equation (B.3) will be zero. The only exception is that when sin $(n + h)\ \pi/3$ or sin $(n - h)\ \pi/3$ are also zero. Then applying L'Hospital's rule:

$$\frac{\sin(n+h)\pi}{\sin[(n+h)\pi/3]} = 3, \text{ and}$$

$$\frac{\sin(n-h)\pi}{\sin[(n-h)\pi/3]} = 3 \qquad \text{(B.4)}$$

Therefore, if conditions given in (B.4) are satisfied, a meaningful MMF space harmonics will be obtained. Equation (B.3) is sufficiently general to determine any n^{th} MMF space harmonic produced by any h^{th} current time harmonic. It can be employed to find out the rotating direction of any specific air gap MMF space harmonic. For example, substituting $n = 1$, $h = 7$ into (B.3) will result in the following expression,

$$f_{5+} = \frac{9F_m}{2}\sin(p\theta - 7\omega t) \qquad \text{(B.5)}$$

(B.5) represents fundamental MMF space harmonic arise from 7^{th} current time harmonic. The same conclusion can also be found in [3]. Minus sign in front of '$7\omega t$' indicates that the MMF is rotating in the forward direction. Similarly, any other n^{th} MMF space harmonic produced by h^{th} current time harmonic can be derived.

Equation (B.3) is obtained under ideal three phase system powered by ideally balanced three phase power supply. Since any actual machine will have structural imperfection and some unbalance in supply, a series of backward rotating magnetic field (compare with forward rotating MMF given in (B.1) arising from ideal condition) will be established [5] as the following,

$$\begin{aligned} f_{A-} &= F_m \sin(np\theta)\cos(h\omega t) \\ f_{B-} &= F_m \sin(np(\theta - \frac{2\pi}{3}))\cos(h(\omega t + \frac{2\pi}{3})) \\ f_{C-} &= F_m \sin(np(\theta - \frac{4\pi}{3}))\cos(h(\omega t + \frac{4\pi}{3})) \end{aligned} \qquad \text{(B.6)}$$

Following similar procedure, a generalized n^{th} MMF space harmonic produced by h^{th} current time harmonic under structural imperfection and supply unbalance will be obtained as,

$$f_{sum-} = \frac{3F_m}{2}\left(\begin{array}{l}\dfrac{\sin(n-h)\pi}{\sin(n-h)\pi/3}\sin(P-\dfrac{2(n-h)\pi}{3}) \\ +\dfrac{\sin(n+h)\pi}{\sin(n+h)\pi/3}\sin(Q-\dfrac{2(n+h)\pi}{3})\end{array}\right) \tag{B.7}$$

(B.7) represents the group of reverse rotating MMF harmonics. For example, substituting $n = 1$, $h = 7$ into (B.7) will result in the following expression.

$$f_{5+} = \frac{9F_m}{2}\sin(p\theta + 7\omega t) \tag{B.8}$$

Plus sign in front of '$7\omega t$' indicate that the MMF is rotating in the reverse direction.

Appendix C

Simulated No load Line Current Spectra

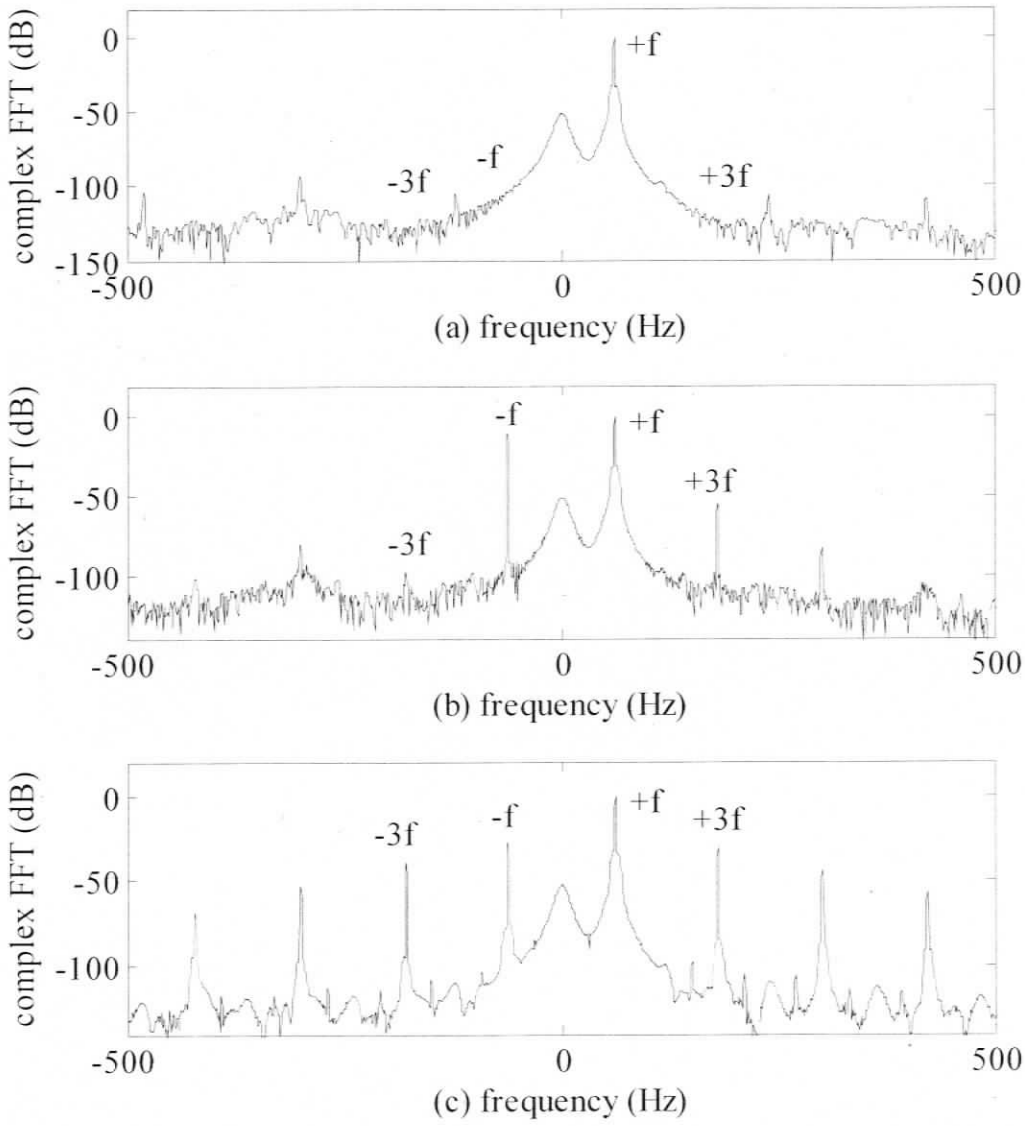

Fig C.1 Simulated line current spectra under no load condition: healthy machine with ideally balanced supply (top); healthy machine with unbalanced supply (middle): single-turn fault machine with balanced supply (bottom); simulated by harmonics-free voltage data.

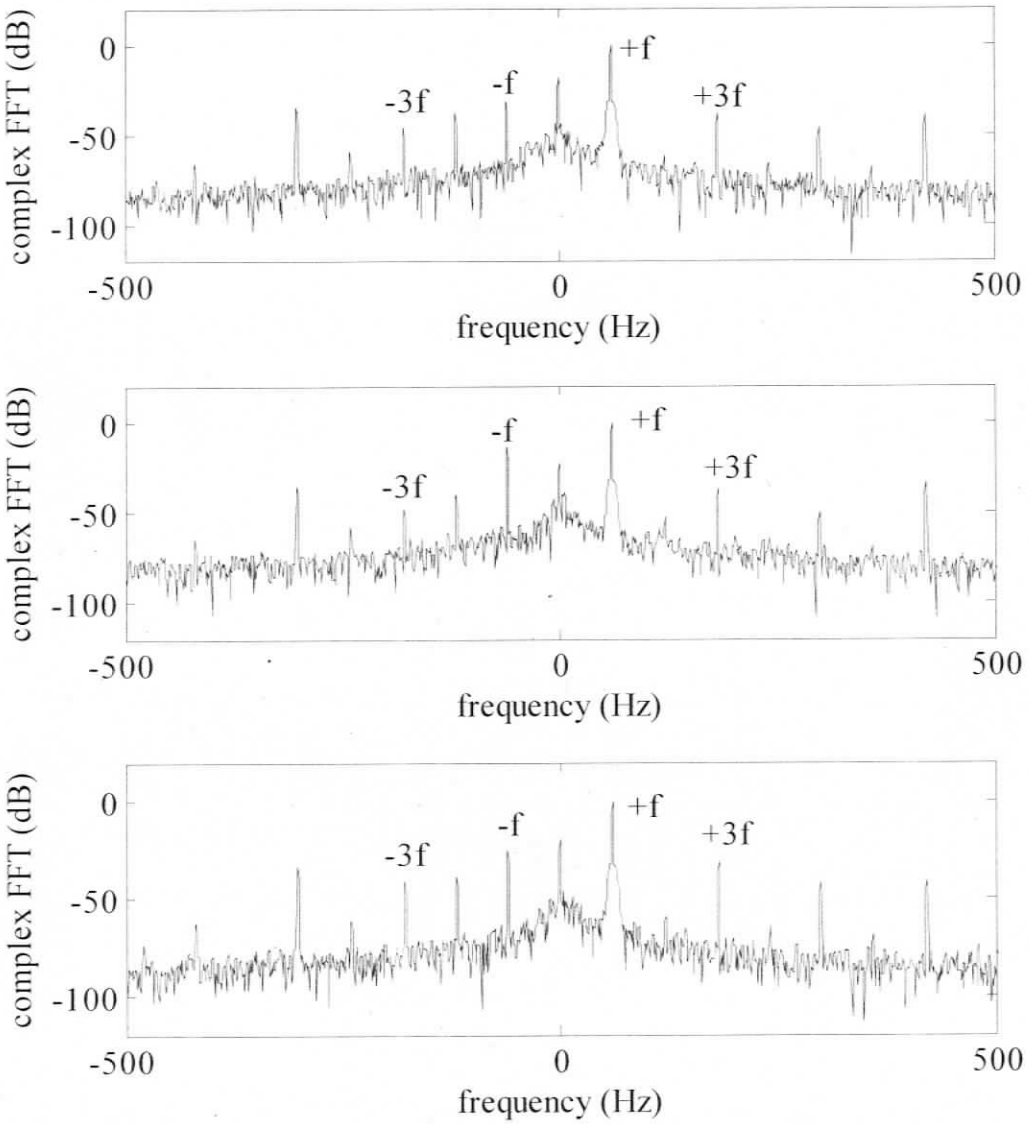

Fig C.2 Simulated line current spectra under no load condition: healthy machine with balanced supply (top); healthy machine with unbalanced supply (middle); single-turn fault machine with balanced supply (bottom); simulated by experimentally collected voltage data.

Appendix D

Details of Star-connected Squirrel Cage Induction Machine Model and Under Test

1) 36 stator slots, 28 rotor slots, 4 pole, 3 hp induction machine:
2) Rotor skew = 5.45 degrees.
3) Mean radius r = 61.72835e-03 m;
4) Length L =104.775e-03 m;
5) Air-gap length g = 0.3683e-03m,
6) Carter's coefficient =1.45;
7) Stator resistance (per phase) R_s=2.1426 ohms;
8) Stator leakage inductance (per phase) L_{ls}=0.017075 H;
9) Rotor bar leakage inductance L_b=0.16045e-06 H;
10) End ring leakage inductance (one segment) L_e=8.16675e-08 H;
11) Rotor bar resistance R_b=39.469e-06 ohm ;
12) End ring resistance (one segment) R_e=3.06992e-06 ohm;
13) J =0.145 (including dc motor rotor inertia)
14) Saturation factor a = 5.75%

Appendix E

Eight Different Supply Unbalance Together with One Balanced Supply Voltage

Table E.1 Variation scheme of unbalanced supply voltage.

	Index of unbalance	V_A (V rms)	V_B (V rms)	V_C (V rms)
1	balance	460	460	460
2	unbalance1	448	472	472
3	unbalance 2	460	448	460
4	unbalance 3	460	448	472
5	unbalance4	460	460	472
6	unbalance5	460	472	448
7	unbalance6	460	472	460
8	unbalance7	460	472	472
9	unbalance8	472	448	460
10	unbalance9	472	460	460

In Table E.1, V_A, V_B and V_C are high-voltage terminals of isolation transformer which were shown as Fig. 5.4. When low-voltage side of isolation transformer are connected to 208 V power supply, V_A, V_B and V_C are respectively connected to the three terminals of line-fed, star-connected induction motor 'balance' together with 'unbalance1' – 'unbalance8' are used to estimate residues. 'HU' fault signatures are measured using 'unbalance 9'. For line-fed delta-connected motor as described in chapter 7, V_A, V_B and V_C, are respectively connected to 208 V supply voltages and the low-voltage side of isolation transformer are connected to the three terminals of induction motor. In Figs. E.1 – E.4, fault signatures obtained from the cases that residues are estimated by using only balanced supply voltage data are displayed.

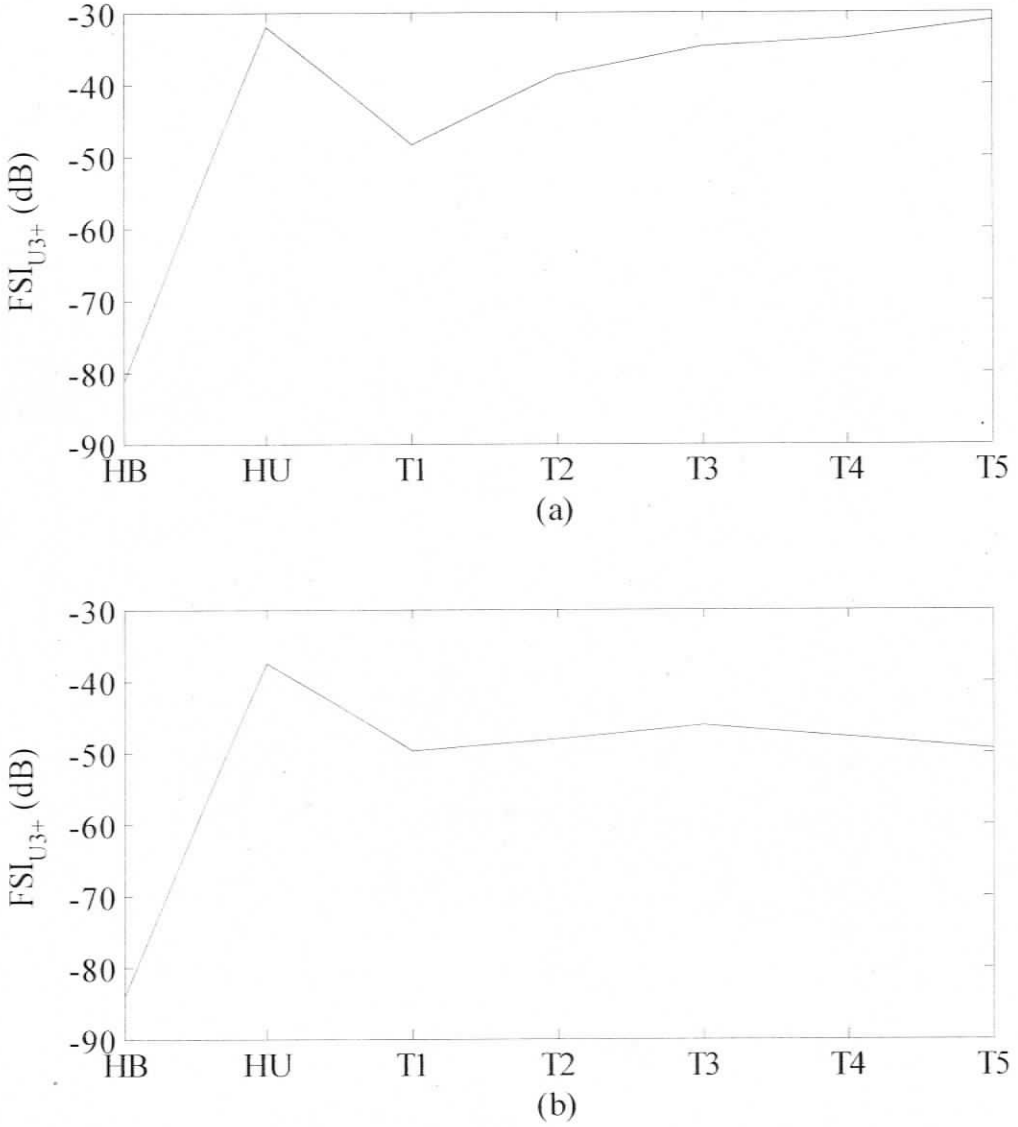

Fig. E.1 Normalized, FSI_{U3+} versus fault severities under different load levels, from top to bottom: (a) 1799 rpm (no load); (b) 1760 rpm (full load).

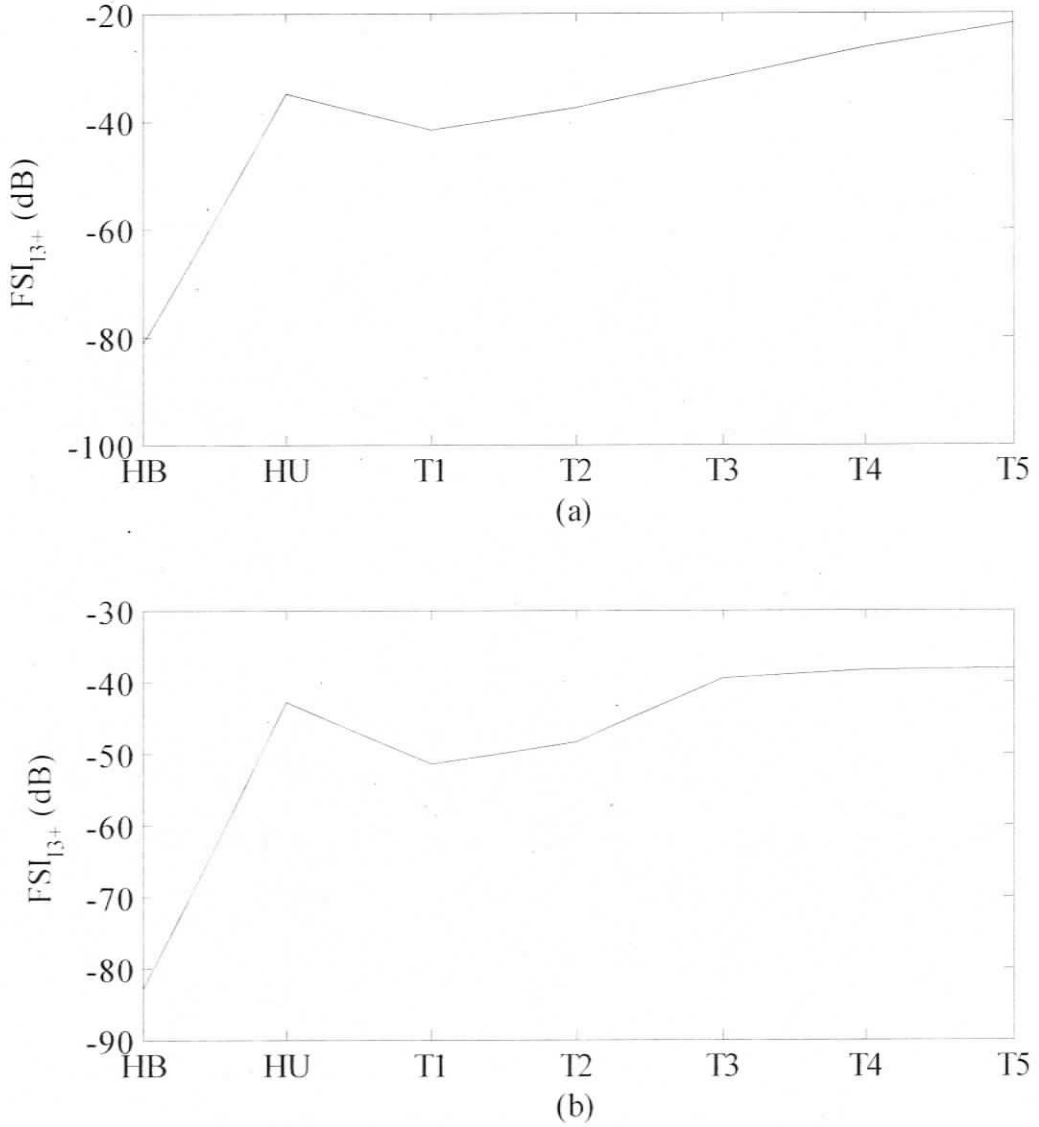

Fig. E.2 Normalized, FSI_{13+} versus fault severities under different load levels, from top to bottom: (a) 1799 rpm (no load): (c) 1760 rpm (full load).

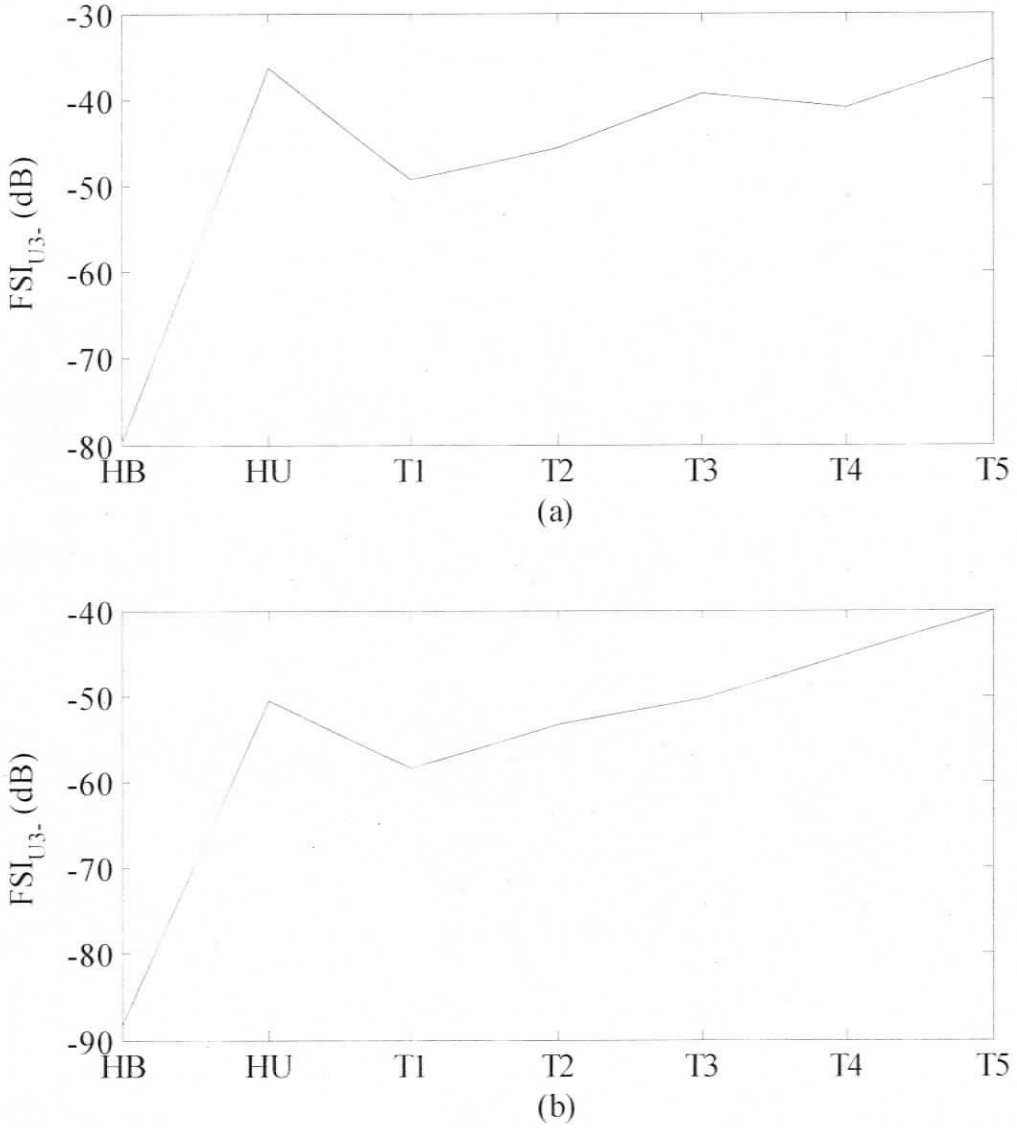

Fig. E.3 Normalized, FSI_{U3-} versus fault severities under different load conditions, from top to bottom: (a) 1799 rpm (no load); (c) 1760 rpm (full load).

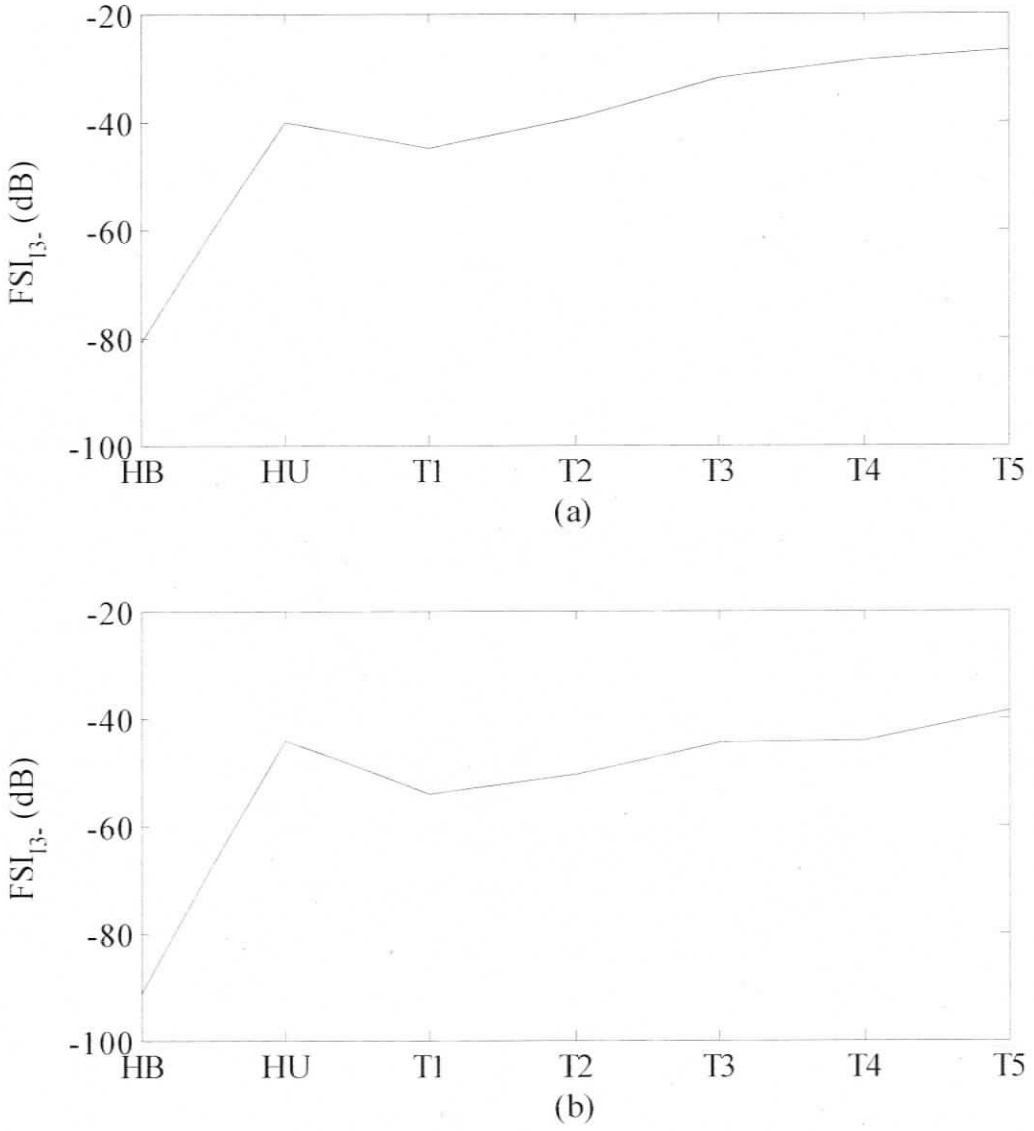

Fig. E.4 Normalized, FSI_{13-} versus fault severities under different load conditions, from top to bottom: (a) 1799 rpm (no load); (c) 1760 rpm (full load).

For Figs. E.1 – E.4, 'HB' are measured from 'balance'; 'HU' are measured from 'unbalance9'. 'balance' and 'unbalance9' are shown in Table E.1.

Appendix F

Complex Coefficients Obtained from Inverter-fed Machine under Frequencies of 30 Hz and 10 Hz

Table F.1 $\bar{k}_{I0+}$ - $\bar{k}_{I3+}$ computed with frequency of 30 Hz.

Rotating speed (rpm)	$\bar{k}_{I0+}$	$\bar{k}_{I1+}$	$\bar{k}_{I2+}$	$\bar{k}_{I3+}$
898	-0.0042 + 0.0074j	-0.1232 + 0.3367j	-0.6323 + 0.0999j	-0.0235 - 0.0739j
874	-0.0002 + 0.0020j	0.1914 + 0.3338j	-0.5520 + 0.7469j	0.0550 - 0.0096j

Table F.2 $\bar{k}_{I0-}$ - $\bar{k}_{I3-}$ computed with frequency of 30 Hz.

Rotating speed (rpm)	$\bar{k}_{I0-}$	$\bar{k}_{I1-}$	$\bar{k}_{I2-}$	$\bar{k}_{I3-}$
898	-0.0014 - 0.0005j	-0.0798 - 0.1442j	0.1602 - 0.4862j	-0.0264 - 0.1372j
874	0.0046 - 0.0005j	1.6463 - 0.1888j	-0.0986 + 0.3589j	-0.1862 - 0.1516j

Table F.3 $\bar{k}_{I0+}$ - $\bar{k}_{I3+}$ computed with frequency of 10 Hz.

Rotating speed (rpm)	$\bar{k}_{I0+}$	$\bar{k}_{I1+}$	$\bar{k}_{I2+}$	$\bar{k}_{I3+}$
299	0.0035 - 0.0025j	0.0446 - 0.2124j	-0.0798 + 0.1942j	0.0087 + 0.0737j
293	0.0125 - 0.0030j	0.2888 + 0.4054j	-0.6592 + 0.3279j	0.1143 + 0.0281j

Table F.4 $\bar{k}_{I0-}$ - $\bar{k}_{I3-}$ computed with frequency of 10 Hz.

Rotating speed (rpm)	$\bar{k}_{I0-}$	$\bar{k}_{I1-}$	$\bar{k}_{I2-}$	$\bar{k}_{I3-}$
299	-0.0055 + 0.0009j	0.1750 + 0.4123j	0.3274 - 0.0391j	0.0233 + 0.0205j
293	-0.0065 - 0.0039j	0.0058 + 0.1880j	0.1670 + 0.2774j	0.0739 + 0.1050j

Appendix G

Details of Delta-connected Squirrel Cage Induction Machine Model and Under Test

3 phase, four-pole, star connected, 2 kW, 60 Hz, 36 stator slots and 45 rotor bars (slots).

1) Stator resistance (per phase) r_s= 0.6 ohm.
2) Stator leakage inductances (per phase): L_{ls}=0.002918 H.
3) Rotor bar resistance r_b=58.27e-07 ohm.
4) Rotor bar leakage inductance L_b=0.343e-09 H.
5) End ring (one segment) resistance r_e=4.5314e-07 ohm.
6) End ring (one segment) leakage inductance L_e=0.175e-09 H.
7) Mean radius r=73.75*1e-03m.
8) Length l_s=76*1e-03m.
9) Air-gap g =0.5e-03m.
10) Carters coefficient =1.95.
11) Inertia J_k= 0.107 kg-m^2.
12) Rotor bar skew 11degrees.

Appendix H

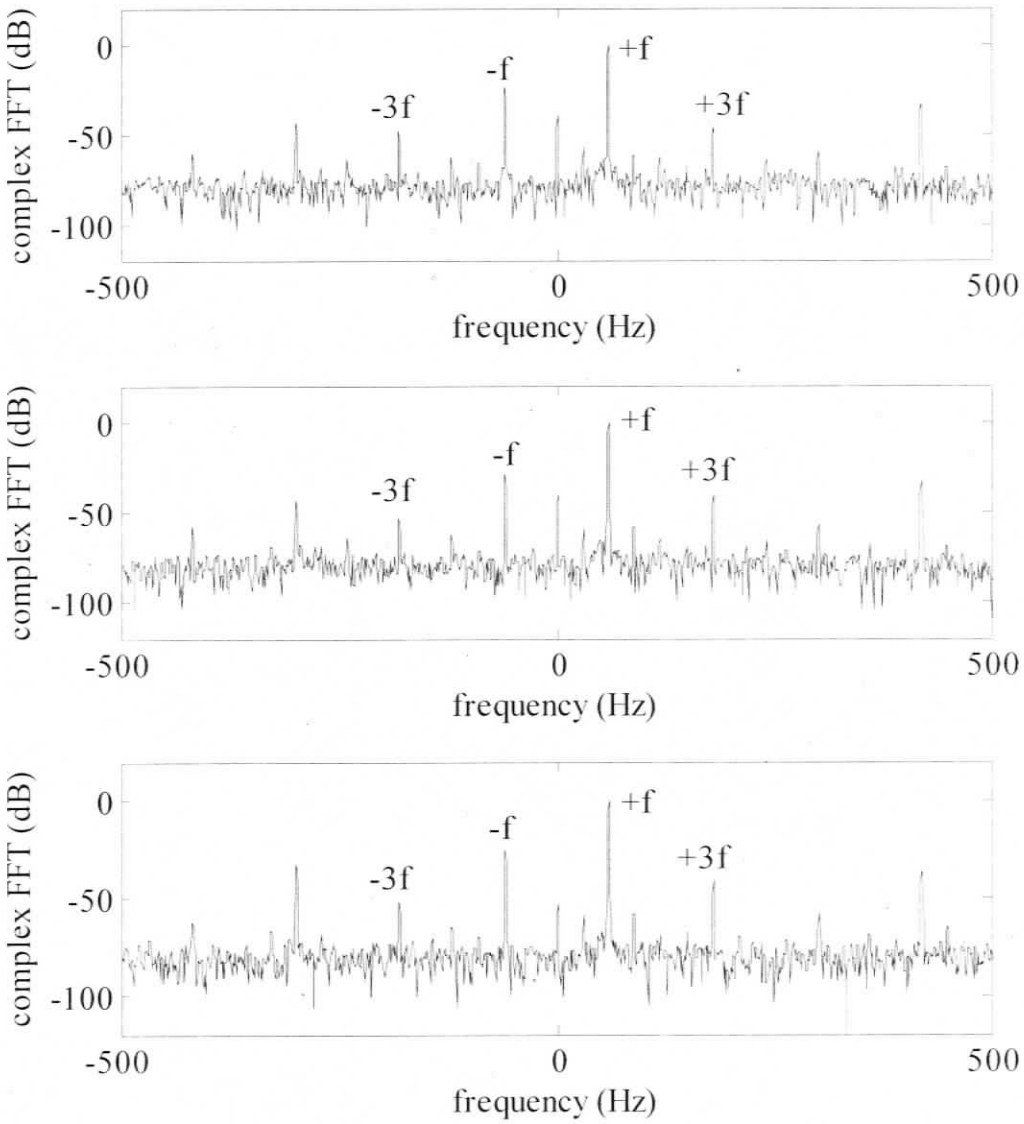

Fig H.1 Experimental line current spectra from line-fed, delta-connected machine under full load condition: healthy machine with balanced supply (top); healthy machine with unbalanced supply (middle); single-turn fault machine with balanced supply (bottom).

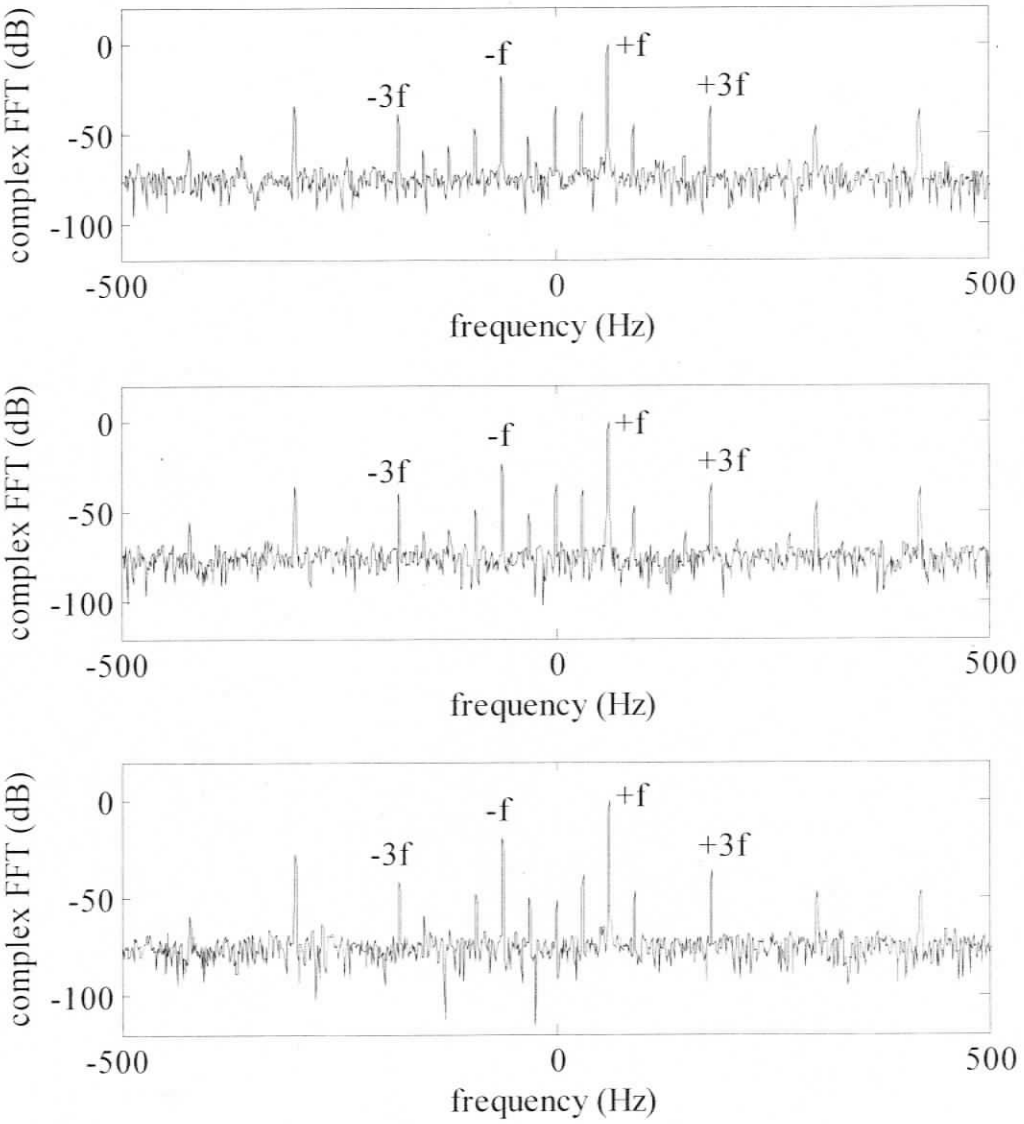

Fig H.2 Experimental line current spectra from line-fed, delta-connected machine under no load condition: healthy machine with balanced supply (top); healthy machine with unbalanced supply (middle); single-turn fault machine with balanced supply (bottom).